NTNU
Norwegian University of
Science and Technology

Electronic Properties of Si as an Intermediate Band Solar Cell

A Density Functional Theory Study

Haakon Hammarbeck

MSc in Physics
Submission date: May 2018
Supervisor: Jon Andreas Støvneng, IFY
Co-supervisor: Turid Reenaas, IFY

Norwegian University of Science and Technology
Department of Physics

Abstract

Crystalline silicon is widely used as a solar cell material in modern day society. This report investigates the possibility of adding an additional energy band placed within the conventional band gap, in order to increase the efficiency of crystalline Si solar cells. Using density functional theory to calculate the electronic structure and finding the density of states along with the Fermi level, the electrical conducting properties of the material are determined. Si in the cubic diamond lattice was used with W and Ag as dopant atoms. Several doping concentrations and unit cell configurations were used with doping concentrations ranging from 25 % to 0.78 % (4-atomic to 128-atomic unit cell). Removing Si-atoms without replacing them with anything was also done, leaving vacancies in the lattice, to mimic more realistic conditions. Using different functionals and basis sets on pure Si and comparing with experiments, the Perdew-Wang 1991 functional was found to give the best results when weighing numerical accuracy vs. computational time. Adding a Hubbard term in the Hamiltonian to further increase the band gap description was tested but turned out to break important physical symmetry properties. The Hubbard term was therefore omitted when analyzing the many impurity configurations. For the systems ranging in unit cell size from 2 to 16, DFT geometry optimizations were run. For the systems ranging in unit cell size from 32 to 128 including Ag, DFTB geometry optimizations were done and DFT energy calculations were done on the optimized geometry. For the systems ranging in unit cell size from 32 to 128 including W, MOPAC geometry optimizations were done and DFT energy calculations were done on the optimized geometry. W-doped Si with a doping concentration of 0.78 % proved to form an intermediate band of width 0.55 eV lying 0.15 eV above the valence band edge. The total band gap of this material was 1.38 eV. It should be noted that most of the results of this thesis is of limited quantitative significance, as DFT is known to underestimate the band gap for solids, and the MOPAC method is a semi-empirical method. The results from this thesis can only point out trends, not accurate results, and the systems that showed tendencies of an intermediate band should be investigated further by higher accuracy DFT calculations and cross-examined by other methods.

Preface

This thesis was written as part of the two year master's program in physics at the Norwegian University of Science and Technology (NTNU). The work presented in this thesis was carried out during the fall of 2017 and the spring of 2018 and marks the end of my studies at NTNU. The idea for this project was made possible by Assoc. Professor Jon Andreas Støvneng and Assoc. Professor Turid Reenaas. Jon Andreas was my main supervisor, helping me with the theoretical models and computational methods. Turid was my co-supervisor, helping me finding the materials of interest in the pursuit of an intermediate band solar cell.

Acknowledgments

Table of Contents

Abbreviations

IBSC	=	Intermediate Band Solar Cell
IB	=	Intermediate Band
QM	=	Quantum Mechanics
DFT	=	Density Functional Theory
KS	=	Kohn-Sham
HF	=	Hartree-Fock
H	=	Hartree
X	=	Exchange
C	=	Correlation
XC	=	Exchange-Correlation
LDA	=	Local Density Approximation
GGA	=	Generalized Gradient Approximation
MGGA	=	Meta-Generalized Gradient Approximation
PW91	=	Perdew-Wang 1991 Functional
PBE	=	Perdew Burke Ernzerhof Functional
PBEsol	=	GGA Functional made by Perdew, Ruzsinszky et al.
M06-L	=	MGGA Functional made by Zhao, Truhar
TPSS	=	MGGA Functional made by Tao, Perdew, Staroverov, Scuseria
FCC	=	Face Centered Cubic
BCC	=	Body Centered Cubic
IBZ	=	Irreducible Brillouin Zone
CB	=	Conduction Band
VB	=	Valence Band
DOS	=	Density of States
ADF	=	Amsterdam Density Functional
DFTB	=	Density Functional based Tight-Binding
MOPAC	=	Molecular Orbital PACkage
NDDO	=	Neglect of Diatomic Differential Overlap
SCM	=	Software for Chemistry & Materials

Chapter 1

Introduction

In the last decades, a higher awareness of our impact on earth has been gained. Mass consumption, pollution and increasing temperatures globally due to fossil fuels have made and will continue to make negative impact on ecosystems all over the world. The Paris Climate Accord and the Kyoto Protocol have given people and governments clear goals that we should reach, and developing clean alternatives to fossil fuels is among humanity's most important challenges in the 21st century [1].

As the sun radiates immense amounts of energy towards earth, solar cells provide a way to utilize this energy. Most solar cells around today are so-called single gap solar cells, with a theoretical maximum efficiency of 40.7%. The first and second generation solar cells are single gap solar cells. In 1997, a new type of solar cell was proposed with a theoretical maximum efficiency of 63.1%, this solar cell is called an intermediate band solar cell (IBSC). The idea is to introduce a new energy band in between the valence band (VB) and the conduction band (CB) in order to capture a higher portion of the incoming sunlight. The IBSC is a type of third generation solar cell. Condensed matter physics is one of the largest research areas in physics today, yet a cheap and functional IBSC has not yet been discovered. This thesis is a contribution to the pursuit of the existence of a cheap and functional IBSC [2].

The development of quantum mechanics and density functional theory (DFT) has provided tools to do theoretical studies of bulk materials and determine their properties. The materials to be investigated in this thesis are crystalline materials, meaning that it is a periodic arrangement of atoms, with associated electrons, a "many-particle" system. Like most systems in quantum mechanics, analytic solutions of the many-particle problems faced in this thesis are not possible, and numerical methods must be used [3].

Si is widely used in the solar cell industry, and its properties are well known. This thesis is a theoretical study of the electronic properties of Si and how these properties are influenced by doping and introduction of vacancies in the material. In this thesis, Ag and W impurities are introduced in crystalline Si in the diamond cubic lattice. Since there is an abundance of knowledge about Si, we can compare some of our results on pure Si to validate our method. The core results we are looking for are the densities of states and

the Fermi levels, which together describe what type of electrical conducting properties the material exhibits.

In chapter 2 the underlying theory behind the calculations, the behavior of electrons and the IBSC are presented. Chapter 3 gives a more detailed explanation on how the theory is implemented in the actual programs used in this thesis, along with their approximations and shortcomings. The results and discussion are found in chapter 4, and the conclusion of our results is given in chapter 5. An outlook on future work to be done based on the results from this thesis is presented in chapter 6.

Chapter 2

Theory

2.1 Quantum mechanics

This section is based on [4] and [3].

2.1.1 The Schrödinger equation

In Erwin Schrödinger's wave mechanical formulation of quantum mechanics, the fundamental equation describing the behaviour of electrons, atoms and molecules is the Schrödinger equation,

$$i\hbar\frac{\partial\Psi}{\partial t} = \hat{H}\Psi. \tag{2.1}$$

Here Ψ is the wave function, describing the state of the system, i is the imaginary unit, and $\hbar$ is the reduced Planck constant. $\hat{H}$ is the energy operator, called the *Hamiltonian*, and its eigenvalues are the allowed energies of the system. The equation describes the time-evolution of the the wave function Ψ. The wave function does not have a physical interpretation, but one can extract physical information by doing mathematical operations on it. To describe a system not varying in time, we use the time-independent Schrödinger equation

$$\hat{H}\Psi = E\Psi, \tag{2.2}$$

where E is the energy of the system. The Hamiltonian for a time-independent N-electron system is

$$\hat{H} = -\frac{\hbar^2}{2m}\sum_{i=1}^{N}\nabla_i^2 + \sum_{i=1}^{N}V(\mathbf{r}_i) + \sum_{i=1}^{N}\sum_{j<i}U(\mathbf{r}_i, \mathbf{r}_j), \tag{2.3}$$

where m is the mass of an electron , ∇_i^2 is the Laplacian, $V(\mathbf{r}_i)$ is the interaction energy between electron i and the nuclei, and $U(\mathbf{r}_i, \mathbf{r}_j)$ is the interaction energy between electron i and j. In the *Born-Oppenheimer approximation*, we assume that the nuclei and electrons can be modeled separately,

$$\Psi_{\text{nuclei, electrons}} = \Psi_{\text{nuclei}} \times \Psi_{\text{electrons}}. \tag{2.4}$$

2.1.2 Hartree-Fock method

The total electron wave function is a function of the coordinates of all the N electrons,

$$\Psi = \Psi(\mathbf{r}_1, \mathbf{r}_2, \ldots, \mathbf{r}_N). \tag{2.5}$$

For an N-electron system, the dimension of Ψ scale as $3N$. Solving the Schrödinger equation quickly becomes computationally demanding for a large electron system. For example, a system of, say, 10 Si atoms each containing 14 electrons would require a wave function of 420 dimensions. We therefore make the approximation of writing the total Hamiltonian as a sum of the single-electron Hamiltonians,

$$\hat{H} = \hat{H}_1 + \hat{H}_2 + \cdots + \hat{H}_N = \sum_{i=1}^{N} \hat{H}_i, \tag{2.6}$$

where $\hat{H}_i$ describes the kinetic and potential energy of electron i. The eigenfunctions of $\hat{H}$ now become a product of single-electron wave functions (spin orbitals),

$$\Psi(\mathbf{r}_1, \mathbf{r}_2, \ldots, \mathbf{r}_N) = \chi_1(\mathbf{r}_1)\chi_2(\mathbf{r}_2)\ldots\chi_N(\mathbf{r}_N) = \prod_{i=1}^{N} \chi_i(\mathbf{r}_i). \tag{2.7}$$

This is known as the *Hartree product*.

Electrons are fermions, meaning their wave function must be anti-symmetric, i.e interchanging two electrons will make the wave function change sign,

$$\Psi(\mathbf{r}_i, \mathbf{r}_j) = -\Psi(\mathbf{r}_j, \mathbf{r}_i), \vee\, i \neq j. \tag{2.8}$$

The wave function (2.7) is a solution to the Schrödinger equation (2.2), but it does not necessarily fulfill the antisymmetry principle for fermions. To fulfill this principle, we instead write (2.7) as a *Slater determinant*,

$$\Psi(\mathbf{r}_1, \mathbf{r}_2, \ldots, \mathbf{r}_N) = \frac{1}{\sqrt{N!}} \begin{vmatrix} \chi_1(\mathbf{r}_1) & \chi_1(\mathbf{r}_2) & \cdots & \chi_1(\mathbf{r}_N) \\ \chi_2(\mathbf{r}_1) & \chi_2(\mathbf{r}_2) & \cdots & \chi_2(\mathbf{r}_N) \\ \vdots & \vdots & \ddots & \vdots \\ \chi_N(\mathbf{r}_1) & \chi_N(\mathbf{r}_2) & \cdots & \chi_N(\mathbf{r}_N) \end{vmatrix}. \tag{2.9}$$

Here the prefactor $1/\sqrt{N!}$ normalizes the wave function. Writing the wave function this way is known as the *Hartree-Fock method*. We note that the wave function in this approximation equals zero when two orbitals are the same, satisfying the *Pauli principle*. We can now write the Schrödinger equation for each electron state χ_i as

$$\left[-\frac{\hbar^2}{2m}\nabla^2 + V(\mathbf{r}) + V_{\mathrm{H}}(\mathbf{r}) + V_{\mathrm{X}}(\mathbf{r}) \right] \chi_i(\mathbf{r}) = E_i \chi_i(\mathbf{r}). \tag{2.10}$$

Here $V(\mathbf{r})$ represents the the interaction energy between an electron and the collection of nuclei. The exchange interaction V_{X} is quantum mechanical effect occurring between

identical particles. The *Hartree potential* $V_H(\mathbf{r})$ corresponds to the classical Coulomb repulsion energy, as an average over charge density:

$$V_H(\mathbf{r}) = e^2 \int \frac{n(\mathbf{r}')}{|\mathbf{r} - \mathbf{r}'|} d\mathbf{r}', \qquad (2.11)$$

where the electron density at position $\mathbf{r}$ is given as

$$n(\mathbf{r}) = 2 \sum_{i=1}^{N} \psi_i^*(\mathbf{r}) \psi_i(\mathbf{r}). \qquad (2.12)$$

The factor 2 is due to spin degeneracy, so two electrons can have the same spatial quantum state provided they have opposite spin. If we can determine the energy purely in terms of electron density, we reduce the problem from a $3N$-dimensional problem to a 3 dimensional problem. As of now, we have only included the kinetic energy of the electrons, potential energy of the electrons and nuclei, and the interaction energy between the electrons themselves (V_H and V_X). However, in a quantum mechanical description we need to include an additional energy term which do not have a classical counterpart, namely the *correlation* (C) energy. We can write the exchange and correlation energy as a single term, the exchange-correlation (XC) energy V_{XC}.

2.1.3   Spin-orbit coupling

We will mostly neglect relativistic effects, but when it is included, we will add the spin-orbit coupling term in the Hamiltonian,

$$\hat{H}_{\text{Spin-orbit}} = \frac{\hbar^2}{2m^2c^2} \frac{1}{r} \frac{dV}{dr} \mathbf{L} \cdot \sigma, \qquad (2.13)$$

where c is the speed of light, σ is the spin of the particle, and $\mathbf{L}$ is the angular momentum operator. This term makes an energy level of a spin state split slightly into two unique levels [5]. Calculating the ground state with this extra term comes at a high computational cost, and this term is typically small compared to the energy level itself, so it is not essential to include it for most electronic structure calculations in this thesis. The spin-orbit coupling is more apparent for systems including heavy elements.

2.2   Density functional theory

This section is based on [6] and [3].

2.2.1   The Hohenberg-Kohn theorems

Density functional theory (DFT) rests on two mathematical theorems proved by Hohenberg and Kohn [3]:

Theorem 1: *The ground-state energy from Schrödinger's equation is a unique functional of the electron density.*

Theorem 2: *The electron density that minimizes the energy of the overall functional is the true electron density corresponding to the full solution of the Schrödinger equation.*

Proof of theorem 1: Assume that there exist two external potentials $V_1(\mathbf{r})$ and $V_2(\mathbf{r})$ giving rise to the same ground state density, $n(\mathbf{r})$. The potentials differ by no more than a constant and belong to the distinct Hamiltonians $\hat{H}_1 = \hat{H}_0 + V_1$ and $\hat{H}_2 = \hat{H}_0 + V_2$, giving rise to two distinct wave functions Ψ_1 and Ψ_2. The ground state energies, E_1 and E_2, for the two systems are given by

$$E_1 = \langle \Psi_1 | \hat{H}_1 | \Psi_1 \rangle = \int V_1(\mathbf{r})n(\mathbf{r})d\mathbf{r} + \langle \Psi_1 | \hat{H}_0 | \Psi_1 \rangle, \tag{2.14}$$

$$E_2 = \langle \Psi_2 | \hat{H}_2 | \Psi_2 \rangle = \int V_2(\mathbf{r})n(\mathbf{r})d\mathbf{r} + \langle \Psi_2 | \hat{H}_0 | \Psi_2 \rangle. \tag{2.15}$$

We now assume that the ground state is non-degenerate. Due to the variational principle, no wave function can give a lower energy than the energy eigenvalue of Ψ_1 for the operator $\hat{H}_1$:

$$E_1 < \langle \Psi_2 | \hat{H}_1 | \Psi_2 \rangle = \int V_1(\mathbf{r})n(\mathbf{r})d\mathbf{r} + \langle \Psi_2 | \hat{H}_0 | \Psi_2 \rangle \tag{2.16}$$

$$= \int V_2(\mathbf{r})n(\mathbf{r})d\mathbf{r} + \langle \Psi_2 | \hat{H}_0 | \Psi_2 \rangle + \int (V_1(\mathbf{r}) - V_2(\mathbf{r}))n(\mathbf{r})d\mathbf{r}$$

$$= E_2 + \int (V_1(\mathbf{r}) - V_2(\mathbf{r}))n(\mathbf{r})d\mathbf{r}.$$

If we redo the calculation for the second system, we get

$$E_2 < E_1 + \int (V_2(\mathbf{r}) - V_1(\mathbf{r}))n(\mathbf{r})d\mathbf{r}. \tag{2.17}$$

If we now add (2.16) and (2.17) together, we get

$$E_1 + E_2 < E_1 + E_2, \tag{2.18}$$

which clearly is a contradiction. Thus, the ground state energy has to be a *unique* functional of the electron density.

Proof of theorem 2: We consider an all-electron system, with an arbitrary number of electrons moving under the influence of an external potential (for example from the nuclei in a crystal lattice). The electron density $n(\mathbf{r})$ uniquely determines the external potential, which, in turn, uniquely determines the Hamiltonian. The Hamiltonian (for non-degenerate states) determines the ground state wave function, so we can conclude that the electron density uniquely determines physical observables such as the various energy terms and the total energy:

$$E[n] = T[n] + V_{\text{int}}[n] + \int V_{\text{ext}}(\mathbf{r})n(\mathbf{r})d\mathbf{r}, \tag{2.19}$$

where T is the kinetic energy, V_{ext} is the external potential, and V_{int} is the electron-electron interaction. Let us define

$$F[n] \equiv \langle \Psi | T + V_{int} | \Psi \rangle = T[n] + V_{int}[n], \tag{2.20}$$

such that

$$E[n] = F[n] + \int V_{ext}(\mathbf{r})n(\mathbf{r})\mathrm{d}\mathbf{r}. \tag{2.21}$$

$F[n]$ is a universal functional, valid for any number of particles and any external potential [7]. The energy functional of $\Psi'(\mathbf{r})$ is given by

$$E' = E[\Psi'] = \langle \Psi' | V_{ext} | \Psi' \rangle + \langle \Psi' | T + V_{int} | \Psi' \rangle , \tag{2.22}$$

and has a minimum at the true ground state, Ψ_1. By combining equations (2.20) and (2.22), we get

$$E[\Psi'] = F[n'] + \int V_{ext}(\mathbf{r})n'(\mathbf{r})\mathrm{d}\mathbf{r} = E[n'] \tag{2.23}$$

$$\geq E[\Psi_1] = F[n_1] + \int V_{ext}(\mathbf{r})n_1(\mathbf{r})\mathrm{d}\mathbf{r} = E[n_1].$$

If one knows the exact form of this universal functional, one could calculate the exact ground state energy purely in terms of the electron density by using the variational principle. The electron density that minimizes the energy will therefore be the true electron density of the ground state.

The first theorem says that there is a one-to-one mapping between the ground-state wave function and the ground-state electron density. This greatly reduces the dimensionality of our original problem, finding the ground state energy. We only have to find the 3-dimensional electron density, instead of finding the $3N$-dimensional wave function. The second theorem gives us a mathematical way to find the ground state energy: To minimize an energy functional of the electron density. The second theorem also guarantees that the electron density used to mathematically minimize the energy functional is the true physical ground state electron density. Let us use the variational principle to minimize equation (2.23) with respect to the electron density. We minimize the energy by introducing a Lagrangian multiplier $(-\mu)$:

$$\frac{\delta}{\delta n(\mathbf{r})} \left[E[n(\mathbf{r})] - \mu \int n(\mathbf{r})\mathrm{d}(\mathbf{r}) \right] = 0. \tag{2.24}$$

Inserting the expression for the energy (2.21), we get

$$\frac{\delta F[n(\mathbf{r})]}{\delta n(\mathbf{r})} + V_{ext}(\mathbf{r}) = -\mu. \tag{2.25}$$

From the expression for μ, we recognize it as the chemical potential, or the negative of the electronegativity:

$$\chi = -\mu = \left(\frac{\partial E}{\partial N} \right)_{V_{ext}}. \tag{2.26}$$

The chemical potential is also called the Fermi level, E_F, and is an important property when determining the electrical conducting properties of the material [8]. More details about the influence of the Fermi level is brought forward in section 2.3. It turns out that an exact solution of equation (2.24) is not possible for interacting systems, since $F[n]$ is not generally known. Walter Kohn and Lu Jeu Sham introduced a way to work around this problem, by replacing the system of of interacting electrons with non-interacting electrons having the same electron density. These non-interacting orbitals are called Kohn-Sham orbitals and are solutions to Kohn-Sham equations [6, 9].

2.2.2 Exchange-correlation functional and the Kohn-Sham equations

Given an electron configuration $\{\psi_i\}$ that collectively describes the electron density (2.12), we denote its energy as $E_{\text{known}}[\{\psi_i\}]$. We denote it by "known" since we know the exact form of all the contributing terms. Since the argument of $E_{\text{known}}[\{\psi_i\}]$ is a function and its output is a scalar, it is called a *functional* rather than a function.

$$E_{\text{known}}[\{\psi_i\}] = -\frac{\hbar^2}{2m} \sum_i^N \int \psi_i^* \nabla^2 \psi_i \mathrm{d}\mathbf{r} + \int V_{\text{ext}}(\mathbf{r}) n(\mathbf{r}) \mathrm{d}\mathbf{r} \tag{2.27}$$

$$+ \frac{e^2}{2} \int \int \frac{n(\mathbf{r}) n(\mathbf{r}')}{|\mathbf{r} - \mathbf{r}'|} \mathrm{d}\mathbf{r}\mathrm{d}\mathbf{r}' + e^2 \sum_j \sum_{k \neq j} \frac{Z_j Z_k}{|\mathbf{R}_j - \mathbf{R}_k|},$$

where Z_j and Z_k are the atomic numbers for atoms j and k, so the last term is the potential energy due to the repulsion between the nuclei. We now promote the energy functional to include the quantum mechanical effects exchange and correlation between the electrons,

$$E[\{\psi_i\}] = E_{\text{known}}[\{\psi_i\}] + E_{\text{XC}}[\{\psi_i\}]. \tag{2.28}$$

To find $E[\{\psi_i\}]$, one must solve the *Kohn-Sham equations*,

$$\left[-\frac{\hbar^2}{2m} \nabla^2 + V_{\text{ext}}(\mathbf{r}) + V_{\text{H}}(\mathbf{r}) + V_{\text{XC}}(\mathbf{r}) \right] \psi_i(\mathbf{r}) = \epsilon_i \psi_i(\mathbf{r}), \tag{2.29}$$

where $V_{\text{XC}}(\mathbf{r})$ is the exchange-correlation potential, defined as the functional derivative of the exchange-correlation energy,

$$V_{\text{XC}}(\mathbf{r}) = \frac{\delta E_{\text{XC}}[n(\mathbf{r})]}{\delta n(\mathbf{r})}. \tag{2.30}$$

When the wave functions and the electron density are found, the energy is found from equation (2.28). If one knew the exact form of E_{XC}, this would be a straightforward task to solve numerically. However, the true form of the exchange-correlation functional is not known and one has to approximate it [3]. The next subsections will present some different ways to do this.

2.2.3 Local density approximation

In the early decades of DFT, the *local density approximation* (LDA) was the workhorse for calculations on atomic, molecular and bulk systems [10]. The exchange-correlation

energy functional in the LDA is given as

$$E_{XC}^{LDA}[n] = \int n(\mathbf{r})\epsilon_{XC}^{LDA}(n(\mathbf{r}))d\mathbf{r}, \tag{2.31}$$

where $\epsilon_{XC}^{LDA}(n(\mathbf{r}))$ is the exchange-correlation energy density for the spatially uniform electron gas [11]. For an inhomogeneous system, the electron gas is divided into infinitesimal (or finite for a numerical algorithm) volumes, each having a constant electron density. From (2.31) we see that the energy from the uniform electron gas at each point in space is weighted by its actual electron density [6]. The exchange-correlation energy density can also be expressed as the sum of the exchange and correlation energies:

$$\epsilon_{XC} = \epsilon_X + \epsilon_C \Longrightarrow E_{XC} = E_X + E_C. \tag{2.32}$$

Even though the LDA was originally meant to give good approximations to systems differing only slightly from the uniform electron gas, it has proven to give relatively good results for highly inhomogeneous systems as well. Reasons for this success come from systematic error cancellations. The exchange energies are overestimated, while the correlation energies are underestimated [12].

2.2.4 Generalized gradient approximation

As the electron density becomes less homogeneous, the LDA becomes a poorer approximation (in principle). In the *generalized gradient approximation* (GGA) one takes into account the gradient in electron density in addition to the electron density itself. Most generally, the exchange-correlation functional is given by

$$E_{XC}^{GGA}[n] = \int f^{GGA}(n(\mathbf{r}), \nabla n(\mathbf{r}))d\mathbf{r}, \tag{2.33}$$

where f^{GGA} is some function of both the electron density and its gradient. This approximation corrects the LDA and converges towards it in the uniform electron gas limit. As with the LDA, the exchange and correlation energies can be modelled separately,

$$E_{XC}^{GGA} = E_X^{GGA} + E_C^{GGA}. \tag{2.34}$$

The magnitude of the correlation energy is typically less than 10 % of the exchange energy, so it is most important that the exchange energy functional is accurate [13]. The exchange energy functional in the generalized gradient approximation is defined as

$$E_X^{GGA}[n] = \int n(\mathbf{r})\epsilon_X^{LDA}(n(\mathbf{r}))F_X(s)d\mathbf{r}, \tag{2.35}$$

where $F(s)$ is an enhancement factor, weighting the LDA exchange energy for a given electron density at that point in space, and s is a dimensionless variable defined as

$$s = \frac{|\nabla n|}{(24\pi^2)^{1/3}n^{4/3}}. \tag{2.36}$$

This parameter can be seen as an "inhomogeneity parameter", since $\nabla n = 0$ makes $s = 0$ and increasing the inhomogeneity increases s. The enhancement factor for the PW91 (Perdew-Wang 1991) exchange functional is given by [13],

$$F_X^{PW91}(s) = \frac{1 + sa_2 \sinh^{-1}(sa_1) + (a_3 + a_4 e^{-100s^2})s^2}{1 + sa_2 \sinh^{-1}(sa_1) + a_5 s^4}. \tag{2.37}$$

All the constants a_i, $i \in \{1, \ldots, 5\}$ are numerical constants, independent of the physical system it is describing. By inspecting (2.37), we see that if the gas is homogeneous ($\nabla n = 0 \Rightarrow s = 0$), then $F_X^{PW91} = 1$ and (2.35) reduces to the LDA. According to [6], GGA will yield especially better results than LDA for systems with covalent bonding, which is the case for Si in the diamond lattice, to be investigated in this thesis.

2.2.5 meta-GGA

The exchange-correlation functional in the meta-GGA approximation is given by

$$E_{XC}^{MGGA}[n] = \int f^{MGGA}(n(\mathbf{r}), \nabla n(\mathbf{r}), \nabla^2 n(\mathbf{r})) d\mathbf{r}. \tag{2.38}$$

Again, we are most interested in the exchange energy functional which can be written, similarly to the GGA, as

$$E_X^{MGGA}[n] = \int n(\mathbf{r}) \epsilon_X^{LDA}(n(\mathbf{r})) F_X(p, z) d\mathbf{r}. \tag{2.39}$$

The dimensionless "inhomogeneity parameters" are

$$p = \frac{|\nabla n|^2}{(24\pi^2)^{2/3} n^{8/3}} = s^2, \tag{2.40}$$

and

$$z = \frac{|\nabla n|^2}{8n} \left[\sum_\sigma \sum_i^{occupied} \frac{\hbar^2}{2m} |\nabla \psi_{i\sigma}(\mathbf{r})|^2 \right]^{-1} \leq 1. \tag{2.41}$$

Here σ runs over the two spin states, and the second sum is the total kinetic energy density of the occupied Kohn-Sham orbitals [14]. The meta-GGA often yields better results than LDA and GGA. It performs especially well when determining band gaps, which LDA and GGA are known to underestimate [15]. We also see the increasing complexity by adding the wave functions in the exchange correlation functional. Solving the Kohn-Sham equations (2.29) with this approximation is a lot more computationally intense than with the LDA or GGA.

In this thesis, we will limit the calculations to the three methods explained in detail above, but for completeness let us put these methods in perspective. LDA, GGA, and meta-GGA are the first three approximations in what is known as "Jacob's ladder". Increasing the rung on the ladder means you increase the physical information of the system. For the first three rungs on Jacob's ladder mentioned above, we increase the information about the electron density : $n \to n, \nabla n \to n, \nabla n, \nabla^2 n$. There are other, higher order

approximations which include more physical information, for example hyper-GGA which includes the exact exchange energy. The exact exchange energy is *non-local*, meaning that it uses information about total electron density. So evaluating the energy density at each point in space requires information about the entire electron density, which makes it a lot more computationally demanding. A way to cope with this is to make a "screened exact exchange functional", so that it only needs information about the surrounding electron density within some finite radius. The GGA and meta-GGA are called "semi non-local" since they use information about the immediate surrounding electron density to evaluate ∇n and $\nabla^2 n$, while the LDA is purely local, hence the name. Another class of approximations are hybrid functionals. These include empirical parameters and are typically best suited for systems that closely resemble the ones where these empirical parameters were developed [3].

2.3 Solid state physics

2.3.1 Crystal structures

An ordered, periodic collection of nuclei is called a *crystal*. More formally, we can write this as

$$\text{Crystal structure} = \text{Bravais lattice} \times \text{basis}. \tag{2.42}$$

A Bravais lattice is a spatially infinite lattice of discrete points spanned by

$$\mathbf{R} = n_1 \mathbf{a}_1 + n_2 \mathbf{a}_2 + n_3 \mathbf{a}_3, \tag{2.43}$$

where n_1, n_2, n_3 are integers and $\mathbf{a}_1$, $\mathbf{a}_2$, $\mathbf{a}_3$ are called the primitive vectors. The entire crystal (all space) is spanned by repeating some volume in the Bravais lattice, this volume is called a *unit cell* [8]. Most solar cell materials are crystals, including Si, to be investigated in this thesis. Si forms in the *diamond lattice*, sometimes called diamond cubic lattice. A way to create this crystal structure, is to use a *face centered cubic* (fcc) Bravais lattice combined with a two-atomic basis. The fcc Bravais lattice unit cell is visualized in Figure 2.1a. At each point in the fcc lattice, we place an atom at position $(0, 0, 0)$ and another one at $\left(\frac{1}{4}, \frac{1}{4}, \frac{1}{4}\right)$ relative to the points in the lattice, see Figure 2.1b. Combining these two yields the diamond lattice unit cell, Figure 2.1c, and when taking all the integers in equation (2.43) into account, the spatially infinite crystal structure is spanned. The length of one side of the unit cell is called the *lattice constant* or lattice parameter, and is typically denoted by a and given in units of Ångstrøm (Å), 10^{-10} m. For our purposes, it is more convenient to describe the material in terms of energy than real space. Taking the Fourier transform of the real lattice gives us the *reciprocal lattice*. In this space, we describe the crystal by its frequencies, or the closely related wave vector $\mathbf{k}$, so it is also frequently called k-space. The lattice vectors in reciprocal space $\mathbf{b}_1$, $\mathbf{b}_2$, $\mathbf{b}_3$ are related to the primitive vectors by

$$\mathbf{b}_1 = 2\pi \frac{\mathbf{a}_2 \times \mathbf{a}_3}{\mathbf{a}_1 \cdot (\mathbf{a}_2 \times \mathbf{a}_3)}, \tag{2.44}$$

$$\mathbf{b}_2 = 2\pi \frac{\mathbf{a}_3 \times \mathbf{a}_1}{\mathbf{a}_2 \cdot (\mathbf{a}_3 \times \mathbf{a}_1)}, \tag{2.45}$$

$$\mathbf{b}_3 = 2\pi \frac{\mathbf{a}_1 \times \mathbf{a}_2}{\mathbf{a}_3 \cdot (\mathbf{a}_1 \times \mathbf{a}_2)}, \tag{2.46}$$

such that

$$\mathbf{a}_i \cdot \mathbf{b}_j = \begin{cases} 2\pi & \text{if } i = j \\ 0 & \text{if } i \neq j \end{cases}. \tag{2.47}$$

Given a site in the lattice, the space where points are closer to that site than any other site is called the *Wigner-Seitz cell*. The Wigner-Seitz cell in reciprocal space is called the *1st Brillouin zone*. Due to the symmetries in the lattice, we only have to solve the Schrödinger equation within this region to describe the spatially infinite crystal. The 1st Brillouin zone for a fcc unit cell is illustrated in Figure 2.2.
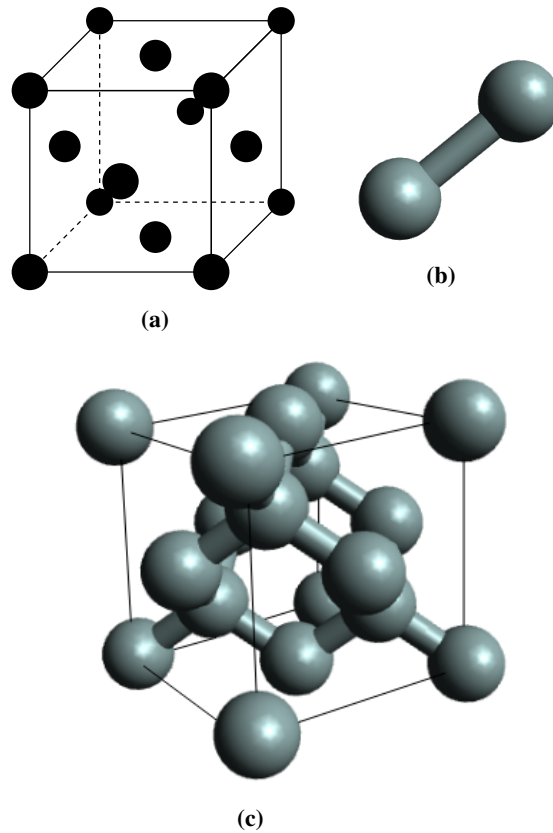
Figure 2.1: The fcc unit cell **(a)** combined with a two-atomic basis **(b)** creates the diamond unit cell **(c)**.

We will now look at two important consequences of the symmetries in the lattice. Let us apply an operation R_i on the Schrödinger equation. The operation R_i is some operation consisting of a point symmetry operation (rotations/reflections/inversions and any combination of these leaving the lattice invariant) and a non-symmorphic operation (an operation that translates, or shifts the system a fraction of the lattice vector). The set of these operations forms a group. An operator acting on some function $g(\mathbf{r})$ will give

$$R_i g(\mathbf{r}) = g(R_i \mathbf{r} + \mathbf{t}_i). \tag{2.48}$$

Here, $R_i \mathbf{r}$ is the rotated/reflected/inverted position $\mathbf{r}$ and $\mathbf{t}_i$ is the non-symmorphic spatial translation. The Hamiltonian is invariant under any symmetry operation, so the operator acts directly on the wave function, $\psi_{i,\mathbf{k}}$:

$$\hat{H}\psi_{i,R_i\mathbf{k}}(R_i \mathbf{r} + \mathbf{t}_i) = \epsilon_{i,\mathbf{k}}\psi_{i,\mathbf{k}}(\mathbf{r}), \tag{2.49}$$

and

$$\hat{H}\psi_{i,R_i^{-1}\mathbf{k}}(\mathbf{r}) = \epsilon_{i,\mathbf{k}}\psi_{i,\mathbf{k}}(R_i \mathbf{r} + \mathbf{t}_i), \tag{2.50}$$
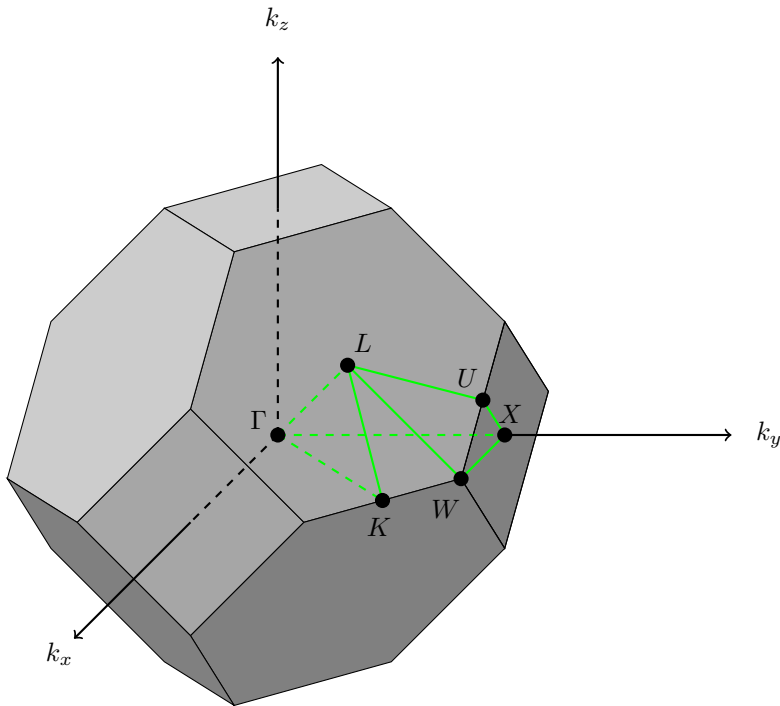
Figure 2.2: The first Brillouin zone of a fcc unit cell. High symmetry points (critical points) are marked with dots and labeled with letters, high symmetry lines are marked with green. Dashed lines are inside the Brillouin zone.

are also eigenfunctions of the Hamiltonian with the same energy eigenvalue. Here are two critical consequences of this symmetry relation:

• There are some k points where $R_i^{-1}\mathbf{k} = \mathbf{k} = R_i\mathbf{k}$. At these points, there is a relation between the eigenfunctions, they can be classified according to group representations. These points are called *high symmetry points*, or *critical points*. For example in the cubic crystal, all states with $\mathbf{k} = 0$ have degeneracy 1,2 or 3.

• There is some fraction of the Brillouin zone that contains all the information needed to describe the entire Brillouin zone and hence the entire crystal. The information outside this zone can be found by using symmetry operations on points within this zone. This zone is termed the *irreducible Brillouin zone* (IBZ).

The high symmetry points and the IBZ are visualized in Figure 2.2. The IBZ is within the region defined by the green lines. For a more thorough discussion about crystal symmetries and the 1st Brillouin zone, see [5].

2.3.2 Bloch's theorem

An electron moving in a periodic crystal lattice obeys the Schrödinger equation with a periodic potential. We can write this as

$$\hat{H}\psi = [-\frac{\hbar^2}{2m}\nabla^2 + V(\mathbf{r})]\psi = E\psi, \tag{2.51}$$

where V has the same periodicity as the physical lattice, with lattice parameter a:

$$V(\mathbf{r} + \mathbf{R}) = V(\mathbf{r}). \tag{2.52}$$

Since all the unit cells are equivalent, we expect a solution such that the probability density $|\psi|^2$ is periodic in the lattice. The solutions of the Schrödinger equation with a periodic potential (2.51) are on the form

$$\psi_{n,k}(\mathbf{r}) = u_{n,k}(\mathbf{r})\mathrm{e}^{i\mathbf{k}\cdot\mathbf{r}}, \quad n = 1, 2, 3, \ldots \tag{2.53}$$

These solutions to the Schrödinger equation are called Bloch waves, or Bloch functions. It is a plane wave $\mathrm{e}^{i\mathbf{k}\cdot\mathbf{r}}$ modulated by some function $u_{n,k}$ that follows the periodicity of the lattice. The energy eigenvalues of (2.51) are

$$E = E_{n,k}, \quad n = 1, 2, 3, \ldots \tag{2.54}$$

We call these eigenvalues energy bands since they range as continuous bands, with forbidden gaps in between them [16].

2.3.3 The Fermi-Dirac distribution

When the temperature of a crystal is close to absolute zero, the electrons will occupy only the lowest energy states. Electrons, being fermions, follow the Pauli principle, so each energy state can contain maximum two electrons, due to spin degeneracy. The distribution function that describes the behaviour of electrons in a crystal is the *Fermi-Dirac distribution function*

$$f(E) = \frac{1}{1 + e^{(E-E_F)/k_B T}}. \tag{2.55}$$

The function gives the probability of a state with energy E to be occupied, where E_F is the *Fermi level*, k_B is Boltzmann's constant and T is the temperature of the system. From equation (2.55) we note that $f(E_F) = 1/2$. This means that there is a 50 % chance that a state with energy $E = E_F$ is occupied, regardless of T. At temperatures larger than zero, there will be a finite probability that electrons occupy energy states higher than the Fermi level, leaving unoccupied states below the Fermi level [17]. At zero temperature, the Fermi-Dirac distribution function equals unity when $E < E_F$, and zero when $E > E_F$. The *Fermi energy* is defined to be the occupied state with the highest energy at zero temperature [8].
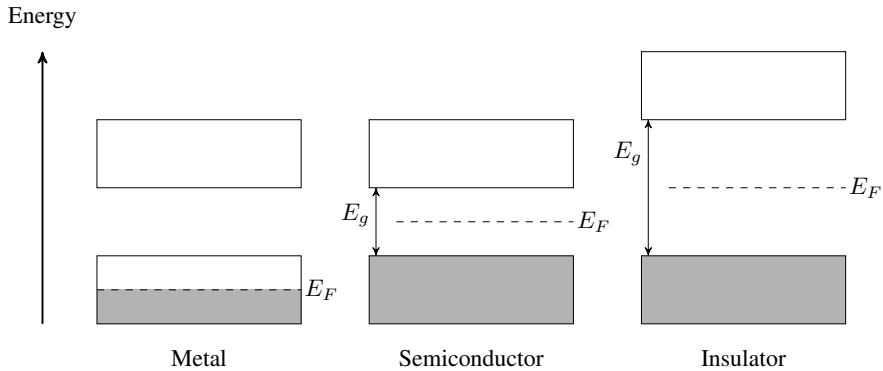
Figure 2.3: The band structure for the three types of solid state materials. E_F is the Fermi level, and E_g is the band gap. The grey enclosed areas represent states filled with electrons, while the white enclosed areas are empty states.

2.3.4 Energy bands

The Fermi level can be used to categorize solid materials. If the Fermi level lies inside an energy band, the solid material is a metal. If the Fermi level lies inside a band gap, it is either an insulator or a semiconductor depending on the width of the band gap. If the band gap is less than about 3-4 eV, it is categorized as a semiconductor, and if it is larger, it is categorized as an insulator [17]. In Figure 2.3, we see the distinction between the three types of solid state materials. Note that the Fermi level can lie anywhere in the band gap, even though it is placed in the middle in Figure 2.3 for both the semiconductor and the insulator. The energy band above the Fermi level is termed the *conduction band* (CB) and the band below is termed the *valence band* (VB). A Si solar cell is a semiconductor. In the context of band theory, the Fermi level E_F represents a hypothetical energy state with a 50% chance of being occupied by an electron. The band gap E_g on the other hand is an energy difference, the difference between the bottom of the conduction band and the top of the valence band. There are other energy gaps found in a material as well. For example E_X and E_Γ which are the energy differences from the top of the VB to the CB at the X and Γ high symmetry points in k-space, respectively. Figure 2.2 shows the position of these points in k-space in the first Brillouin zone.

2.3.5 Electrons in crystals

In a semiconductor at zero temperature, there can be no electron flow since all the electrons are in the completely filled VB without any nearby electron states to move into. Once the temperature increases, some electrons will become excited into the CB, and the material may conduct both an electron current in the CB, and a hole current in the VB. It is a convention to use the term hole and hole current in the VB, even though it is the electrons that are moving around. The hole simply represents an electron-vacancy in the VB, and makes calculations easier.

The energy of electrons in free space is given by

$$E = \frac{p^2}{2m_e} \tag{2.56}$$

where p is the momentum of the electron, and m_e its mass. Electron movement in the periodic lattice is slightly different than that of the free electron. Instead of adding the periodic potential in the energy expression (2.56), we redefine the mass into an "effective mass", given by

$$m^* = \frac{\hbar^2}{d^2E/d\mathbf{k}^2}. \tag{2.57}$$

The curvature of the band structure determines the effective mass of the electron, so we have included the potential in the momentum part of the energy expression. The convention in solid state physics is to use the electron wave vector instead of the momentum, they are related by $\mathbf{p} = \hbar\mathbf{k}$. We are interested in describing the electrons near the band gap, so we choose zero energy at the bottom of the CB,

$$E = \frac{\hbar^2}{2m_e^*}(\mathbf{k} - \mathbf{k}_0)^2 + E_c, \tag{2.58}$$

where $\mathbf{k}_0$ is the position of the bottom of the CB in $\mathbf{k}$-space, and E_c its energy. Equivalently, we can create an energy expression for the holes

$$E = \frac{\hbar^2}{2m_h^*}(\mathbf{k} - \mathbf{k}_0')^2 + E_v, \tag{2.59}$$

where E_v is the top of the valence band, and $\mathbf{k}_0'$ its position in $\mathbf{k}$-space. Exciting an electron from the VB to the CB requires energy, and if the position of the bottom of the CB and the top of the VB are at different $\mathbf{k}$-values, it also requires a change in momentum. An example of this is pure Si in the diamond lattice, where $\mathbf{k}_0' \neq \mathbf{k}_0$. We say that this semiconductor is an *indirect band gap semiconductor*. If $\mathbf{k}_0' = \mathbf{k}_0$, the material is a *direct band gap semiconductor*. GaAs is an example of a direct band gap semiconductor.

The Fermi-Dirac distribution describes the probability of occupying an energy state. To find the actual electron (and hole) distribution for a specific material, we have to include the available energy states of the material, the *density of states* (DOS) [17]. The band structure defines the DOS and together with the Fermi level, what type of material it is.

Another way to excite electrons from the valence band to the conduction band is by illumination, for example by sunlight. If an incoming photon's angular frequency ω is such that $\hbar\omega \geq E_g$, there is a chance that an electron will be excited from the VB to the CB where it can move around easily, so that the material may conduct a current. This is visualized in Figure 2.4. The light may excite electrons further up in the conduction band when the incoming light has higher energy. If this happens, they will diffuse down to the bottom of the conduction band, exciting phonons (vibrational modes) in the material.

The first solar cells (1st and 2nd generation) were *single gap solar cells*, p-n junctions with the same electron-exciting mechanism as described in Figure 2.4. The theoretical maximum efficiency for these kind of semiconductors is 40.7%. This is known as the Shockley-Queisser limit [2]. When addressing the maximum efficiency, we assume an operating solar cell at 25°C and incoming radiation from a perfect blackbody. For a complete explanation of the assumptions done for the maximum efficiency, see [18].
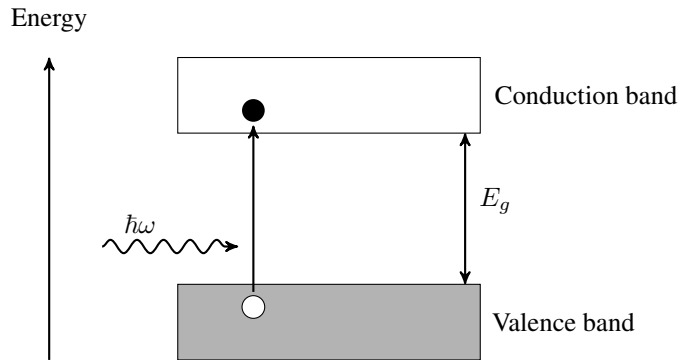
Figure 2.4: Exciting an electron from the VB to the CB by an incoming photon with energy $\hbar\omega$, leaving a hole in the VB.

2.3.6 Intermediate band solar cell

In 1997, a new type of solar cell was proposed by Antonio Luque and Antonio Martí, the *intermediate band solar cell* (IBSC). The idea is to add an additional energy band between the CB and the VB, the so-called *intermediate band* (IB). The theoretical maximum efficiency of an IBSC is 63.1% [2]. In equilibrium, the Fermi level lies inside the IB. The IB material is placed between a p-doped and an n-doped semiconductor, acting as selective contacts see Figure 2.5. The band structure for such a junction is visualized in Figure 2.6.
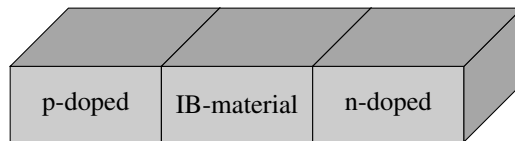
Figure 2.5: p-IB-n junction.

The reason for the increased efficiency lies in the electron-exciting mechanism. In addition to the photon frequencies that excite electrons straight from the VB to the CB, like in Figure 2.4, lower frequencies are also absorbed. These lower frequencies can excite electrons from the VB to the IB and from the IB to the CB. More photon frequencies absorbed yields a higher efficiency. The three excitation processes are illustrated in the middle of Figure 2.6 [2, 19].

Pure Si has a single band gap, but in this thesis, we will try to find some doping and/or vacancy configuration of Si that makes an IB appear. We will be using Ag and W as the doping atoms and will be looking at different concentrations, and unit cell configurations.

p-doped   IB-material   n-doped
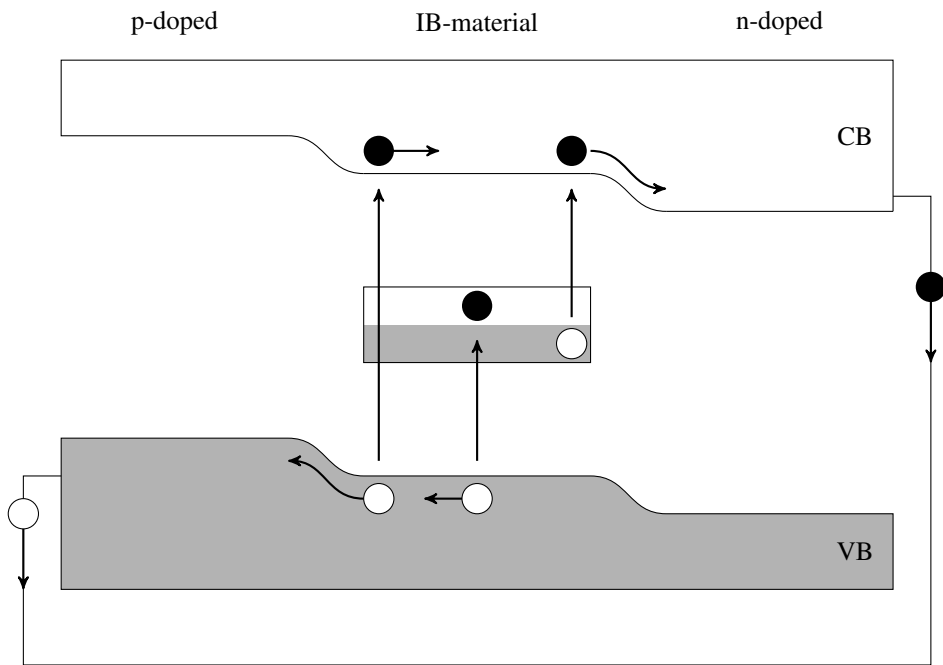
Figure 2.6: Energy bands of a p-IB-n junction and a depiction of the electron (black dots) and hole (white dots) currents. The three electron excitation mechanisms are shown in the middle of the figure.

Chapter 3

Computational Method

The BAND package for ADF (Amsterdam Density Functional) was used for all the DFT calculations in this thesis. Two other ADF packages called DFTB and MOPAC were also used. For more details on how the underlying theory is implemented in these program packages, see the SCM (Software for Chemistry & Materials) webpage [20].

3.1 Calculating the ground state

3.1.1 Basis sets

For a given k-value, the Bloch functions ψ_i^k are constructed from the atom-centered basis functions $\chi_j(\mathbf{r})$ in the following way:

$$\psi_i^k(\mathbf{r}) = \sum_j^J C_{ij}^k \phi_j^k(\mathbf{r}), \tag{3.1}$$

where

$$\phi_j^k(\mathbf{r}) = \sum_R e^{ikR} \chi_j(\mathbf{r} - \mathbf{R}). \tag{3.2}$$

Here, $\mathbf{R}$ is the lattice vector in real space and C_{ij}^k are the expansion coefficients. In a numerical implementation, J needs to be finite. In practice, this means that the wave functions cannot be exactly described since they belong to a function space that has infinite dimensions. The basis functions $\chi_j(\mathbf{r})$ are the product of a radial function $R(r)$ and a real spherical harmonic function $Z_m^l(\theta, \phi)$,

$$\chi_j(\mathbf{r}) = R(r) Z_m^l(\theta, \phi), \tag{3.3}$$

where r, θ and ϕ are the spherical coordinates centered at the nucleus, m and l are the magnetic and angular quantum numbers, respectively. j is the total angular momentum

quantum number. The basis functions are obtained by numerically solving the Kohn-Sham equations for isolated atoms. They are commonly known as *Slater type orbitals* [21, 22].

Here is an explanation of the naming convention used for the different basis sets typically seen in computational quantum mechanics: SZ (single zeta): One basis function for each atomic orbital. DZ (double zeta): Two basis functions for each atomic orbital. And so on for TZ (triple zeta) and QZ (quadruple zeta). When atoms approach one another, the orbitals tend to shift to one side or the other, creating a polarized orbital state. Generally, to polarize a basis function having angular momentum l, mix it with one or more basis functions with angular momentum $l+1$. For example, using three basis functions for each atomic orbital with angular momentum l, and mixing them with two basis functions with angular momentum $l+1$ would be called, in short hand notation, TZ2P [23]. In this thesis, we use the basis sets: SZ, DZ, DZP, TZP, TZ2P, QZ4P. We will use different basis sets for the same system (pure Si in the cubic diamond lattice) to find the best candidate for further analysis for several doping and impurity configurations when it comes to computational time vs accuracy.

3.1.2 Solving the Kohn-Sham equations

In Heisenbergs matrix formulation of quantum mechanics, the Schrödinger equation (eigenvalue problem) can be written as a matrix diagonalization problem [24]. Diagonalizing a matrix is a problem well suited for a numerical solution and there is a manifold of numerical libraries optimized for this kind of task. Most computational quantum mechanical programs use this method, including ADF. Solving the Kohn-Sham equations (2.29) is now a diagonalization problem, meaning that the single particle Kohn-Sham equations,

$$\hat{H}_{\text{KS}}\psi_i(\mathbf{r}) \equiv \left[-\frac{\hbar^2}{2m}\nabla^2 + V_{\text{ext}}(\mathbf{r}) + V_{\text{H}}(\mathbf{r}) + V_{\text{XC}}(\mathbf{r}) \right]\psi_i(\mathbf{r}) = \epsilon_i\psi_i(\mathbf{r}), \qquad (3.4)$$

become

$$\begin{bmatrix} 0 \\ \vdots \\ \vdots \\ 0 \end{bmatrix} = \begin{bmatrix} A_{11,i} & A_{12,i} & \cdots & A_{1J,i} \\ A_{21,i} & A_{22,i} & \cdots & A_{2J,i} \\ \vdots & \vdots & \ddots & \vdots \\ A_{J1,i} & A_{J2,i} & \cdots & A_{JJ,i} \end{bmatrix} \begin{bmatrix} C_{i1} \\ \vdots \\ C_{iJ} \end{bmatrix}, \qquad (3.5)$$

where

$$A_{nm,i} = \langle\phi_n|\hat{H}_{\text{KS}}|\phi_m\rangle - \epsilon_i\langle\phi_n|\phi_m\rangle. \qquad (3.6)$$

At first glance, it may look straightforward to solve this problem using a finite difference scheme on the Laplacian (kinetic term), evaluate the potentials and then use any standard library for diagonalizing the resulting matrix. There is, however, another obstacle we need to pass. In order to find the eigenstates, ψ_i, and the eigenvalues, ϵ_i, we need to diagonalize the Hamiltonian. To diagonalize the Hamiltonian, we need to evaluate the Hartree potential and the exchange-correlation potential. To evaluate these potentials, we need to know the electron density $n(\mathbf{r}) = 2\sum_{i=1}^{N}\psi_i^*(\mathbf{r})\psi_i(\mathbf{r})$, but here we need to know the wave functions which is what we wanted to find in the first place. To break this cycle, we use what is known as a *self-cosistent field method*. The idea is to make an initial guess on the electron density, then solve the Kohn-Sham equations and see if the wave functions create the same

electron density, under some convergence criterion. If they do not, then make a different guess on the electron density and repeat the process until convergence [3, 24]. The process is illustrated in Figure 3.1.
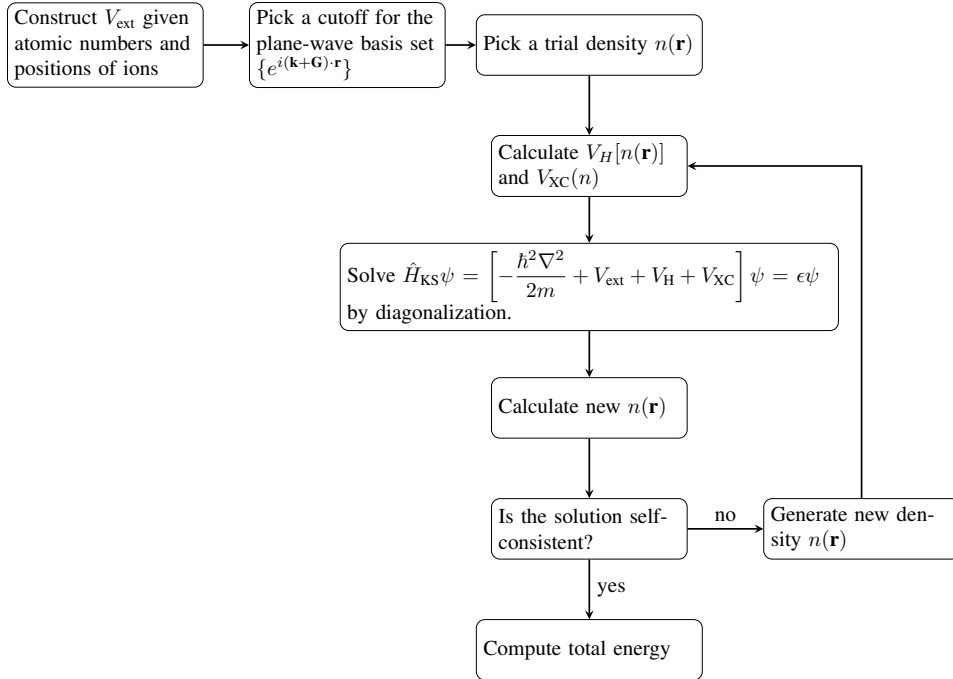
Figure 3.1: Flowchart describing how to solve the Kohn-Sham equations iteratively. Image inspired by [25].

3.1.3 Functionals

The functionals used in this thesis are presented in Table 3.1. First we will compare the

Table 3.1: The different functionals used in this thesis. X is for the exchange part and C is for the correlation part of the functional.

Approximation	Functional	Authors	Reference
LDA	VWN	X: Slater	[26]
		C: Vosko, Wilk, Nusair	[27]
GGA	PW91	Perdew, Wang	[28], [11]
GGA	PBE	Perdew, Burke, Ernzerhof	[29]
GGA	PBEsol	Perdew, Ruzsinszky et al.	[30]
MetaGGA	M06-L	Zhao, Truhlar	[31], [32]
MetaGGA	TPSS	Tao, Perdew, Staroverov, Scuseria	[14], [33]

functionals for the same system (pure Si in the cubic diamond lattice), to find the best candidate for further analysis for several doping and impurity configurations.

3.1.4 The frozen core approximation

A way to speed up the calculations is to use what is known as a "frozen core". The innermost electrons are kept fixed (frozen) to their optimal position in a spherical potential (not affected by neighboring atoms), and not varied in the process of finding the ground state. This can be justified by arguing that the it is the outermost electrons that are the most important for electronic structure calculations. In BAND, these innermost one-electron orbitals for each atom type are saved and need not be calculated for each system under consideration, reducing the computational time. BAND uses the options `Small`, `Medium`, and `Large` when specifying the frozen core. In this thesis, we will use a `Small` frozen core [34, 35].

3.1.5 The Hubbard U parameter

DFT electronic structure calculations tend to underestimate the band gap of a semiconductor. A way to cope with this error, is to add an additional term in the Hamiltonian, a so called Hubbard U term. After finding the functional that best match experimental results, we will modify the Hamiltonian with a Hubbard term (GGA+U) to improve the band gap description even further. In ADF, the energy correction is written as an energy functional in the following way [36, 37]:

$$E_U[\{n^{I\sigma}\}] = \frac{U}{2} \sum_{I,\sigma} \sum_i \lambda_i^{I\sigma}(1 - \lambda_i^{I\sigma}). \tag{3.7}$$

Here, σ runs over the two spin states at atom site I. The quantity $\lambda_i^{I\sigma}$ represents the occupation of orbital i with spin σ at atom site I. $\lambda \approx 1$ represents a fully occupied

orbital, and $\lambda \approx 0$ represents a completely empty orbital, $0 \leq \lambda \leq 1$. This energy functional is added to the total energy functional (2.28). If $U > 0$, the energy increases if two states are close to one another. If $U < 0$, the energy increases if two states are further away from one another. To get a wider band gap, we let $U > 0$, forcing the electrons to get more smeared out in order to gain the lowest possible energy. U is called the Hubbard parameter and represents the strength of this electron-electron repulsion/attraction. For a more detailed explanation of the Hubbard term implemented in ADF, see [36].

3.1.6 Mulliken population analysis

Finding the partial contribution to the DOS from the different elements is of interest to the results of this thesis. A way to do this use to use the *Mulliken population analysis* [38]. The main idea is to relate the total number of electrons to the density matrix and overlap integrals. Since there is no operator corresponding to the atomic charge, any partitioning method, such as Mulliken, can give arbitrary results, even though the method is uniquely defined [38, 39].

3.1.7 DFTB

When investigating some of the largest systems in this thesis, we will use an approximative version of DFT, called Density Functional based Tight-Binding (DFTB). The method does not give as accurate results as regular DFT, but is about 2-3 orders of magnitude faster with respect to computational time. DFTB is based on DFT, but uses parameters, so it's not a first principles theory, like DFT. Most of these parameters are, however, based on pure DFT, so they have a theoretically solid basis. The main idea behind DFTB is to consider the electrons as tightly bound, and treating electron-electron interactions with neighboring atoms merely as a perturbation. The Hamiltonian itself is now a parametrized matrix, depending on internuclear distances [40] [41]. The pre-calculated parameters (Slater-Koster files) we will use in the DFTB calculations, using the DFTB package for ADF, are gathered from [42]. This library/parameter set is called `hyb-0-2`.

3.1.8 MOPAC

When investigating some systems in which there are no DFTB parameters available, we will use the MOPAC (Molecular Orbital PACkage) suite for ADF. It is a semi-empirical method based on the NDDO (neglect of diatomic differential overlap) formalism. It should be noted that MOPAC uses a minimal basis set, and results should be presented with caution. In our results, we will use MOPAC to optimize the geometry for the largest systems where there are no DFTB parameters available, then use standard DFT to calculate the energy and the DOS.

4

Results and Discussion

4.1 Properties of Si and functional comparison

In this section, properties of bulk Si in the cubic diamond lattice are presented. The candidate with best results is then modified with a Hubbard Hamiltonian (GGA+U) to provide a better description of the band gap. A visualization of Si in the cubic diamond lattice is presented in Figure 4.1.
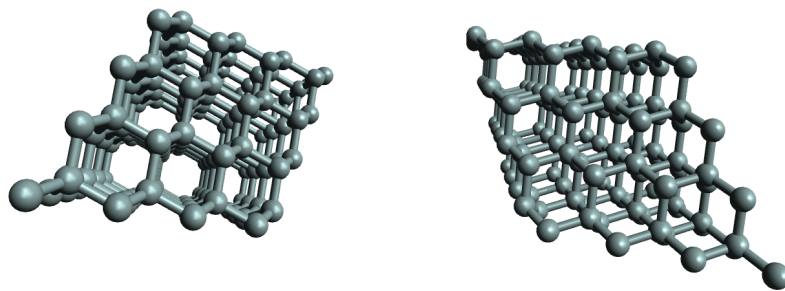
Figure 4.1: Two different perspectives of Si in the cubic diamond lattice.

In Table 4.1 a comparison of different physical quantities using different fucntionals is presented. It is clear that DFT underestimates the band gap, especially in the local density approximation. The M06-L functional in the meta-GGA gives by far the best estimate when comparing with experimental results. This comes as no surprise, since the M06-L functional is designed with the band gap problem in mind [15]. All the functionals tested here give a good estimate of the lattice parameter. It should be noted that the calculations are assuming a temperature of 0 K, where the experimental band gap is 1.17 eV, while the band gap at room temperature is about 1.12 eV [43].

Table 4.1: Energy gap and lattice constant calculated from the different functionals and their experimental values as found by [43]. The numerical quality is set to good and a small frozen core is used. The basis set is TZ2P.

Method	Functional	E_g (eV)	$E_g/E_{g,\text{expt.}}(\%)$	a (Å)	$a/a_{\text{expt.}}(\%)$
expt.	-	1.17	-	5.43	-
LDA	VWN	0.53	45%	5.38	99%
GGA	PW91	0.65	55%	5.46	101%
GGA	PBE	0.63	54%	5.46	101%
GGA	PBEsol	0.51	44%	5.42	100%
Meta-GGA	M06-L	1.05	90%	5.41	100%
Meta-GGA	TPSS	0.71	61%	5.45	100%

The band gaps are energy differences in the band structure. Absolute energies in this chapter, for example DOS plots, are adjusted such that $E = 0$ represents the vacuum level, alternatively the energy of a free particle. In Figure 4.2 we see the DOS of Si in the diamond lattice when using the different functionals. The unit of the DOS in this thesis is presented as [number of states/unit cell], a dimensionless quantity. The true DOS would have dimension [1/energy]. However, BAND produces a histogram of the DOS within an energy interval. Note that the dimension is per unit cell, so increasing the unit cell size produces larger DOS values [44]. It becomes clear that all the functionals provide the same trends for the DOS. The DOS from the meta-GGA functionals, M06-L and TPSS, is shifted away from the band gap region compared to the other functionals. They are also the functionals that provide the band gaps that are closest to the experimental values, see Table 4.1. Even though they look quite the same, the band gap is a critical region where the DOS needs to be precise and we see that the M06-L functional provides the biggest band gap. The band gap is seen at just below -5 eV, where the DOS equals zero.

Both the meta-GGA functionals, M06-L and TPSS, are computationally too demanding, especially when the system size is scaled up. Even though the M06-L functional provides the best description of the band gap, it it not feasible for this thesis. So for the further calculations, we choose the functional in the GGA which gave the best results for the band gap of pure Si, the PW91 functional, see Table 4.1.

In Figure 4.3 we use the PW91 functional with different basis sets. They all provide the same trends. When increasing the basis size, the DOS on the left side of the band gap is mostly shifted more to the right. On the right side of the band gap, the DOS seems to shift more to the left when increasing the basis size. The TZ2P and QZ4P are almost identical, especially around the band gap region. The QZ4P is computationally a lot more demanding than all the other basis sets, so by weighing accuracy vs computational time, the TZ2P basis set will be used for the rest of the calculations in this thesis. From now on, we denote the PW91 functional with a TZ2P basis set, a small frozen core and the numerical quality set to "good" as the "standard setup".
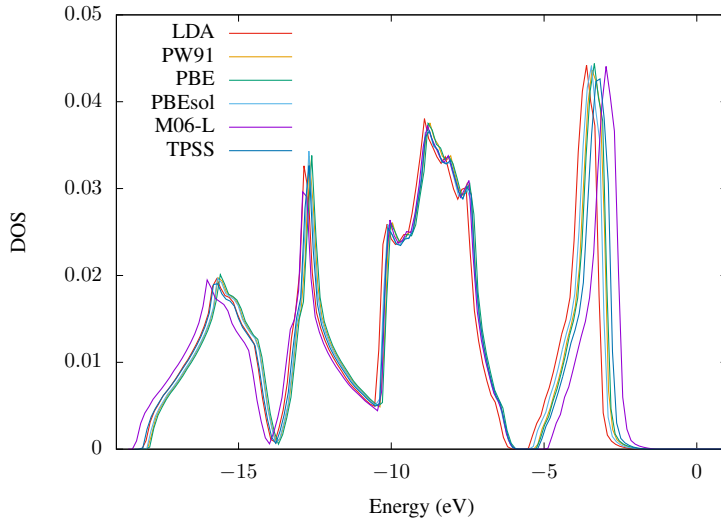
Figure 4.2: DOS of Si using different functionals. Additional results from the different functionals are presented in Table 4.1. A small frozen core is used and the basis set is TZ2P. The numerical quality is set to good.
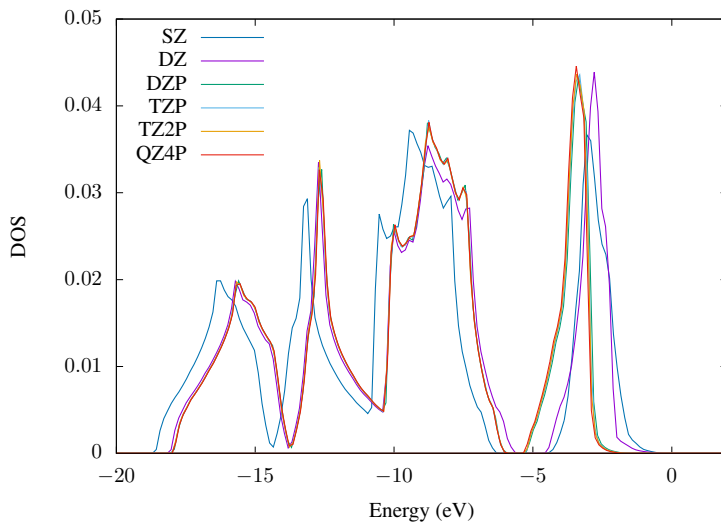
Figure 4.3: DOS of Si using the PW91 functional with different basis sets. An explanation of the basis set naming convention is found in subsection 3.1.1. A small frozen core is used and the numerical quality is set to good.

In Figure 4.4 we see the partial contributions to the total density of states. It is clear that the p-states are the most dominant around the band gap, which is the most interesting area for this thesis. The Fermi level in the standard setup lies approximately in the middle of the band gap, with a value of $E_F = -5.6865$ eV.
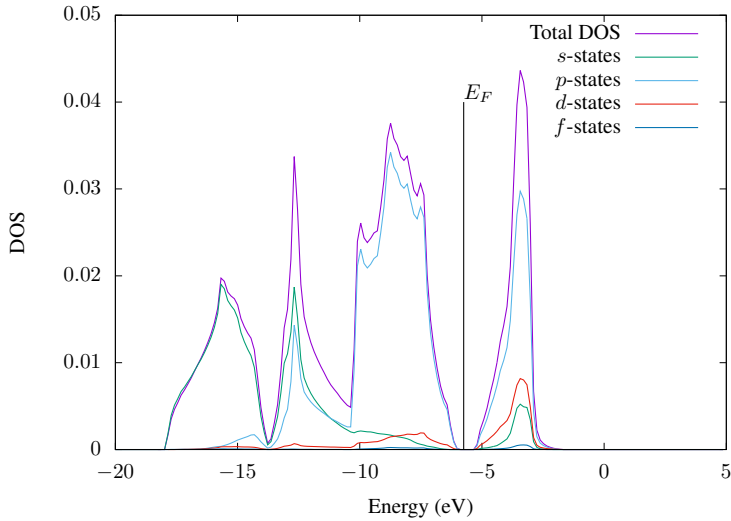
Figure 4.4: Partial and total DOS of Si using the standard setup. The Fermi level is $E_F = -5.6865$ eV and lies inside the band gap. The p-states make up most the total DOS around the band gap.

4.1.1 Hubbard model correction

To make a better description of the band gap we include a Hubbard like term in the Hamiltonian. In this way, we can use the GGA approximation with its quick computational time and get a better description of the band gap, instead of using, say, a meta-GGA functional. Adding the Hubbard term in the Hamiltonian only slightly increases the computational time the GGA, making it feasible. From Figure 4.4 we see that the p-states are the most dominant around the band gap, and therefore the most interesting states for this analysis. We therefore let the Hubbard term, equation (3.7), include only the p-states in the system.

U	E_g
0.027	0.655
0.136	0.674
0.272	0.688
0.816	0.729
1.361	0.771
1.633	0.810
1.905	0.859
2.177	0.918
2.449	0.987
2.585	1.023
2.721	1.062
2.993	1.145
3.020	1.153
3.048	1.162
3.075	**1.171**
3.102	1.179
3.265	1.234
3.537	1.329
3.810	1.427
4.082	1.525
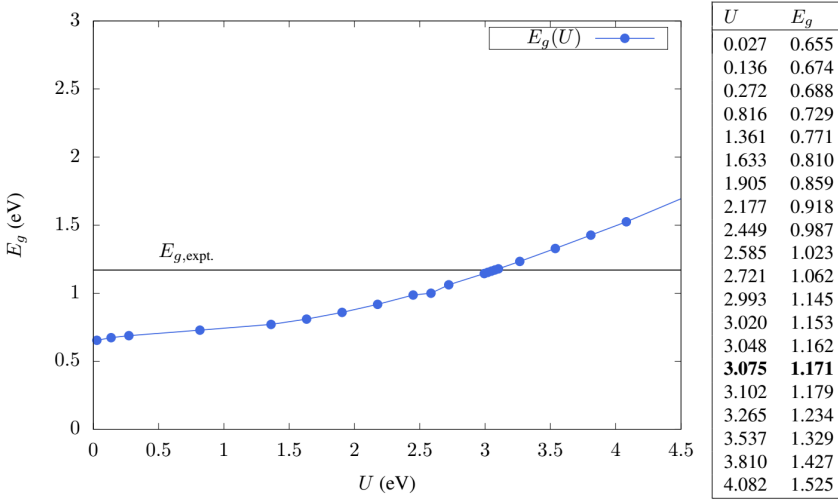
Figure 4.5: The band gap, E_g, as a function of the Hubbard parameter U using the standard setup. The data points are visualized in the table to the right. All units are eV.

In Figure 4.5, we see the band gap as a function of the Hubbard U-parameter and a table of the calculated values. At $U = 3.075$ eV, the band gap is $E_g = 1.171$ eV, close to 100 % the experimental value. Even though the band gap value may equal the experimental value at a larger value of U, the lowest U-value will make the system have lowest energy and will therefore be more probable. In addition, this is a semi-empirical correction to make a better description of the band gap, so choosing a larger U-value would make the results deviate more from DFT made from first principles. $U = 3.075$ is of the same order of magnitude as proposed by [45].

In Figure 4.6 we see the band structure of Si calculated with the PW91 functional. The band structure provides the same trends as other calculations based on different methods than DFT [46–48], see Figure 4.7. Comparing the most important region in k-space for this semiconductor, the region between the Γ point and the X point, wee see that the DFT calculation using the PW91 functional provides the same behavior as both Figure 4.7 **(a)** and **(b)**, partly validating our DFT results. In all these cases, the lowest energy point in the CB lies close to the X point when moving from the Γ point. This point is marked with E_g in Figure 4.6, this energy difference is the band gap.
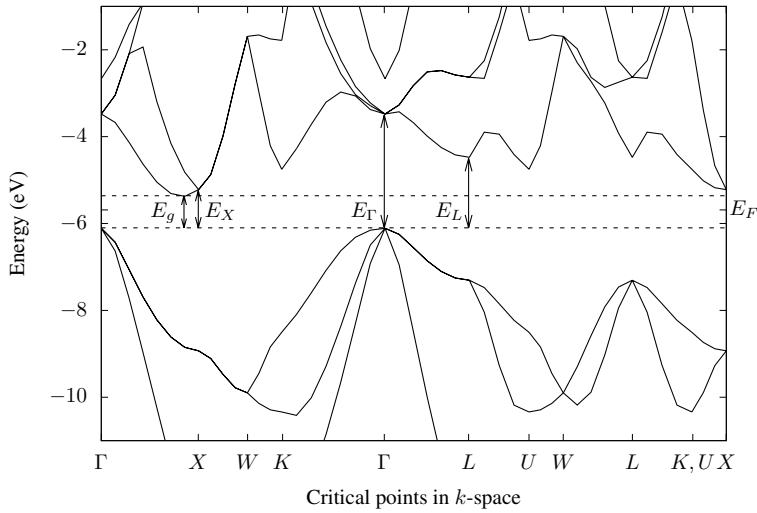
Figure 4.6: The band structure of Si using the standard setup. Some energy gaps are marked with double arrows. The lower and upper dashed horizontal lines represent the top of the VB and bottom of the CB, respectively. The Fermi level is $E_F = -5.6865$ eV.
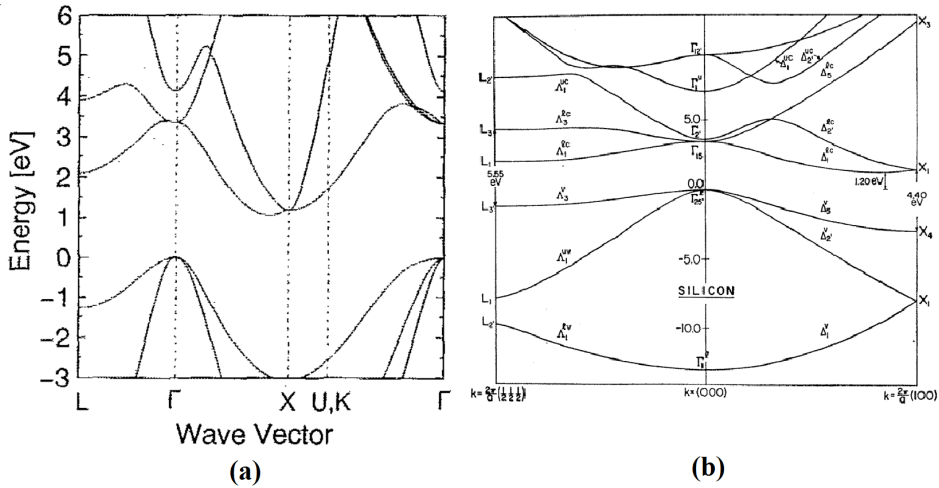
Figure 4.7: **(a)** The band structure of Si calculated by an empirical local pseudopotential method, taken from [48]. **(b)** The band structure calculated by the "$\mathbf{k} \cdot \mathbf{p}$" method, taken from [46].

In Figure 4.8 we see the band structure for the same calculation, but the Hubbard U-term is included, with $U = 3.075$ eV. Some energy values and the lattice parameter are presented in Table 4.2. A comparison of the DOS with and without the Hubbard term is shown in Figure 4.9, and we see that it provides the same qualitative trends as without

the Hubbard term, but the DOS seems rather stretched. This stretching makes it differ vastly from any of the other "pure" DFT functionals in Figure 4.2. Upon inspection of the band structure in Figure 4.8, we also see the "stretching" of the band structure. A crucial observation is that the high symmetry points are broken. The energy levels have split, for example near the Γ point, it has split into three separate energy levels. One might think that maybe the spin-orbit coupling might have become noticeable once the Hubbard term was included, but there are no relativistic effects in play in this calculation. A separate calculation of the spin-orbit splitting was done, Figure 4.10, and we see that the energy levels split at about one order of magnitude smaller than that of the Hubbard term splitting.
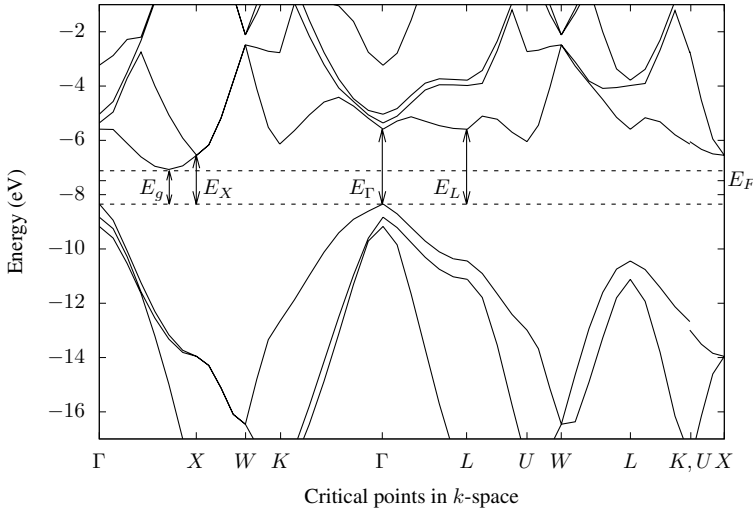
Figure 4.8: The band structure of Si using the PW91 functional with a Hubbard U correction, $U = 3.075$ eV. Some energy gaps are marked with double arrows. The lower and upper dashed horizontal lines represent the top of the VB and bottom of the CB, respectively. A small frozen core was used and the basis set is TZ2P. The Fermi level is $E_F = -7.4835$ eV.

From Table 4.2 we see that the lattice parameter, a, when using the Hubbard parameter is 92% of the experimental value. This is a lot lower than all the unmodified GGA functionals, even the LDA provides a good lattice parameter, as presented in Table 4.1. We conclude that the results with Hubbard term included is rather invalid, since they break these important physical symmetry properties. So for the most part of the DFT calculations further in this thesis, we will omit the Hubbard term in the Hamiltonian. A recent discussion actually weighs against the usage of the Hubbard term in the Hamiltonian for band structure calculations [49].
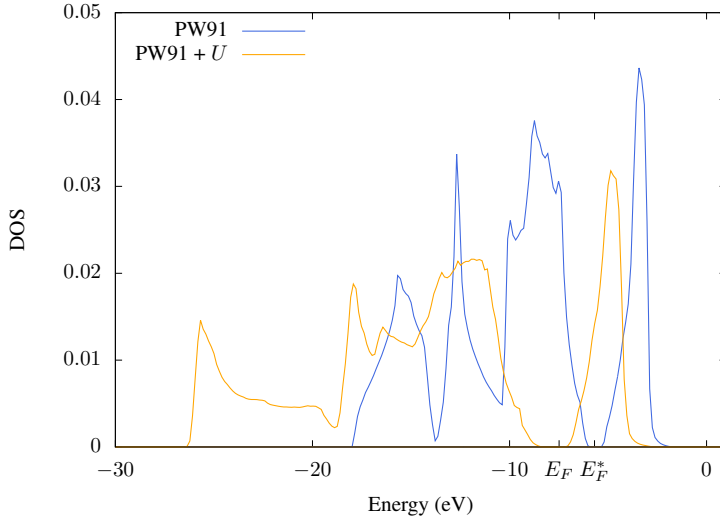
Figure 4.9: DOS of Si using the PW91 functional with and without the Hubbard U correction. A small frozen core was used and the basis set is TZ2P. E_F^* is the Fermi level when using PW91, and E_F when using PW91 + U.

Table 4.2: Some electronic properties calculated from the different functionals and its experimental value as found by [43]. The numerical quality is set to good and a small frozen core is used. The basis set is TZ2P. $U = 3.075$ eV. The energy gaps are given in eV and the lattice constant is given in Ångstrøm.

property	expt.	PW91 calc.	% of expt.	PW91 + U calc.	% of expt.
E_g	1.17	0.65	55%	1.17	100%
E_Γ	3.34	2.54	76%	2.76	83%
E_X	1.25	0.79	63%	1.80	144%
E_L	2.40	1.53	64%	2.76	115%
a	5.43	5.46	101%	4.98	92%
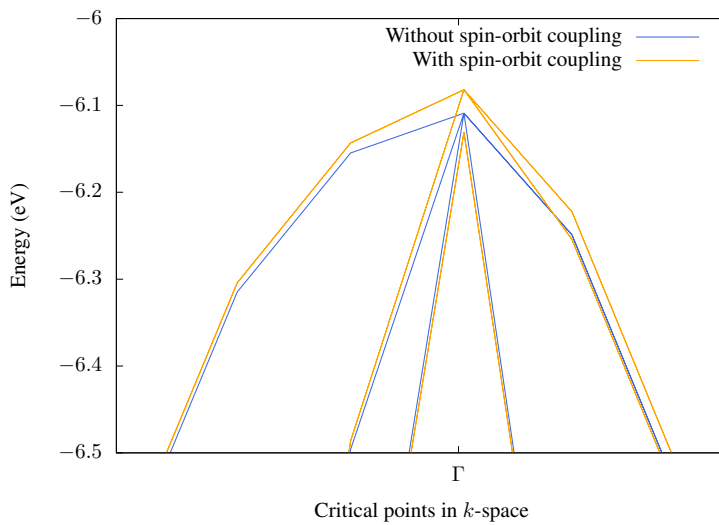
Figure 4.10: Top of the valence band at the Γ high symmetry point in k-space visualized with and without spin-orbit coupling.

4.2 Ag-doped Si

In this section, we will look at Ag-doped Si, still in the cubic diamond lattice. In the first subsection, DFT results are presented with a unit cell size ranging from 4 to 16 atoms and doping concentrations ranging from 25 % to 6.25 %. In the second subsection, we look at larger unit cells using DFTB, and get the doping concentration even further down. In both sections we look at several unit cell configurations and see how this affects the DOS.

4.2.1 Properties of Ag

First, some properties of pure Ag in the cubic diamond lattice with the same lattice parameter as Si. The DOS and its partial contributions are presented in Figure 4.11. We see that
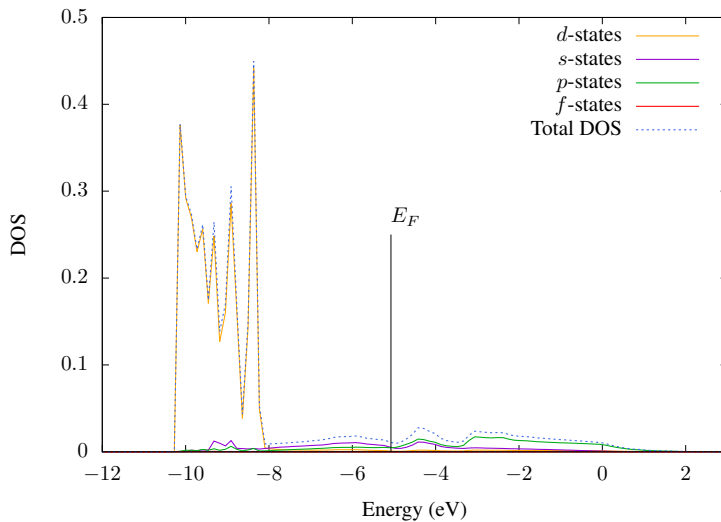
Figure 4.11: DOS as a function of energy for pure Ag in the cubic diamond lattice using the standard setup. The lattice parameter is set to the experimental value of Si in the diamond lattice. The Fermi level is $E_F = -5.0721$ eV.

the material is a metal, since the Fermi level lies inside a band. A region with high DOS is apparent at about -8 to -10 eV, consisting almost entirely of d-states. When appearing naturally, Ag forms in the FCC lattice, not in the diamond lattice like Si. In Figure 4.12, a DFT calculation is run with Ag in the FCC lattice using the standard setup. The lattice parameter was set to $a = 4.086$ Å, as found by [50]. We see the same qualitative trends as in the diamond lattice, however the high DOS region is shifted about 2 eV in the negative energy direction. The region is also "stretched" out to about twice the area. The absolute value of the DOS is "per unit cell", and the unit cell size is different, so directly comparing the values from the two lattices does not make sense. However, the diamond lattice can be modeled as a FCC lattice with a 2-atomic basis, so one could expect the DOS to be about twice as high in the diamond lattice compared to the FCC lattice. By inspection of the

two figures, we see that Ag in the diamond lattice reaches about 3-4 times as high in the FCC lattice. The Fermi level in the diamond lattice is about 0.8 eV larger than in the FCC lattice.
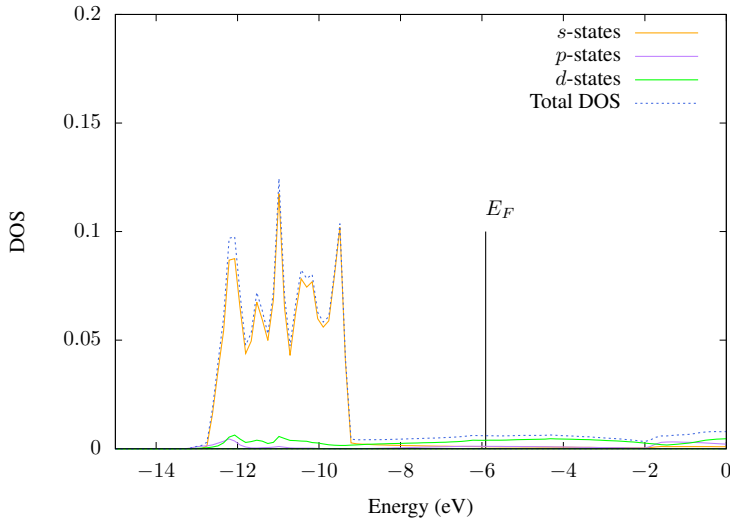
Figure 4.12: DOS as a function of energy for pure Ag in the FCC lattice using the standard setup. The lattice parameter is set to the experimental value of Ag in the FCC lattice. The Fermi level is $E_F = -5.9082$ eV.

4.2.2 DFT calculations

The simplest way to dope Si by 25 % of Ag is to use a basis like the one in Figure 4.13. Due to symmetry when repeating the lattice, it does not matter which one of the four atoms is replaced with Ag, all would yield the same lattice and results. The DOS of this system is shown in Figure 4.14

We see that the doped material is a metal. However there is a gap in the energy just above -15 eV. It is apparent that there is a DOS spike just below -10 eV which originates from the Ag states, even though it has a slightly different energy.

In Figure 4.15 we compare the **(a)** LDA, **(b)** meta-GGA: M06-L, **(c)** GGA:PW91, and **(d)** the GGA:PW91 + U. They all provide the same basic trends, but **(d)** is quite stretched at the "tail" below -15 eV, just as with the calculation on pure Si.

We will now look at 25 % doping concentration, but with an increased unit cell size, making more distinct configurations possible. There is a manifold of configurations when making the basis, some degenerate. In Figure 4.16, we see some of these configurations and, in Figure 4.17 and Figure 4.18, the corresponding DOS. For example configuration 3 and 6 leads to the same lattice when repeating the unit cell, and this can also be seen in the DOS for these configurations. The same goes for configuration 2 and 7. We can notice that there are some differences in some of the configurations. They all provide a clear peak
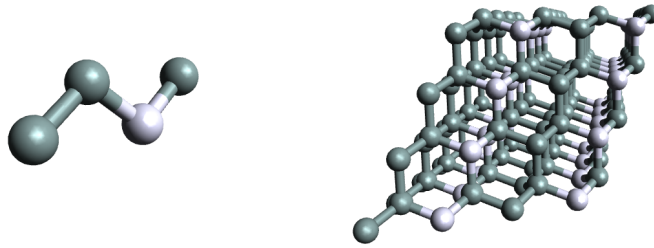
Figure 4.13: Ag-doped Si with a doping concentration of 25 %. The unit cell is visualized on the left and a periodic view is visualized on the right.
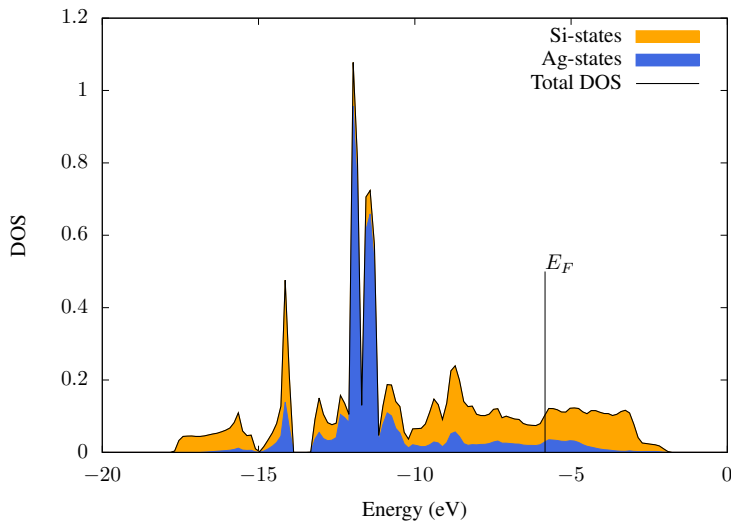
Figure 4.14: DOS as a function of energy for Ag-doped Si with a doping concentration of 25% using the standard setup. The Fermi level is $E_F = -5.8314$ eV.

just below -10 eV, however, they weigh the partial DOS from the two elements differently following the Mulliken population analysis. In, for example, config. 6, the peak consists of about 50/50 Ag/Si, but in config. 4, the Ag contribution is almost negligible compared to Si. In addition, in config. 2 and 7, which are the same systems by symmetry, we see that the Ag states are weighted slightly different, in a small area just below the band gap (just above -15 eV). The Ag states (blue area) are a bit higher in config. 2 than in config. 7. This shows the weakness of the Mulliken population analysis method. That the Mulliken population analysis has its weaknesses is well known, even Mulliken himself pointed out that the method has serious shortcomings [39]. We conclude that we cannot really say
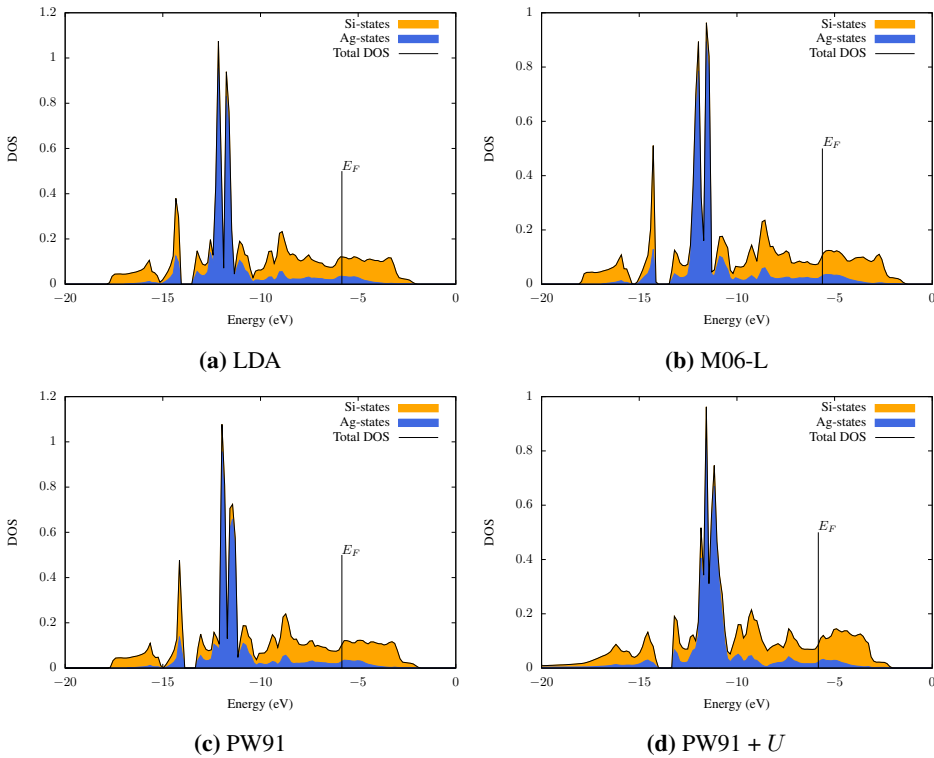
Figure 4.15: DOS as a function of energy for Ag-doped Si with a doping concentration of 25% using different functionals. Standard setup.

which elements contribute to which states with certainty.

It would be difficult to manufacture a perfect lattice such as these systems. A more realistic crystal with 25 % doping concentration will consist of various regions with these different configurations. A way to realistically create this system and its DOS along with its Fermi level is to make a virtual unit cell that is a linear combination of the 8 different unit cell configurations, where each sub-system is weighted by its Boltzmann factor. The "master-DOS" for the 25 % Ag doped Si crystal is presented in Figure 4.19.

We recognize the patterns from all the 8 configurations. All the 8 configurations had about the same energy and the same Boltzmann weight. The Boltzmann weights and the partition function were calculated with the temperature set to 298 K (room temperature), even though DFT calculations themselves assume 0 K. This was done since the room temperature distribution for a system is more realistic for an operating solar cell, even though the DFT calculations have to be done at 0 K in the BAND program.
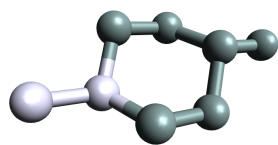
(a) Config. 1
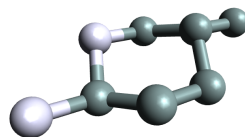
(b) Config. 2
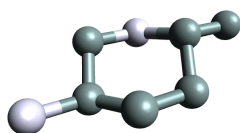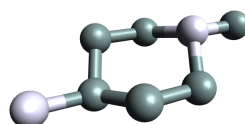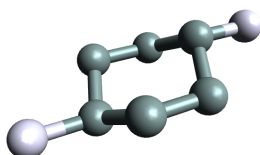
(c) Config. 3
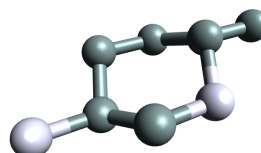
(d) Config. 4
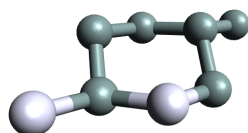
(e) Config. 5
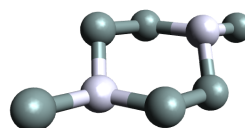
(f) Config. 6

(g) Config. 7

(h) Config. 8

Figure 4.16: Several unit cell configurations for Ag-doped Si with a doping concentration of 25%.

(a) Config. 1

(b) Config. 2

(c) Config. 3

(d) Config. 4
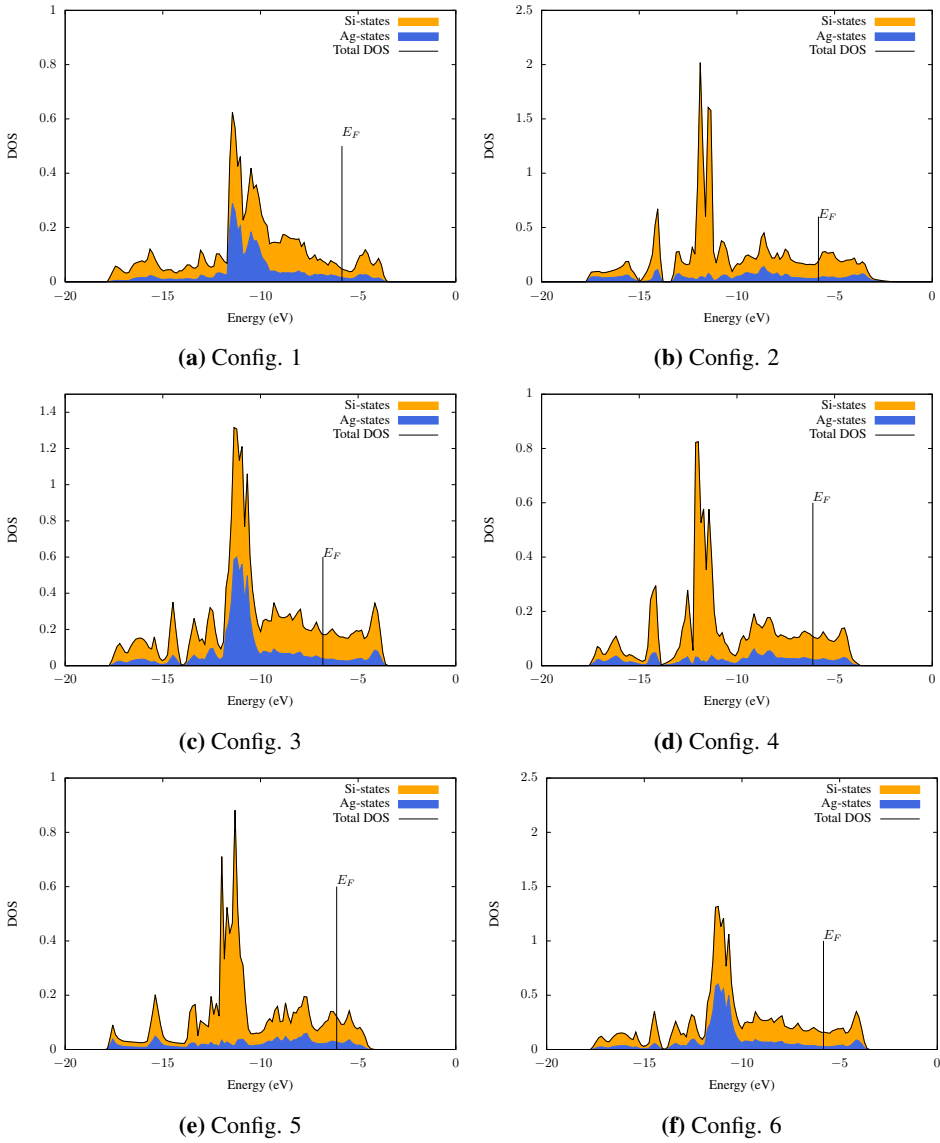
(e) Config. 5

(f) Config. 6

Figure 4.17: DOS as a function of energy for Ag-doped Si with a doping concentration of 25% using different unit cell configurations with the standard setup.

(a) Config. 7 **(b)** Config. 8
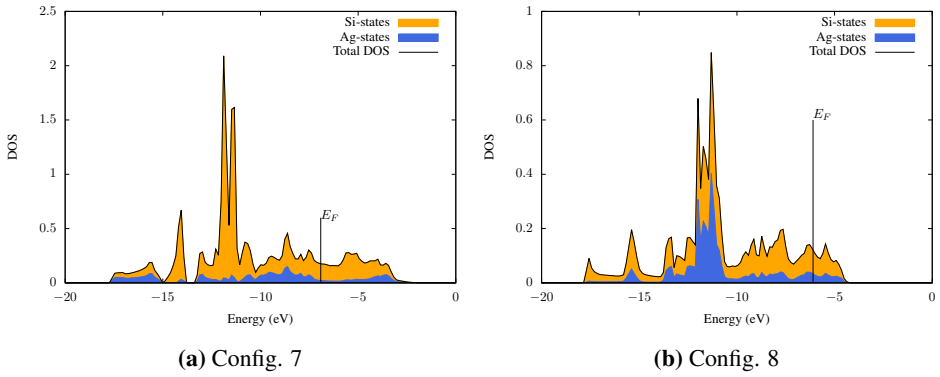
Figure 4.18: DOS as a function of energy for Ag-doped Si with a doping concentration of 25 % using different unit cell configurations with the standard setup.
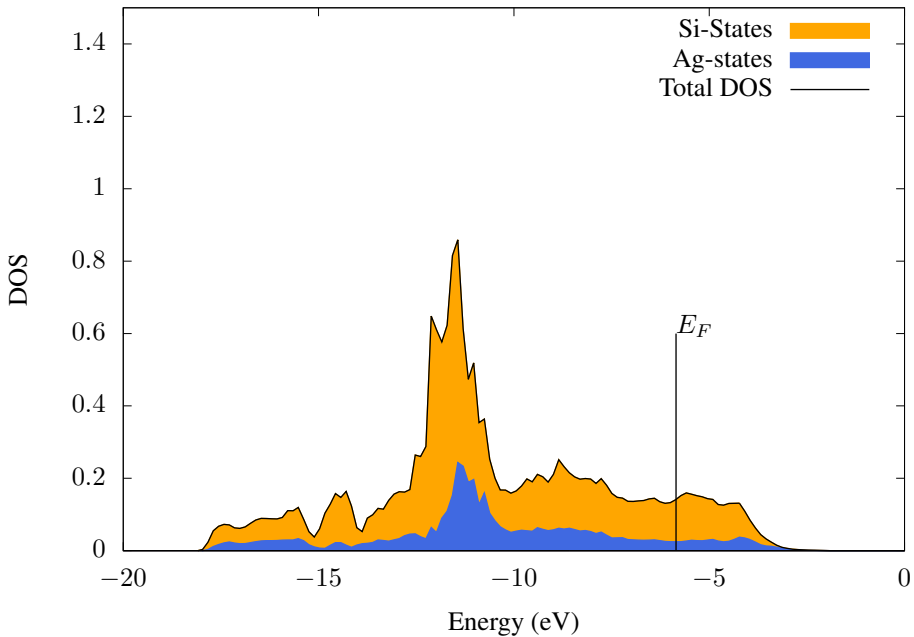
Figure 4.19: Boltzmann weighted DOS as a function of energy for Ag-doped Si with a doping concentration of 25%. Standard setup.

Increasing the unit cell size even further, we dope the material by 6.25 %, Figure 4.20. In Figure 4.21 the DOS of a 16-atomic unit cell is shown, where one of the 16 Si atoms is replaced by an Ag atom. The material is a metal, but there is a band gap which is slightly closer to that of pure Si than that of the ones with 25% doping concentration. The Ag states contribute much less here than with 25 % doping, as expected by lowering the concentration.
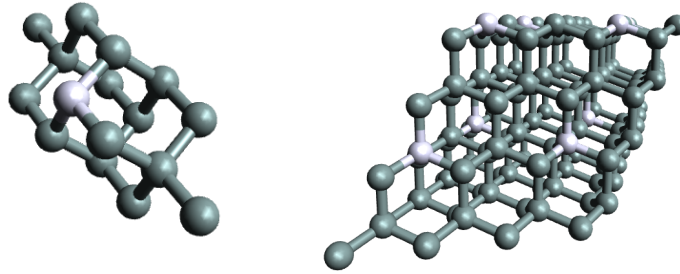

Figure 4.20: Ag-doped Si with a doping concentration of 6.25 %. The unit cell is visualized on the left and a periodic view is visualized on the right.
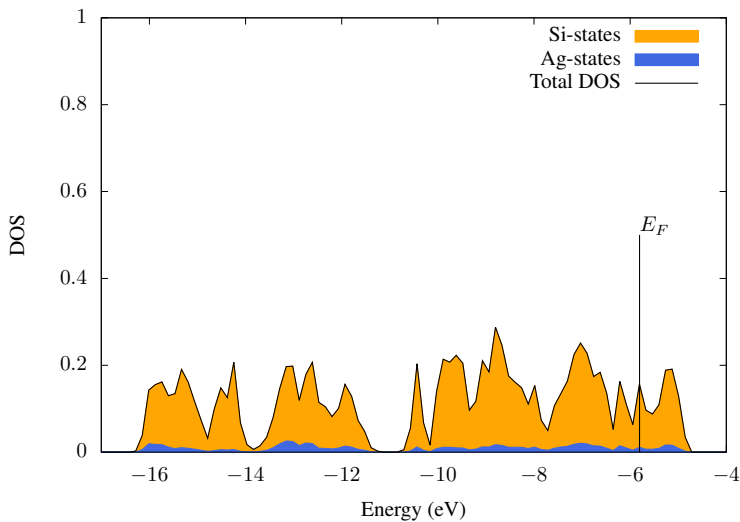
Figure 4.21: DOS as a function of energy for Ag-doped Si with a doping concentration of 6.25% using the standard setup. The Fermi level is $E_F = -5.6235$ eV.

When only one doping atom is used, the placement in the unit cell is irrelevant, but when adding several doping atoms, the relative placement matters. In Figure 4.22 6 dif-

ferent unit cell configurations are shown, and their respective DOS are presented in Figure 4.23. All configurations show a clear DOS spike just below -10 eV, indicating that we are dealing with Ag. We see again that the Mulliken population analysis provides rather arbitrary partial DOS. In Figure 4.23 there seems to be a region just above -15 eV where the DOS is quite low. However there is no band gap. A "master-DOS" where the 6 configurations are Boltzmann weighted is shown in Figure 4.24. The material is a metal, and there are no signs of a band gap.

(a) Config. 1

(b) Config. 2

(c) Config. 3

(d) Config. 4
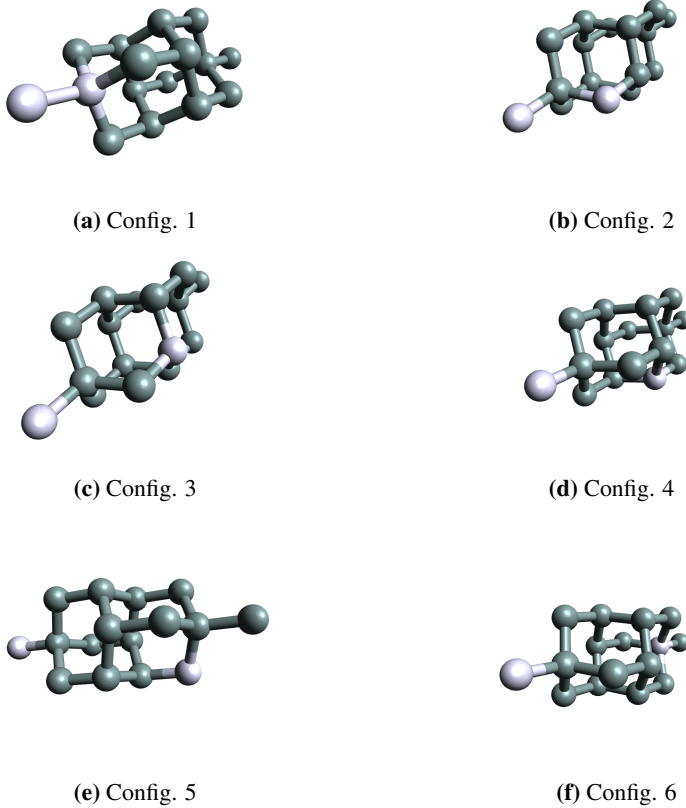
(e) Config. 5

(f) Config. 6

Figure 4.22: Several unit cell configurations for Ag-doped Si with a doping concentration of 12.5%.

(a) Config. 1

(b) Config. 2

(c) Config. 3

(d) Config. 4
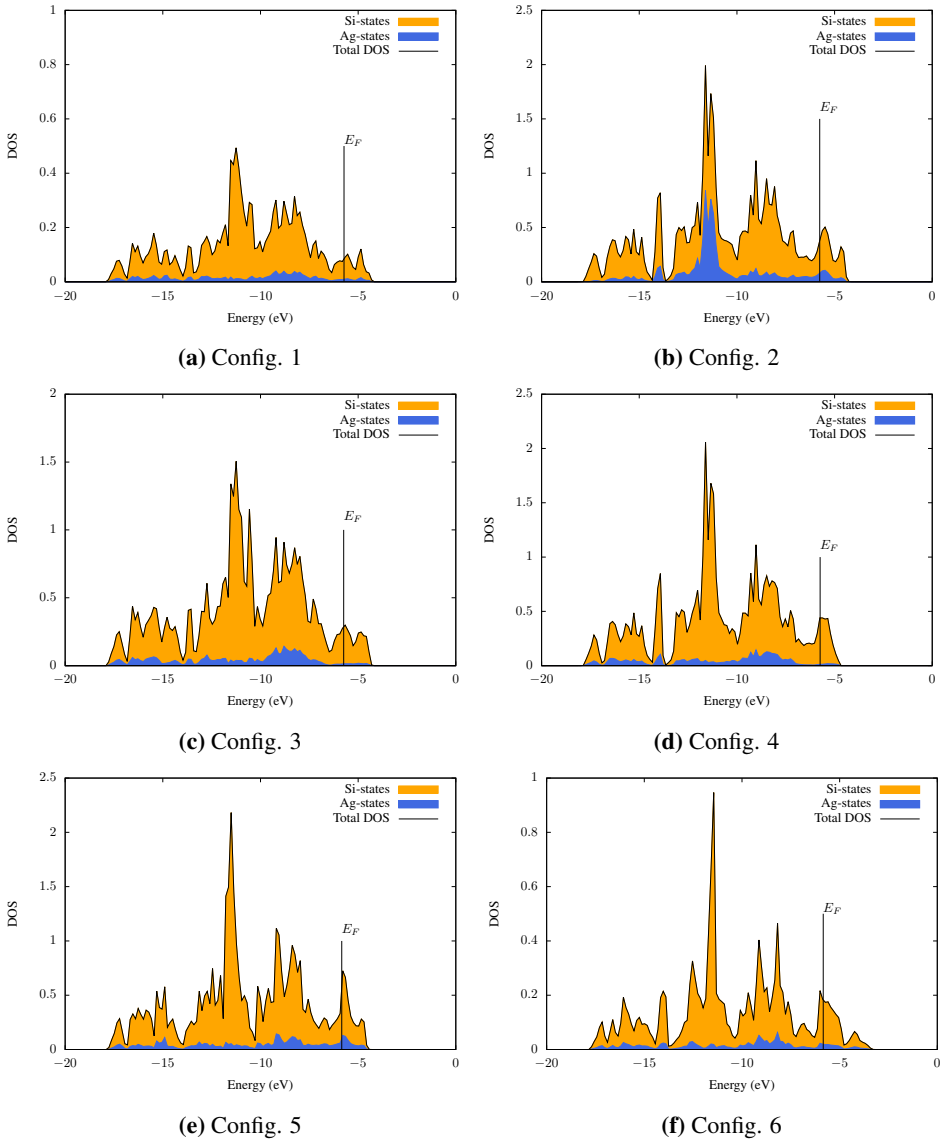
(e) Config. 5

(f) Config. 6

Figure 4.23: DOS as a function of energy for Ag-doped Si with a doping concentration of 12.5% using different unit cell configurations with the standard setup.
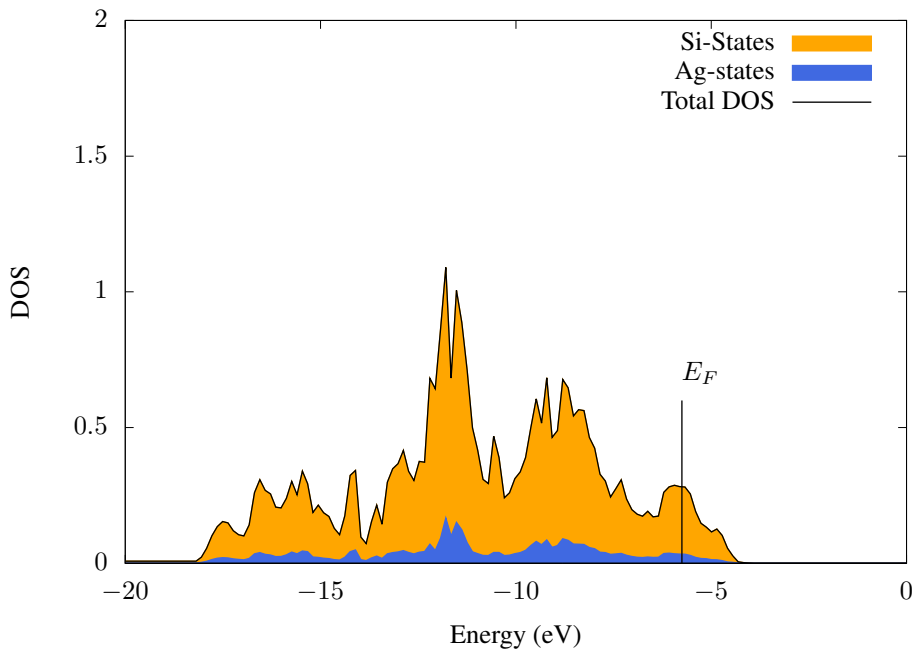
Figure 4.24: Boltzmann weighted DOS as a function of energy for Ag-doped Si with a doping concentration of 12.5%. Standard setup.

4.2.3 DFTB calculations

In this subsection we present the results for unit cells containing more than 16 atoms, using DFTB to optimize the geometry, then doing a DFT calculation on the final geometry to find the DOS and the Fermi level.

In Figure 4.25 we see the initial and final configurations of a unit cell of 32 atoms, where one Si atom is replaced with an Ag atom. The geometry is only slightly changed, there is a slightly longer distance to the nearest neighbors in the lattice from the Ag atom. In Figure 4.26 we see the DOS and Fermi level of the final geometry. The Fermi level is $E_F = -5.7577$ eV, and we see that it is placed in a clear drop in the DOS. Even though the DOS is lower around the Fermi level, it is nonzero, and the material is a metal. The partial DOS contribution from the Ag-states is small compared to the Si-states. For the larger systems, we will only include the total DOS, omitting the partial contributions.
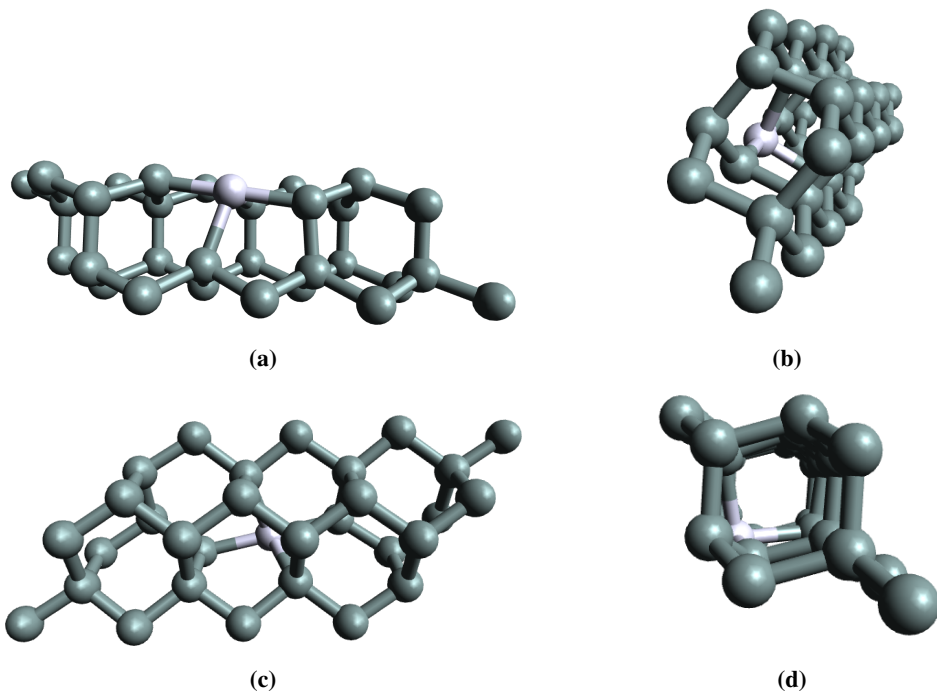

(a)

(b)

(c)

(d)
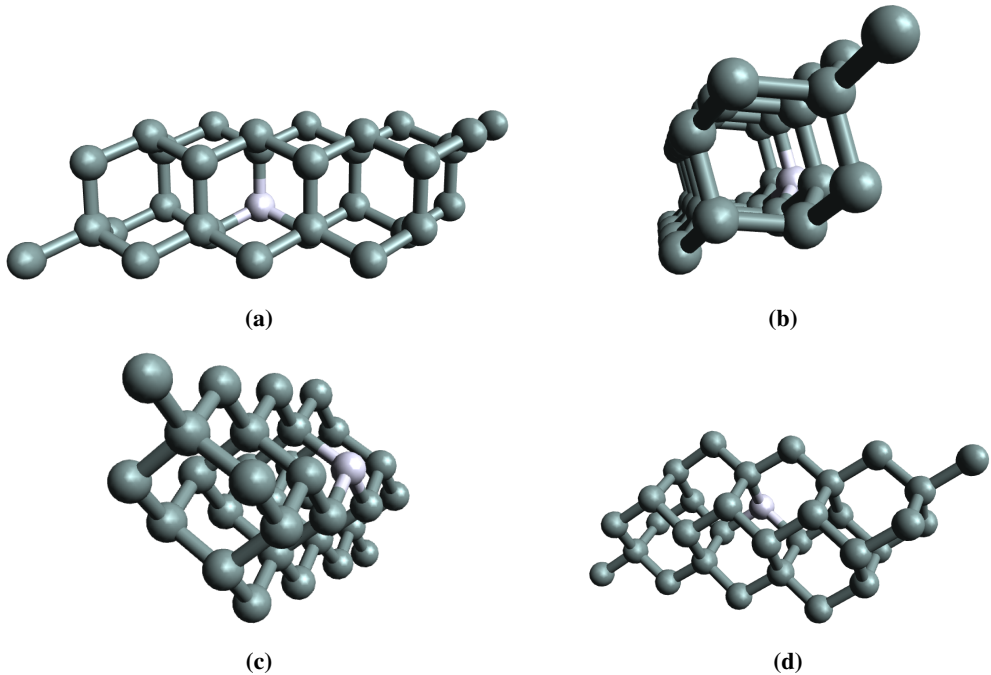
Figure 4.25: The unit cell of a 3.125% Ag-doped Si crystal. **(a)** and **(b)** are two perspectives of the initial configuration. **(c)** and **(d)** are two perspectives of the optimized geometry.
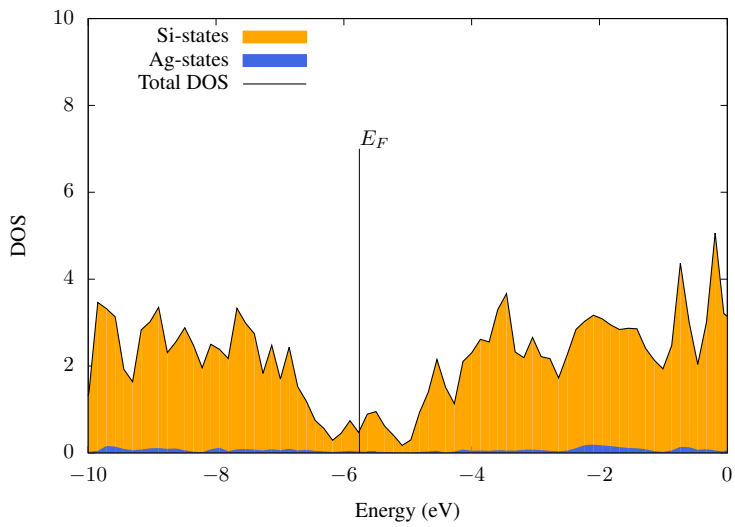
Figure 4.26: Boltzmann weighted DOS as a function of energy for Ag-doped Si with a doping concentration of 3.125%. Standard setup.

In the next calculations we have replaced 2 Si atoms with Ag in the 32-atomic basis, in three different ways. In the first configuration, Figure 4.27, the Ag atoms have initially one Si atom in between them, but after the geometry optimization, they have moved together, forming a cluster. In the second configuration, Figure 4.28, the Ag atoms are placed one lattice point further away from each other, and stay separated after the geometry optimization. We can see that the right-most Ag-atom in the final geometry has moved slightly out of its diamond lattice position, towards the other Ag atom. In the third configuration, Figure 4.29, the Ag atoms are placed even further away from each other, and stayed separated even after the geometry optimization. This indicates that there is some critical inter-atomic distance between the Ag-atoms determining if the two impurities will clump together or stay separated. When inspecting the DOS of the three configurations, Figure 4.30, we see that there are no interesting properties for our purposes in the search for an IB material, the Fermi levels all lie in an energy band.

(a)

(b)

(c)

(d)
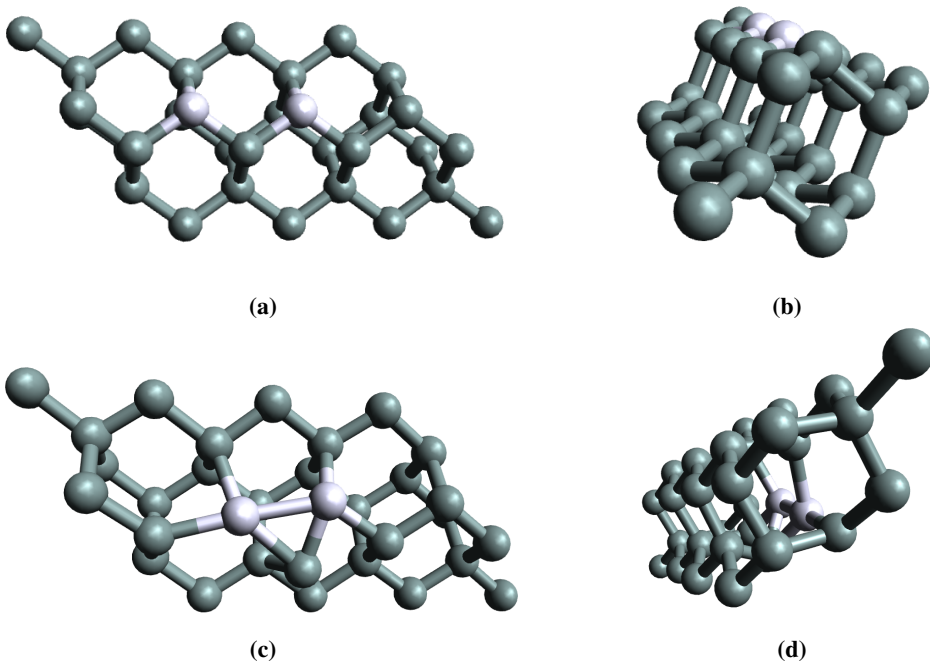
Figure 4.27: The unit cell of a 6.25% Ag-doped Si crystal. **(a)** and **(b)** are two perspectives of the initial configuration. **(c)** and **(d)** are two perspectives of the optimized geometry, labeled Config. 1.
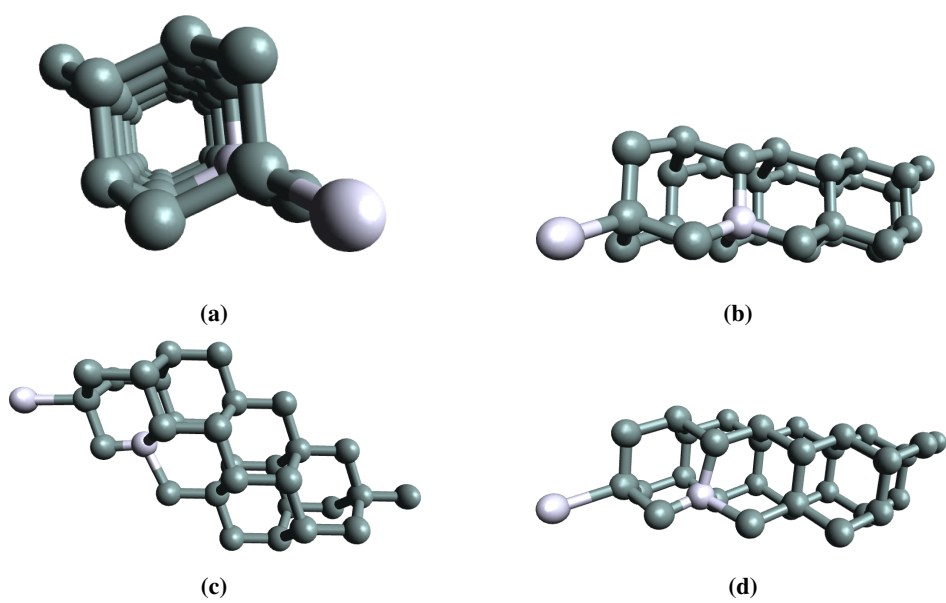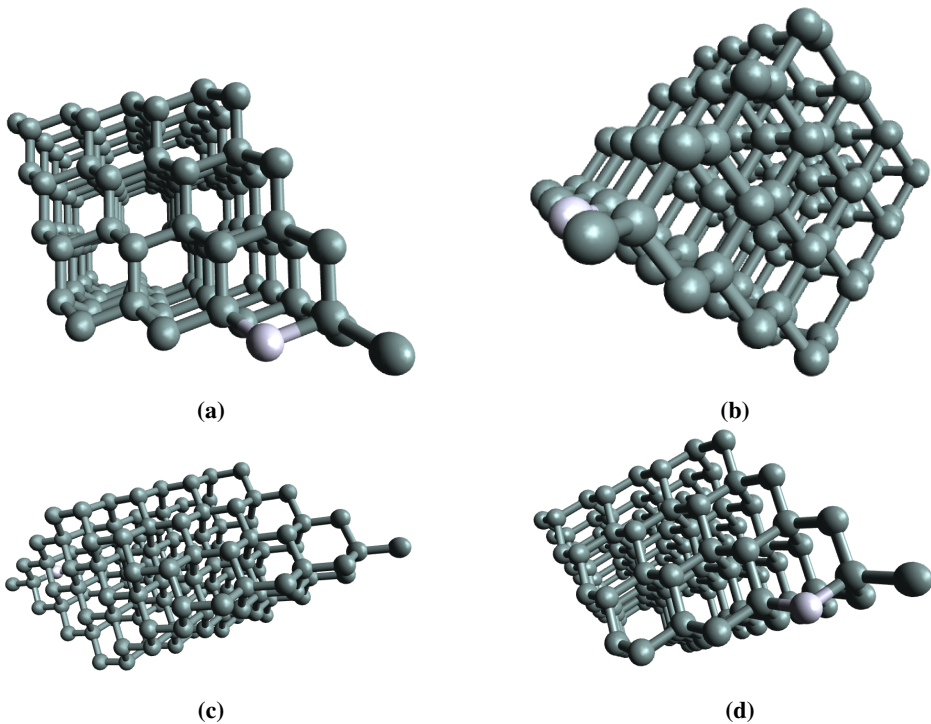
Figure 4.28: The unit cell of a 6.25% Ag-doped Si crystal. **(a)** and **(b)** are two perspectives of the initial configuration. **(c)** and **(d)** are two perspectives of the optimized geometry, labeled Config. 2.

(a)

(b)

(c)

(d)
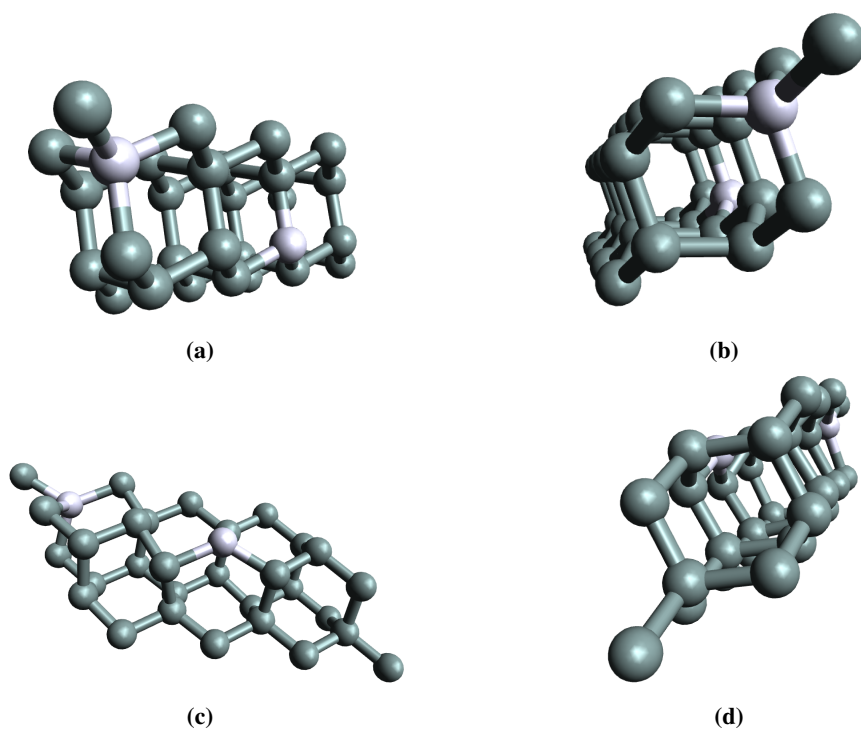
Figure 4.29: The unit cell of a 6.25% Ag-doped Si crystal. **(a)** and **(b)** are two perspectives of the initial configuration. **(c)** and **(d)** are two perspectives of the optimized geometry, labeled Config. 3.
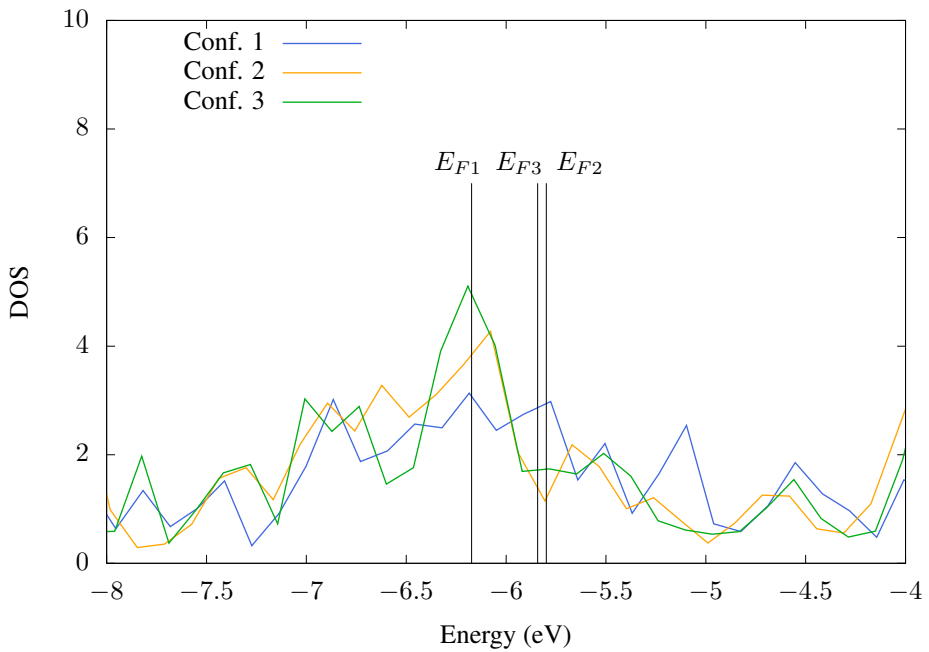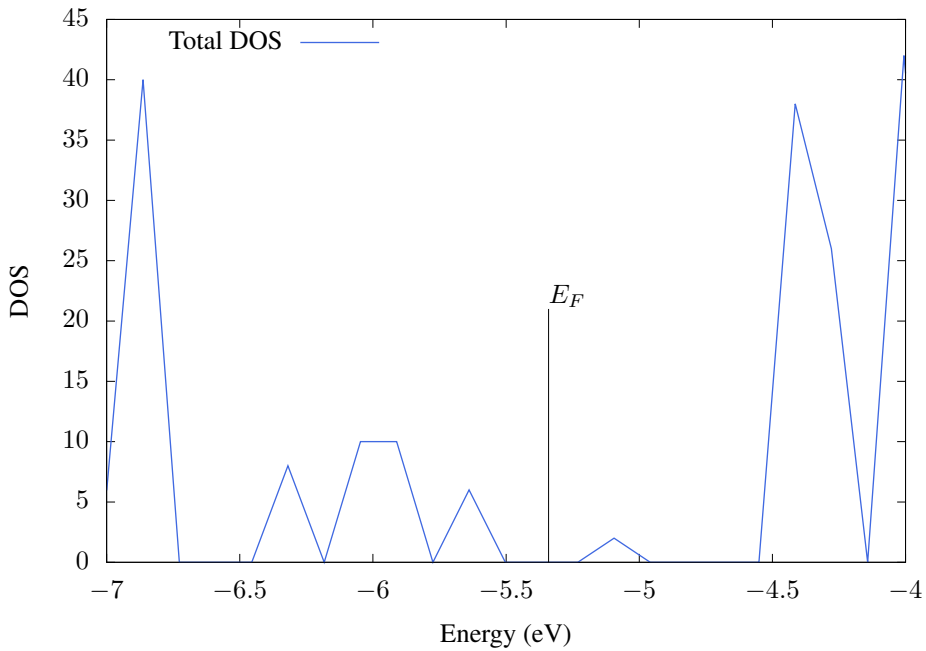
Figure 4.30: DOS as a function of energy for Ag-doped Si with a doping concentration of 6.25%. Standard setup.

We now see how vacancies in the lattice affect the electronic properties of the material. In addition to replacing one Si-atom with an Ag-atom in a 32-atomic unit cell, we also remove a Si-atom without replacing it with anything. This is done to visualize realistic effects when manufacturing the material. When doping a perfect Si crystal by "shooting" impurities at it, the impurities may carry such a momentum that they remove additional atoms in the lattice other than the ones they are replacing [51]. In Figure 4.31 the vacancy is right next to the Ag atom. In Figure 4.32 there are two Si-atoms between the vacancy and the Ag-atom, and in Figure 4.33 there are three Si-atoms between. The neighboring lattice points seem to move towards the vacancy in all the three optimized geometries, which makes sense from a classical point of view. The DOS for all the three configurations, shown in Figure 4.34, show that there are no interesting properties in the search for an IB material, the material is a metal.

(a)

(b)

(c)

(d)

Figure 4.31: The unit cell of a 3.23% Ag-doped Si crystal with a vacancy in the lattice. **(a)** and **(b)** are two perspectives of the initial configuration. **(c)** and **(d)** are two perspectives of the optimized geometry, labeled Config. 1.
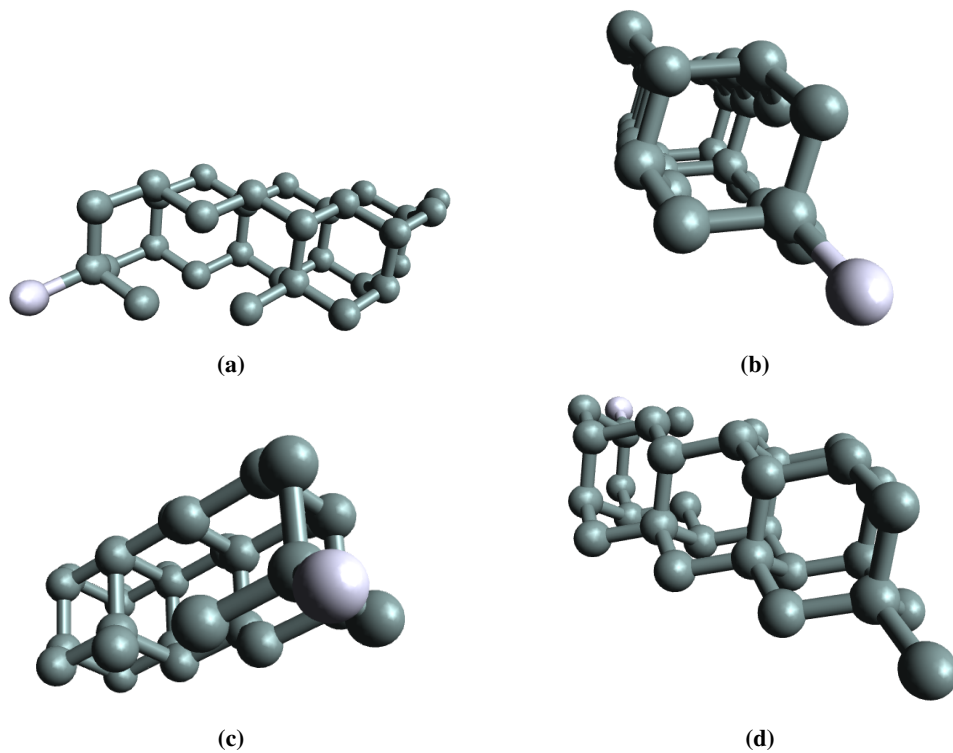
Figure 4.32: The unit cell of a 3.23% Ag-doped Si crystal with a vacancy in the lattice. **(a)** and **(b)** are two perspectives of the initial configuration. **(c)** and **(d)** are two perspectives of the optimized geometry, labeled Config. 2.
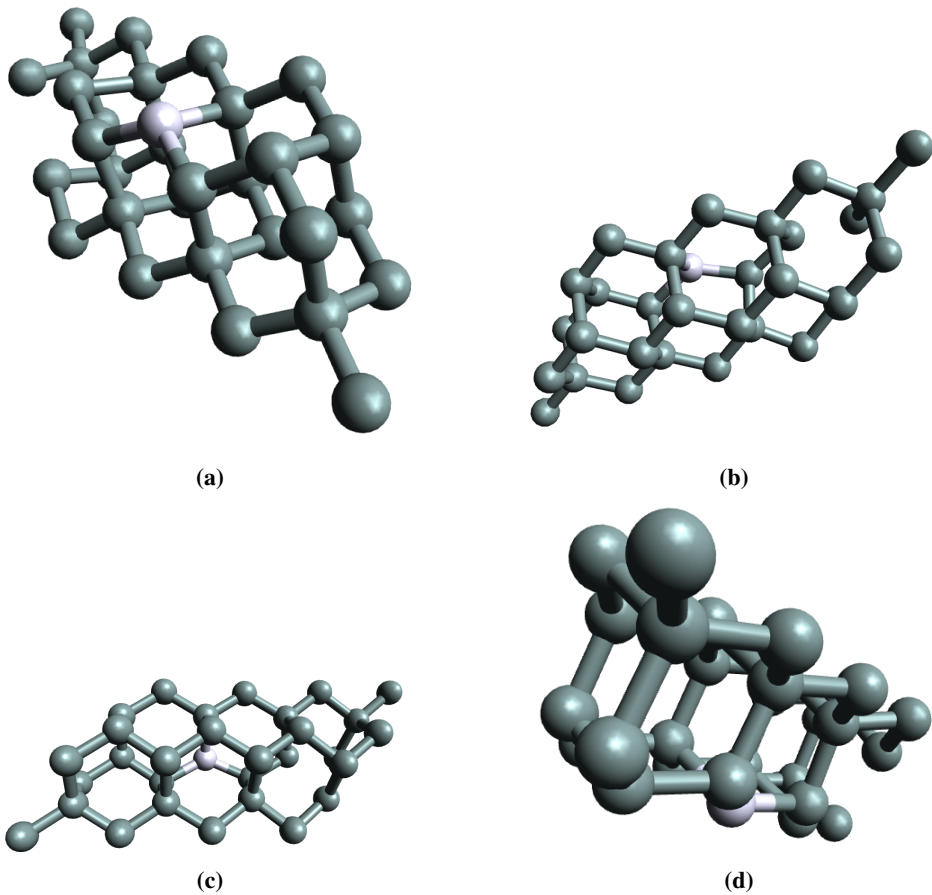
Figure 4.33: The unit cell of a 3.23% Ag-doped Si crystal with a vacancy in the lattice. **(a)** and **(b)** are two perspectives of the initial configuration. **(c)** and **(d)** are two perspectives of the optimized geometry, labeled Config. 3.
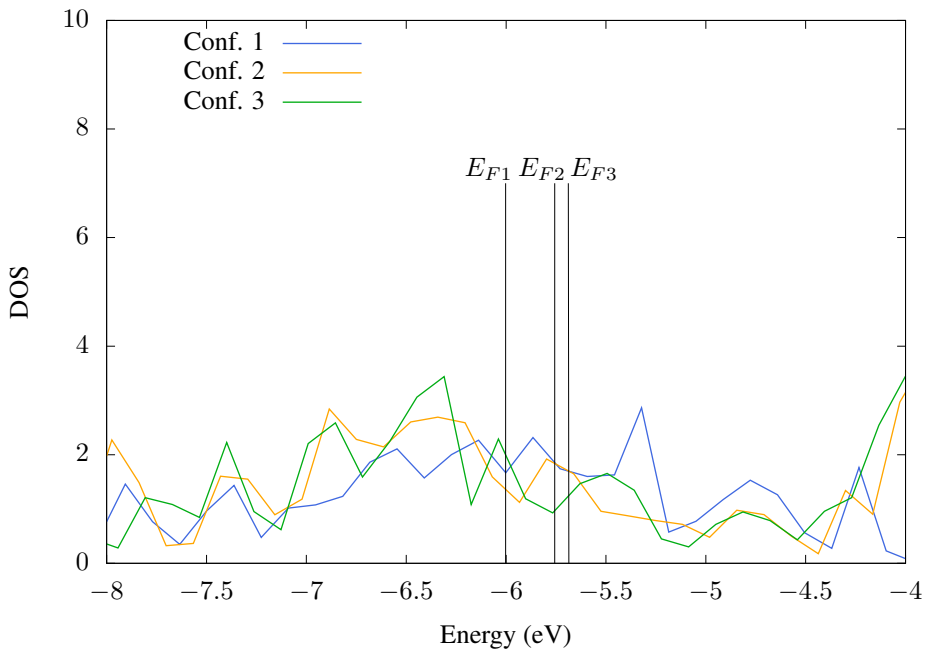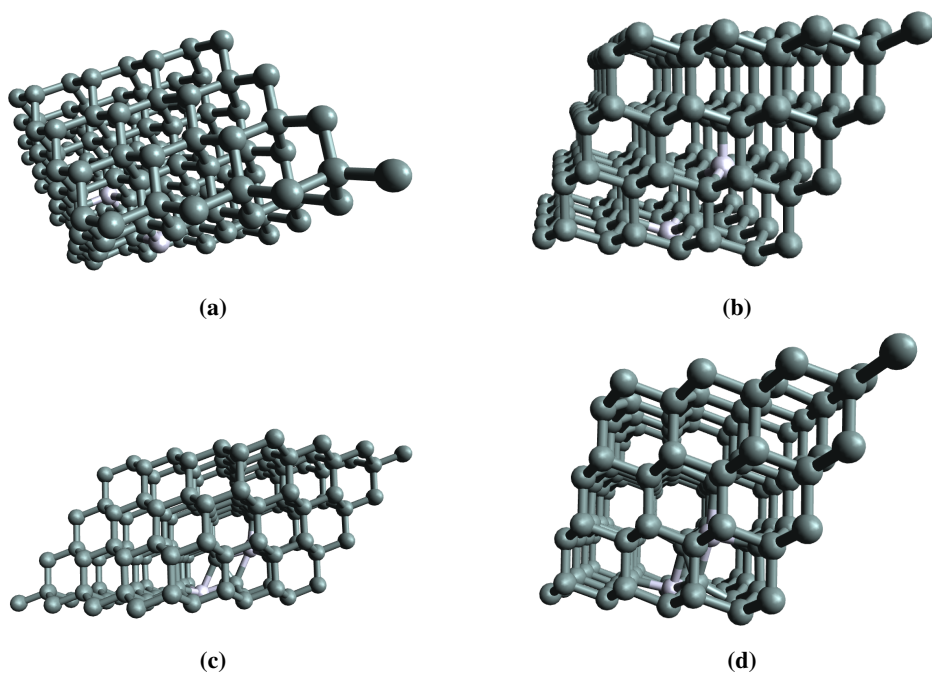
Figure 4.34: DOS as a function of energy for Ag-doped Si with a doping concentration of 3.23% with a defect in the lattice. Standard setup.

We now use a 128-atomic unit cell with one Si-atom replaced with an Ag-atom. The initial and optimized unit cell are shown in Figure 4.35. It seems that only the immediate surrounding of the impurity is slightly shifted, while the lattice seems unaffected a couple of lattice sites away from the impurity, meaning that the majority of the lattice with a small doping concentration will still be in the diamond lattice, preserving some of the properties of pure Si. The numerical quality of the DOS-plot in Figure 4.36 seems poorer than some of the previous calculations, however, this plot is zoomed in around the Fermi level, which is the region we are most interested in. From the DOS in Figure 4.36 the material is a semiconductor since the Fermi level lies inside a band gap, and the gap is small. It should be noted that in this zoomed perspective small numerical errors will change the behavior of the material, so we cannot say for certain if, for example, the nonzero value just below -5 eV really is a part of the conduction band, or should be zero. A higher sampling rate around -6 eV could also give better indications on whether the nonzero DOS around -6 eV is a continuous band, ranging from -6.6 eV to -5.5 eV, or three separate bands. BAND does not allow to choose certain energy-regions to sample with a higher frequency, so the entire standard energy spectrum would need to be sampled at a higher rate if one wants a higher quality, increasing the computational time too much for the scope of this thesis. However this material is of interest since there may be indications of the IB at around -6.5 eV to -5.5 eV.
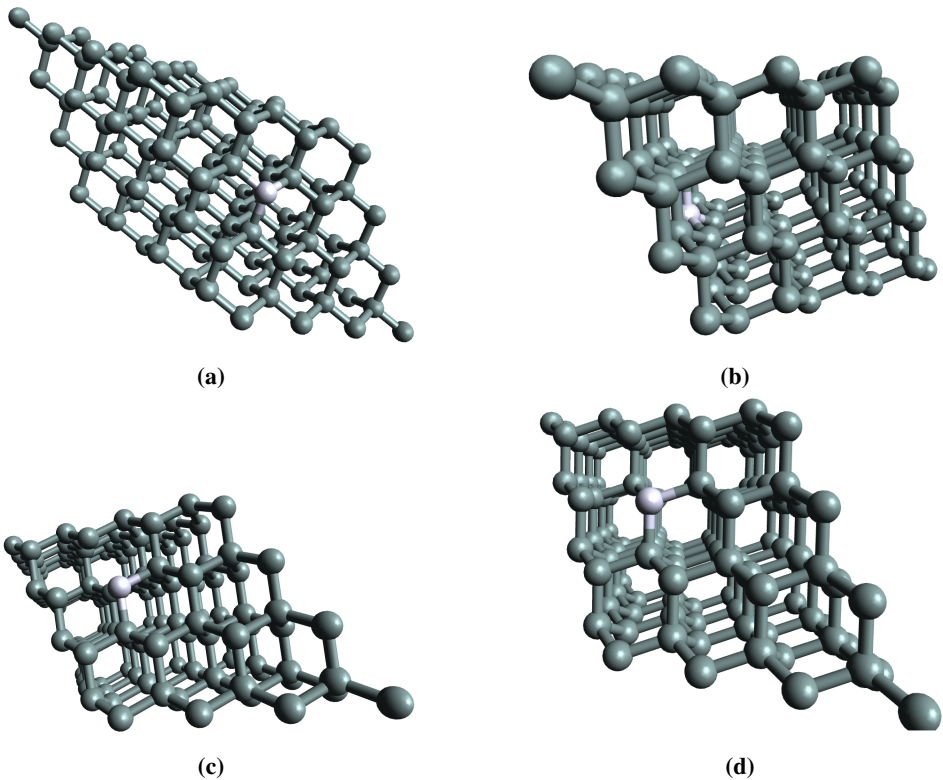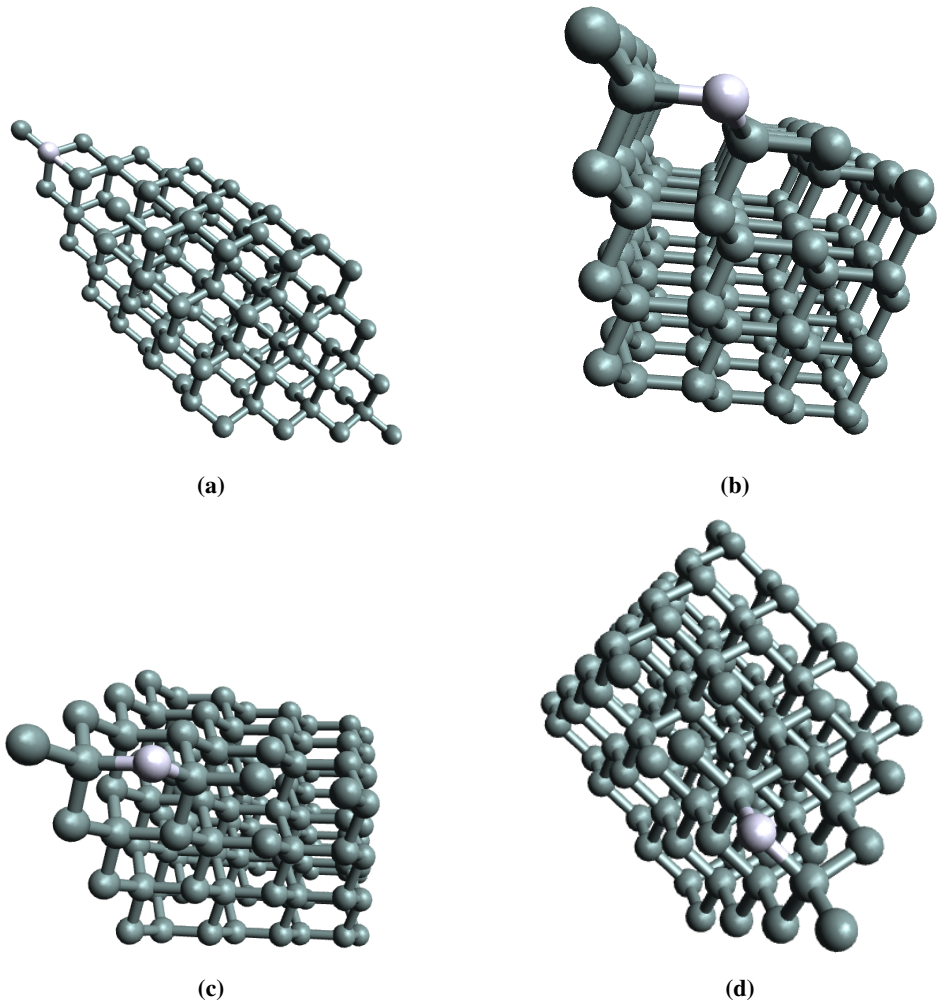

(a)

(b)

(c)

(d)

Figure 4.35: The unit cell of a 0.78% Ag-doped Si crystal. **(a)** and **(b)** are two perspectives of the initial configuration. **(c)** and **(d)** are two perspectives of the optimized geometry.

Figure 4.36: DOS as a function of energy for Ag-doped Si with a doping concentration of 0.78%. Standard setup.

We now add two Ag-atoms in the lattice, in two different unit cell configurations. In Figure 4.37 we see the configuration where the two Ag-atoms are placed as neighbors in the lattice. They have moved slightly towards each other in the optimized geometry. In Figure 4.38 the Ag-atoms are placed such that it is 2 lattice sites away. Looking at the DOS in Figure 4.39 we see that there might be some trends for a formation of an intermediate band in both the configurations. However, both the Fermi levels lie inside a nonzero region of states and the materials are both metals.
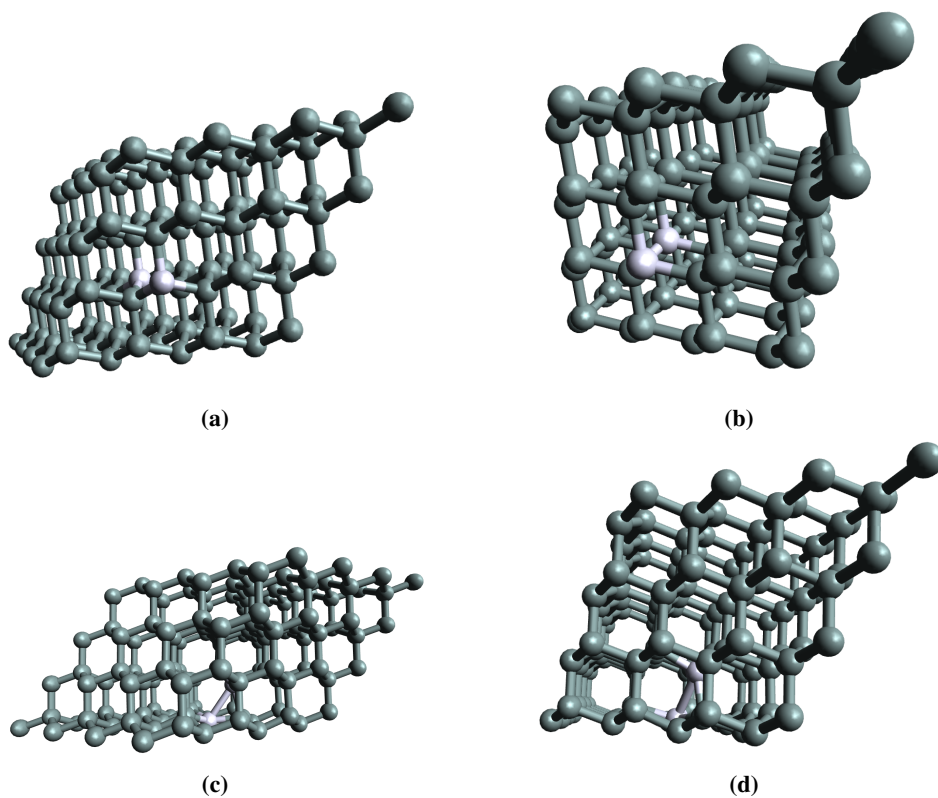
Figure 4.37: The unit cell of a 1.56% Ag-doped Si crystal. **(a)** and **(b)** are two perspectives of the initial configuration. **(c)** and **(d)** are two perspectives of the optimized geometry, labeled Config. 1.

Figure 4.38: The unit cell of a 1.56% Ag-doped Si crystal. **(a)** and **(b)** are two perspectives of the initial configuration. **(c)** and **(d)** are two perspectives of the optimized geometry, labeled Config. 2.
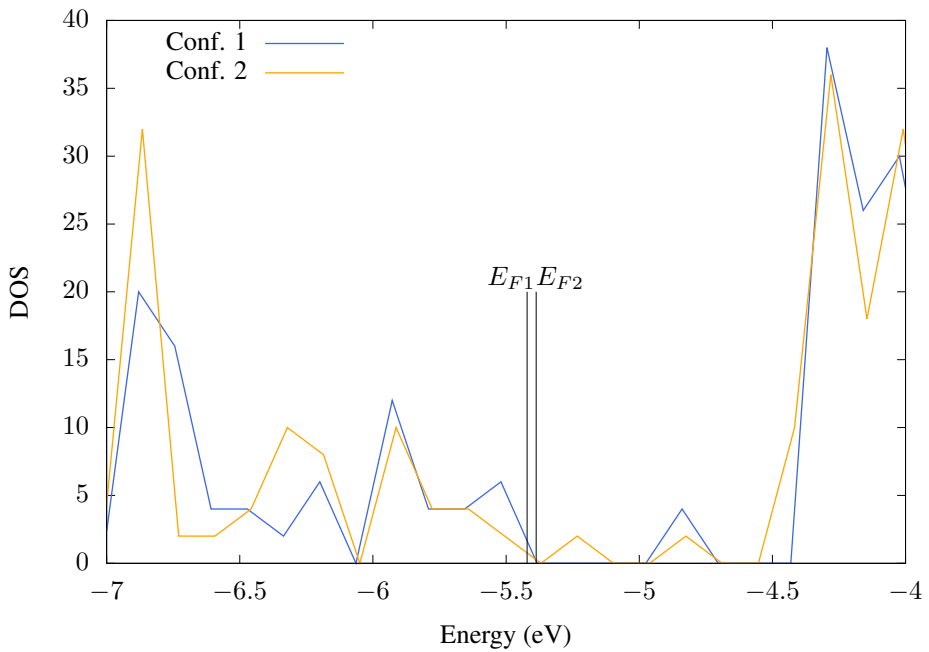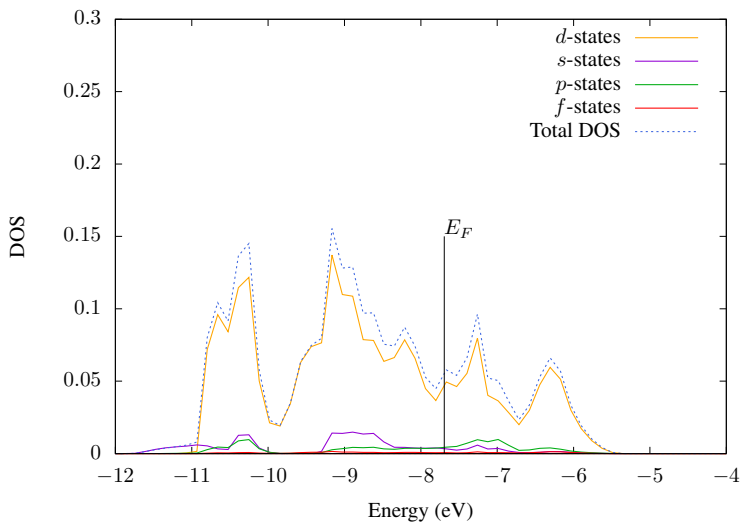
Figure 4.39: DOS as a function of energy for Ag-doped Si with a doping concentration of 1.56%. Standard setup.

We will now see the effects of vacancies in the lattice with a 128 atomic basis, where one Si-atom is replaced by one Ag-atom, and one Si-atom is removed from the lattice. In Figure 4.40 the vacancy is right next to the Ag-atom, and in Figure 4.41 there are two Si atoms in between the vacancy and the Ag-impurity. Again, the atoms in the immediate surrounding of the vacancy have moved towards the vacancy in the optimized geometry, slightly. The DOS for these two configurations are shown in Figure 4.42, and also here we see that there are tendencies for the material to carry IB properties. From the DOS of Config. 1 we see that the Fermi level may lie inside what looks like an IB. From the DOS of Config. 2 wee see that the Fermi level lies inside a region which may resemble an IB, however, due to the numerical quality wee cannot say anything for certain and the system should be studied further. Both the materials seem to have the CB edge at about -4.3 eV, and the VB edge at about -6.3 eV, meaning that the band gap is about $E_g = 2$ eV.

(a)

(b)

(c)

(d)

Figure 4.40: The unit cell of a 1.56% Ag-doped Si crystal with a vacancy in the lattice. **(a)** and **(b)** are two perspectives of the initial configuration. **(c)** and **(d)** are two perspectives of the optimized geometry, labeled Config. 1.

Figure 4.41: The unit cell of a 1.56% Ag-doped Si crystal with a vacancy in the lattice. **(a)** and **(b)** are two perspectives of the initial configuration. **(c)** and **(d)** are two perspectives of the optimized geometry, labeled Config. 2.
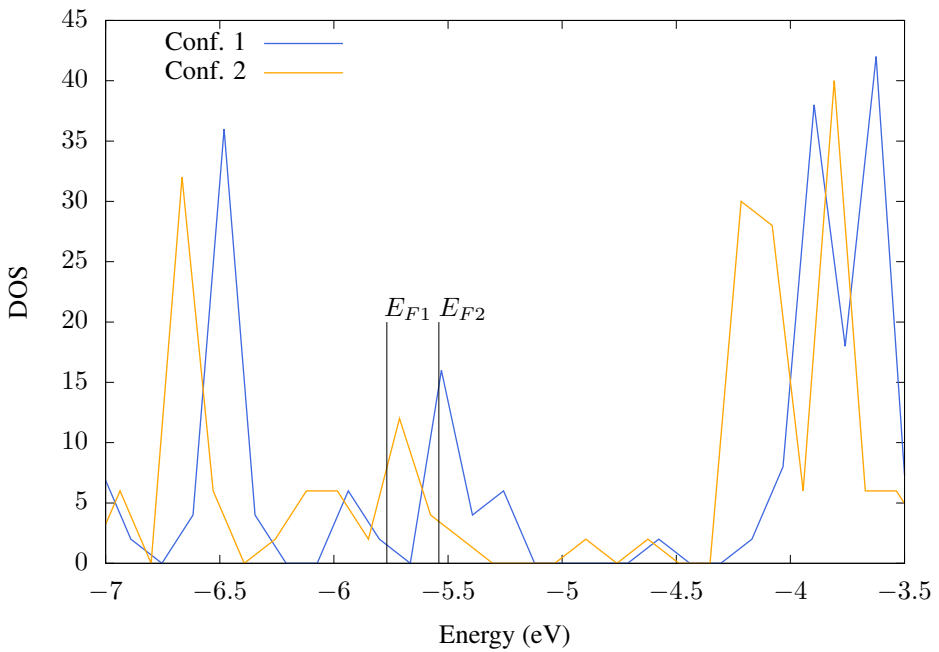
Figure 4.42: DOS as a function of energy for Ag-doped Si with a doping concentration of 0.79% with a vacancy in the lattice. Standard setup.

4.3 W-doped Si

In this section we present results from systems doped with W. For the unit cell sizes ranging from 4 to 16, we are using the BAND program to run DFT calculations. For larger systems, optimizing the geometry using DFT is too computationally demanding. Since there are currently no DFTB-parameter sets for W-Si, we are instead using a program package MOPAC, which is a semi-empirical method, to optimize the geometry. A DFT calculation is then run on the optimized geometry to find the densities of states and the Fermi levels.

4.3.1 Properties of W

In Figure 4.43 we see the DOS of W in the diamond lattice with the same lattice parameter as Si. The whole energy band consists primarily of d-states and two peaks are apparent at about -9 eV and -10 eV to -11 eV. The total band is rather narrow compared to that of Si which is about three times as big on the energy scale.

Figure 4.43: DOS as a function of energy for pure W in the cubic diamond lattice using the PW91 functional. The lattice parameter is set to the experimental value of Si in the diamond lattice. Small frozen core. Basis type TZ2P. The Fermi level is $E_F = -7.6928$ eV.

W naturally forms in the body centered cubic (BCC) lattice, and a calculation on W in this lattice is shown in Figure 4.44. The lattice parameter is set to the experimental value of $a = 3.17$ Å, as given by [52]. From the DFT calculation the material is a metal, which is its actual physical property, partly validating the DFT method.
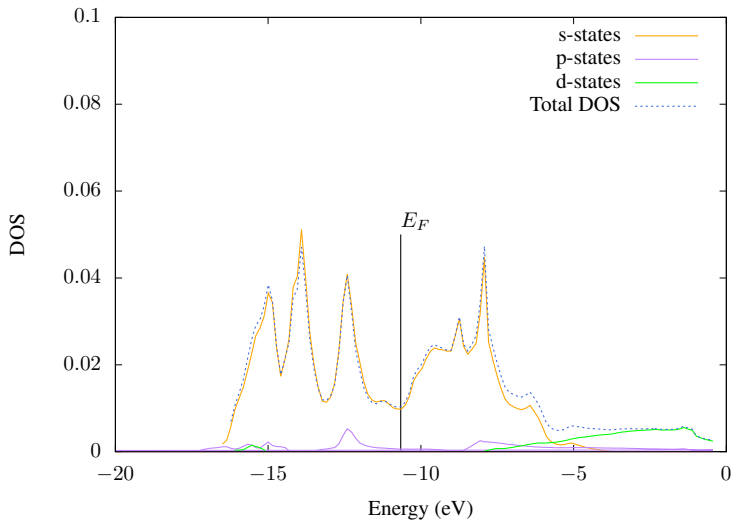
Figure 4.44: DOS as a function of energy for pure W in the BCC lattice using the PW91 functional. The lattice parameter is set to the experimental value of W in the BCC. Standard setup. The Fermi level is $E_F = -10.6574$ eV.

4.3.2 DFT calculations

DFT calculations were run on an 8-atomic basis, with two W-atoms and 6-Si atoms in the diamond lattice. Using 8 different configurations, shown in Figure 4.45, the DOS and Fermi levels were calculated, and the results shown in Figure 4.46 and Figure 4.47. Configuration 2 and 7, both corresponding to the same crystal lattice when the unit cell is repeated in space, give the same total DOS with some states giving an indication of an IB. However, the Fermi level lies about 10 eV away from this apparent band in energy space, and the materials are both metals. The rest of the configurations are all metals, with no other interesting properties in the context of an IBSC. From the degenerate configurations 2 and 7, we see that the partial DOS are distributed differently, while the total DOS is the same, again showing a weakness in the Mulliken population analysis. A "master DOS" is shown in Figure 4.48, where the DOS and the Fermi level is a superposition of all the 8 configurations, each weighted by its Boltzmann factor.
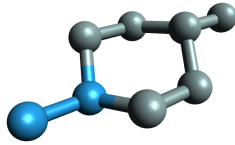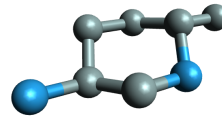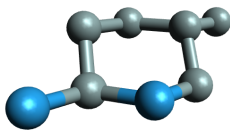
(a) Config. 1
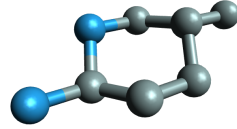
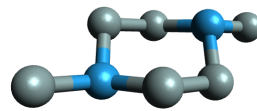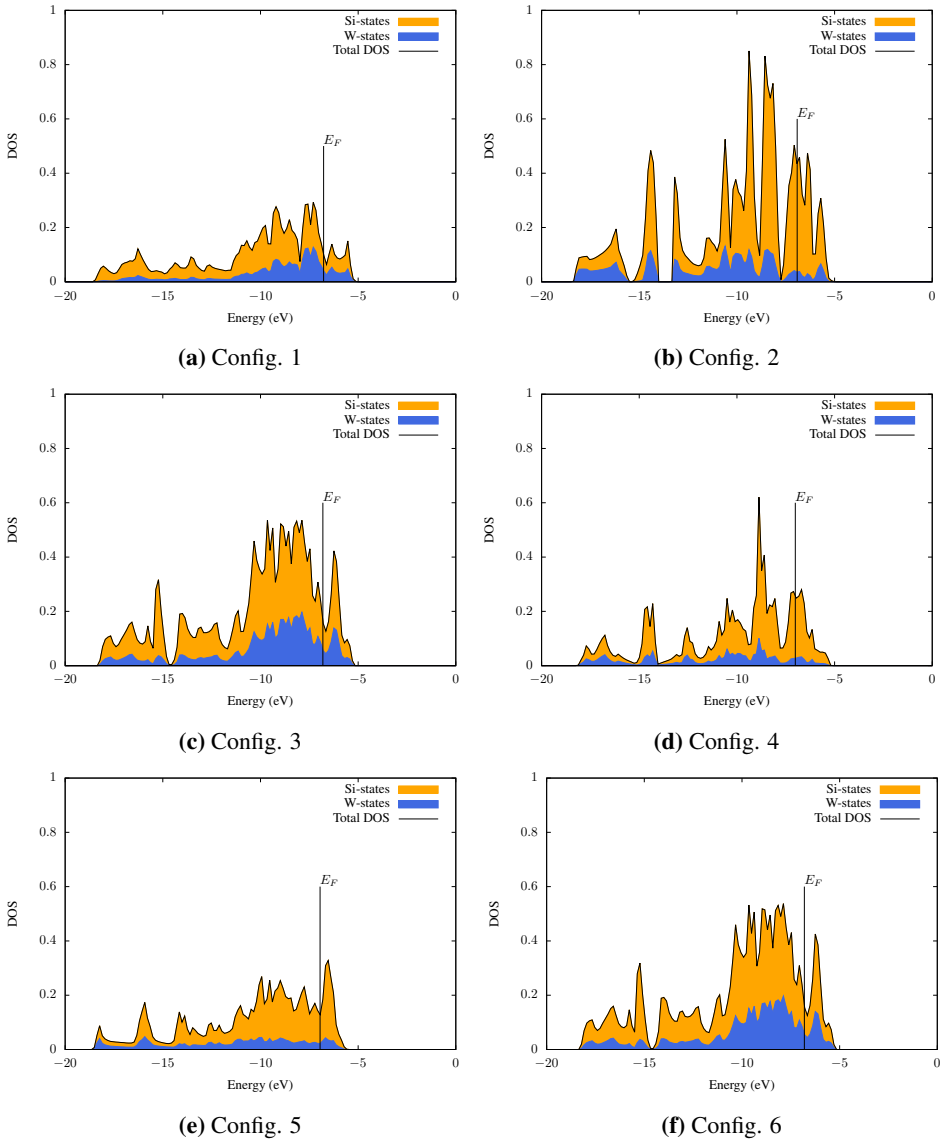(b) Config. 2
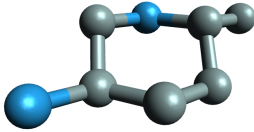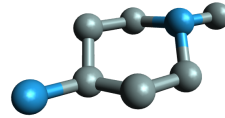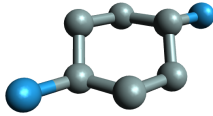
(c) Config. 3
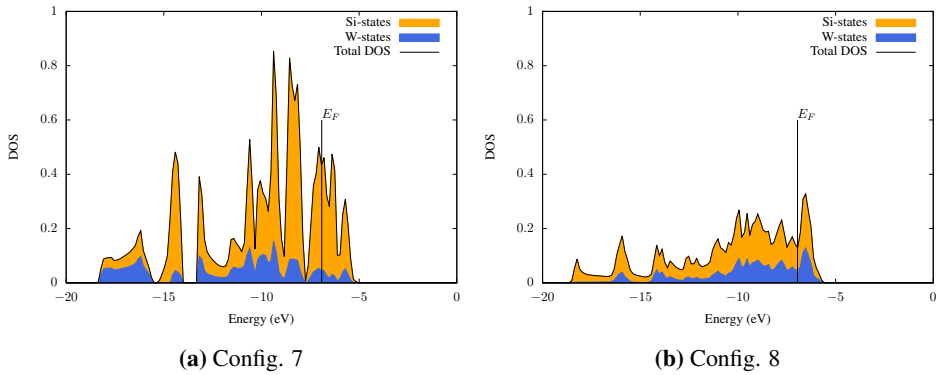

(d) Config. 4

(e) Config. 5

(f) Config. 6

(g) Config. 7

(h) Config. 8

Figure 4.45: Several unit cell configurations for W-doped Si with a doping concentration of 25%.

(a) Config. 1

(b) Config. 2

(c) Config. 3

(d) Config. 4

(e) Config. 5

(f) Config. 6

Figure 4.46: DOS as a function of energy for W-doped Si with a doping concentration of 25% using different unit cell configurations with the PW91 functional. Small frozen core. Basis type TZ2P.
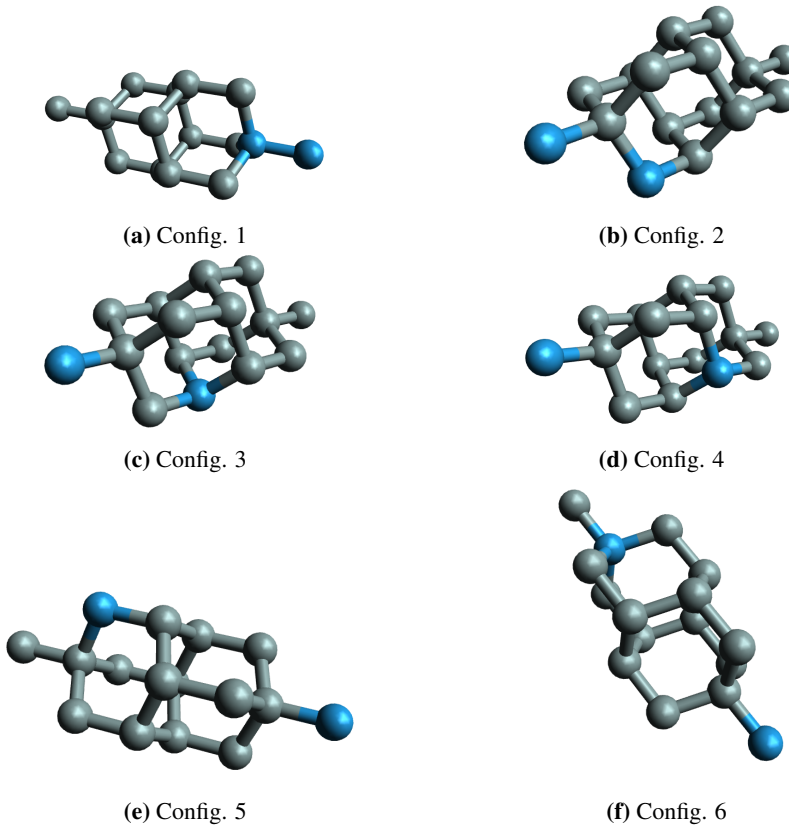
(a) Config. 7   **(b)** Config. 8

Figure 4.47: DOS as a function of energy for W-doped Si with a doping concentration of 25 % using different unit cell configurations with the PW91 functional. Small frozen core. Basis type TZ2P.
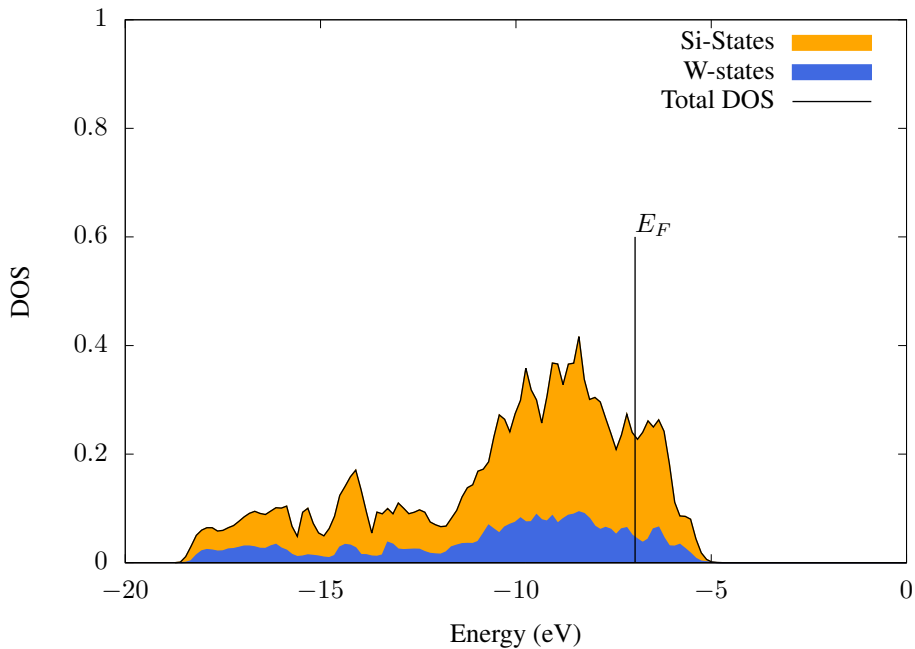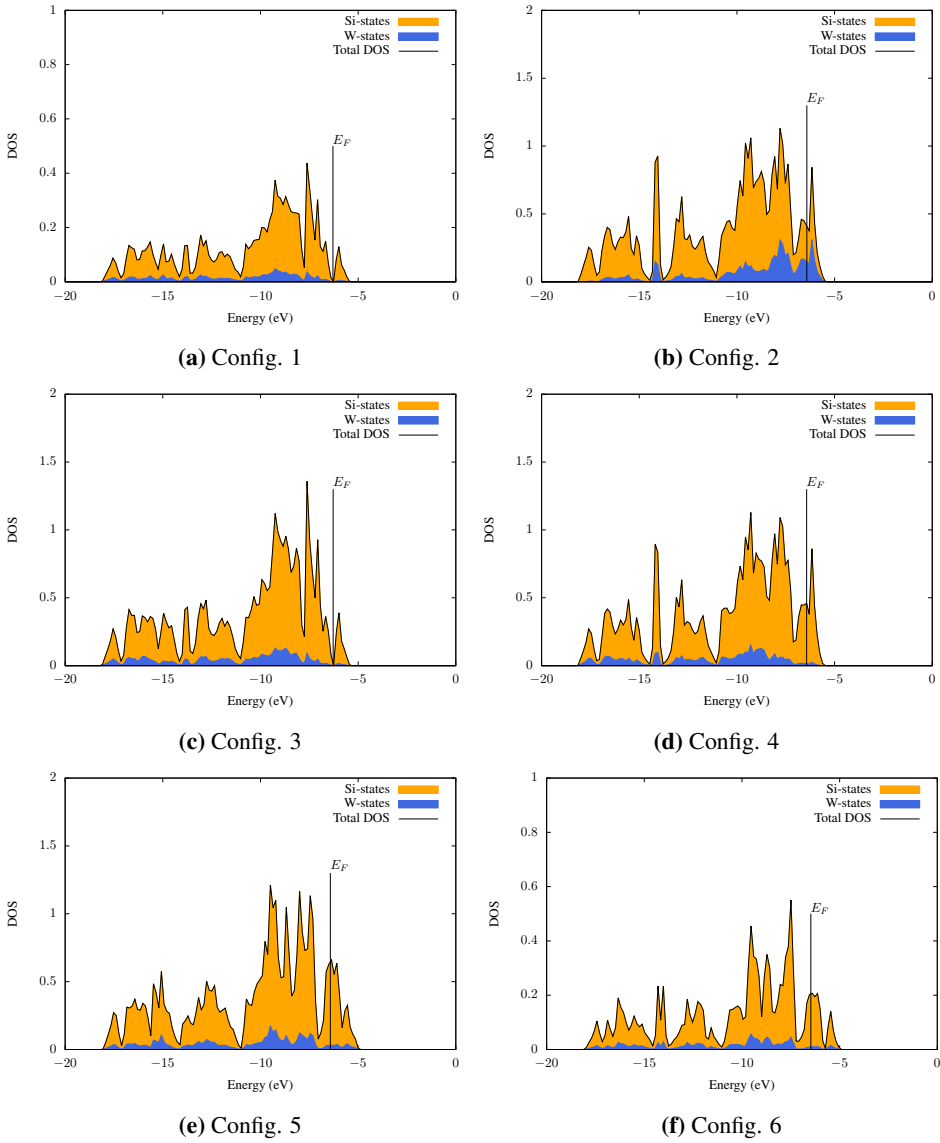

Figure 4.48: Boltzmann weighted DOS as a function of energy for W-doped Si with a doping concentration of 25% and a vacancy in the lattice. Standard setup.

We increase the unit cell size to include 16 atoms and do again DFT geometry optimizations. A total of 6 configurations were used with different placements of two W-atoms, these configurations are shown in Figure 4.49. The DOS is shown if Figure 4.50 and a "master DOS" in 4.51. Configuration 1 and 3 have the Fermi level in a narrow region where the DOS is zero. However, all the other configurations lack this region with zero DOS, and the master DOS does not possess this property, so if one wanted a material with a 12.5% doping, it would most certainly have metallic properties.

(a) Config. 1

(b) Config. 2

(c) Config. 3

(d) Config. 4

(e) Config. 5

(f) Config. 6

Figure 4.49: Several unit cell configurations for W-doped Si with a doping concentration of 12.5%.

(a) Config. 1

(b) Config. 2

(c) Config. 3
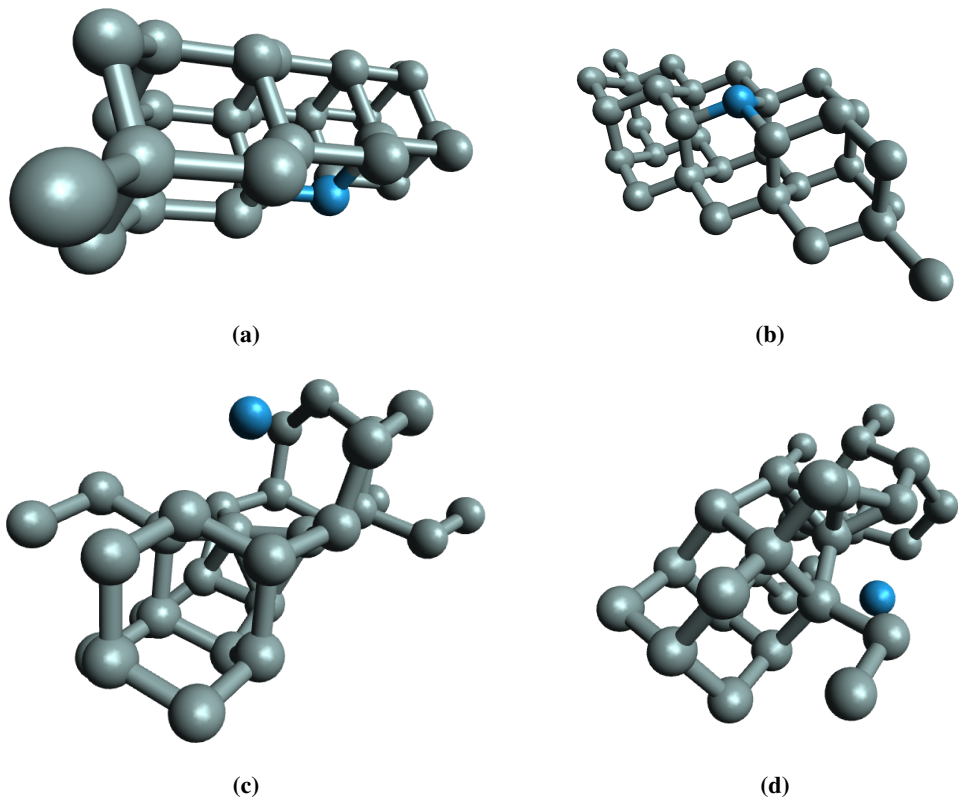
(d) Config. 4

(e) Config. 5

(f) Config. 6

Figure 4.50: DOS as a function of energy for W-doped Si with a doping concentration of 12.5% using different unit cell configurations with the standard setup.
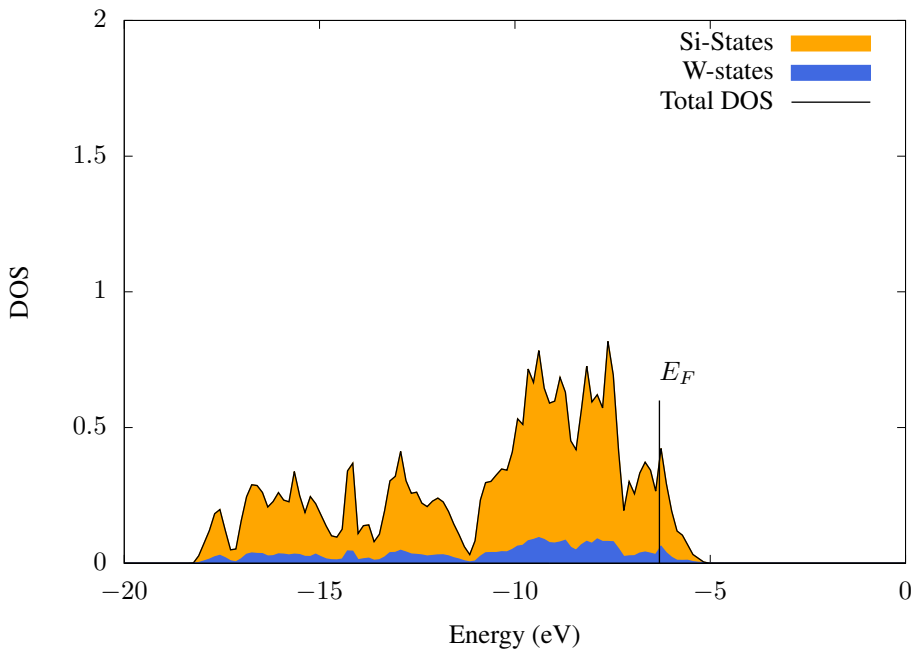
Figure 4.51: Boltzmann weighted DOS as a function of energy for W-doped Si with a doping concentration of 12.5%. Standard setup.

4.3.3 MOPAC and DFT calculations

We now look at larger systems, using MOPAC to optimize the geometry and BAND to do a DFT calculation on the optimized geometry. In Figure 4.52 we see the initial and optimized geometry for a 32-atomic unit cell where one Si-atom is replaced by a W-atom, giving a doping concentration of 3.125%. The unit cell is dramatically changed compared to the DFTB optimization run on the configurations including Ag. The DOS of this system is shown in Figure 4.53. There is a clear DOS-drop between -6 eV and -6.5 eV, however, it is nonzero, and the Fermi level lies inside band, indicating that the material is a metal.
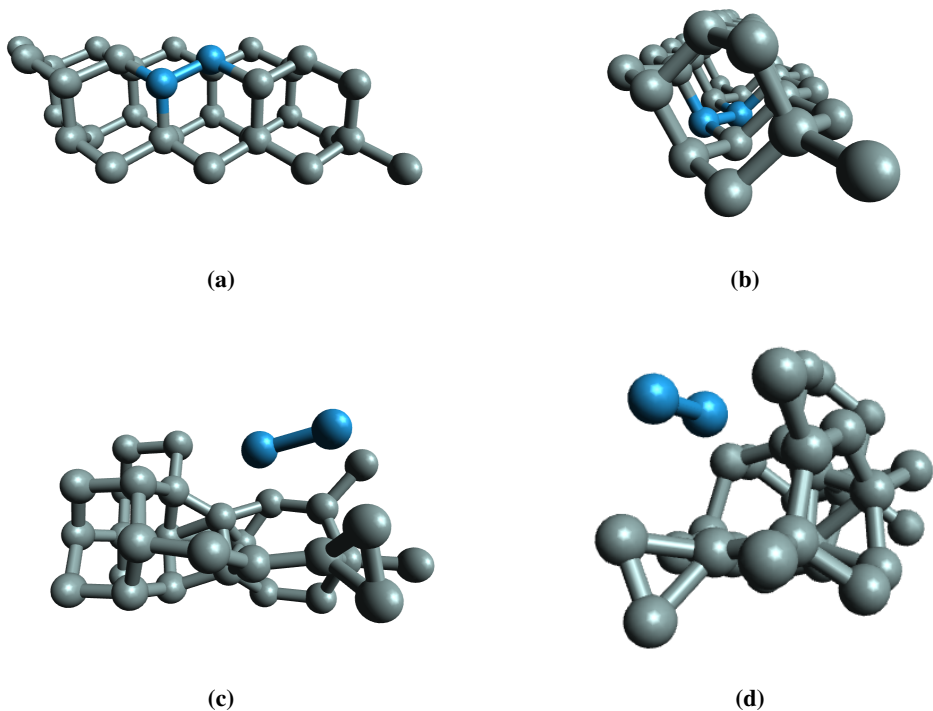

(a)

(b)

(c)

(d)

Figure 4.52: The unit cell of a 3.125% W-doped Si crystal. **(a)** and **(b)** are two perspectives of the initial configuration. **(c)** and **(d)** are two perspectives of the optimized geometry.
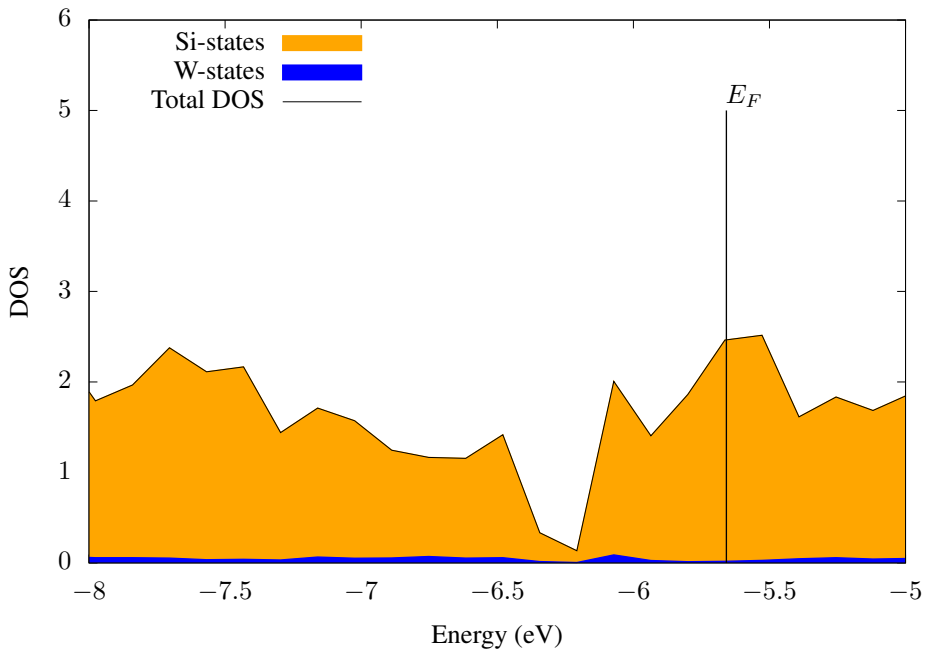
Figure 4.53: DOS of a 3.125% W-doped Si crystal. The Fermi level is $E_F = 5.682$ eV.

In Figure 4.57 we see the DOS for W-doped Si with a doping concentration of 6.25% for three different unit cell configurations. The three configurations started with different internal distance between the W-atoms, shown in Figure 4.54, Figure 4.55 and Figure 4.56. The Fermi level from the second and third configurations lie almost on top of each other. All the three materials are metals, and there are no signs of a band gap near the Fermi levels. All the three optimized unit cells are quite deformed and it is difficult to find remains of a periodicity within the unit cells. In Figure 4.54 the W-atoms are placed next to each other and in Figure 4.55 there is one Si-atom in between. In both these configurations the W-atoms have moved together, forming a cluster. In the third configuration, however, the W-atoms were placed even further apart, and stayed separated even after the geometry optimization. This indicates that there is some critical distance marking the difference between cluster formation and separated W-impurities.
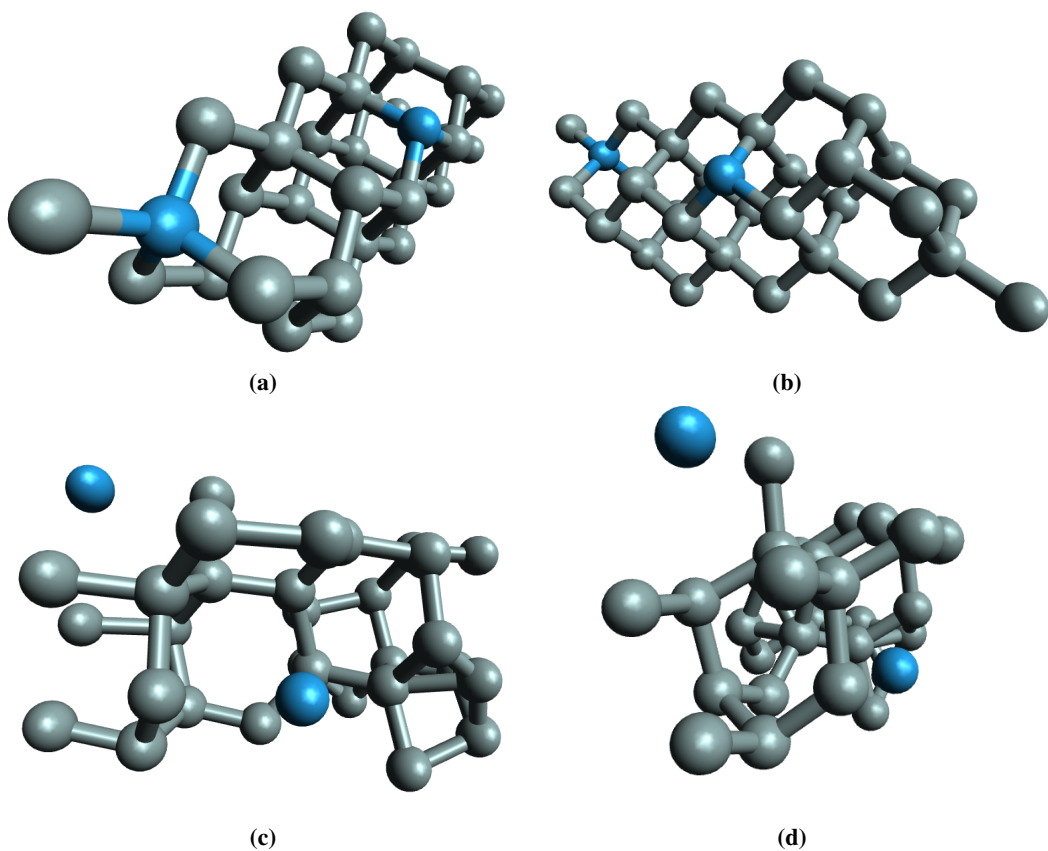

(a)

(b)

(c)

(d)

Figure 4.54: The unit cell of a 6.25% W-doped Si crystal. **(a)** and **(b)** are two perspectives of the initial configuration. **(c)** and **(d)** are two perspectives of the optimized geometry, labeled Config. 1.
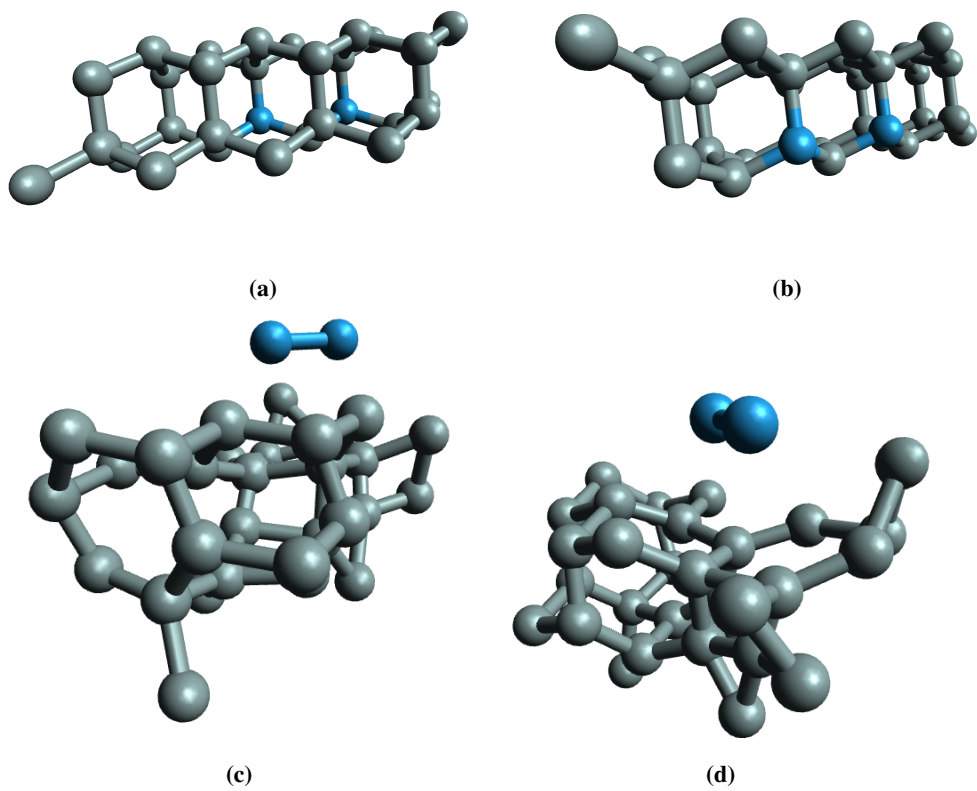
Figure 4.55: The unit cell of a 6.25% W-doped Si crystal. **(a)** and **(b)** are two perspectives of the initial configuration. **(c)** and **(d)** are two perspectives of the optimized geometry, labeled Config. 2.

Figure 4.56: The unit cell of a 6.25% W-doped Si crystal. (a) and (b) are two perspectives of the initial configuration. (c) and (d) are two perspectives of the optimized geometry, labeled Config. 3.
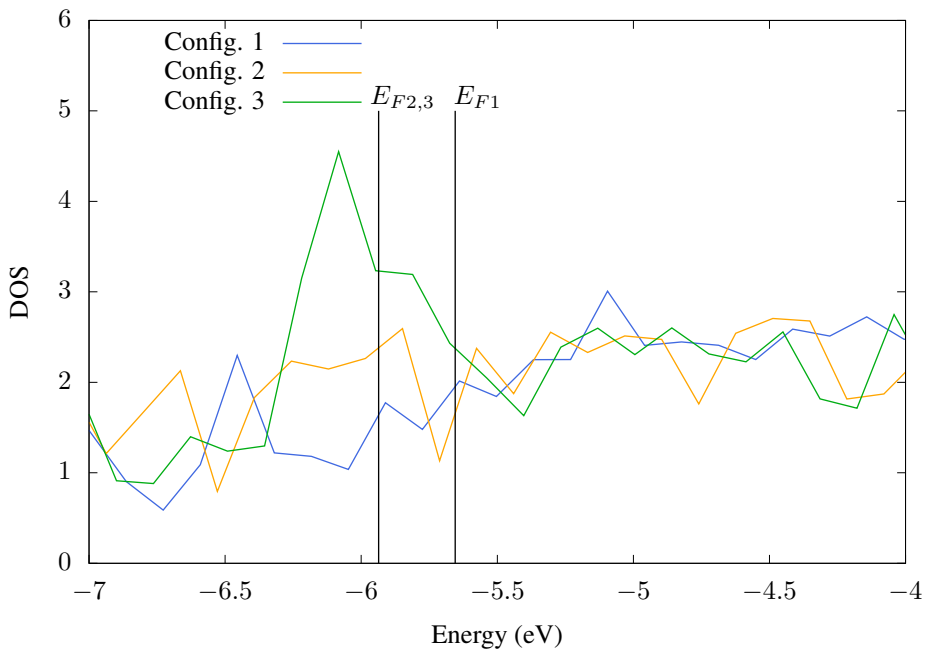
Figure 4.57: DOS as a function of energy for W-doped Si with a doping concentration of 6.25% . Standard setup.

In Figure 4.61 we see the DOS of the three configurations shown in Figure 4.58, Figure 4.59 and Figure 4.60. In these configurations, one Si-atom is replaced by a W-atom, and a Si-atom is removed without replacing it, leaving a vacancy in the lattice. All the Fermi levels lie inside an energy band, and the materials are all metals.


(a)

(b)

(c)

(d)
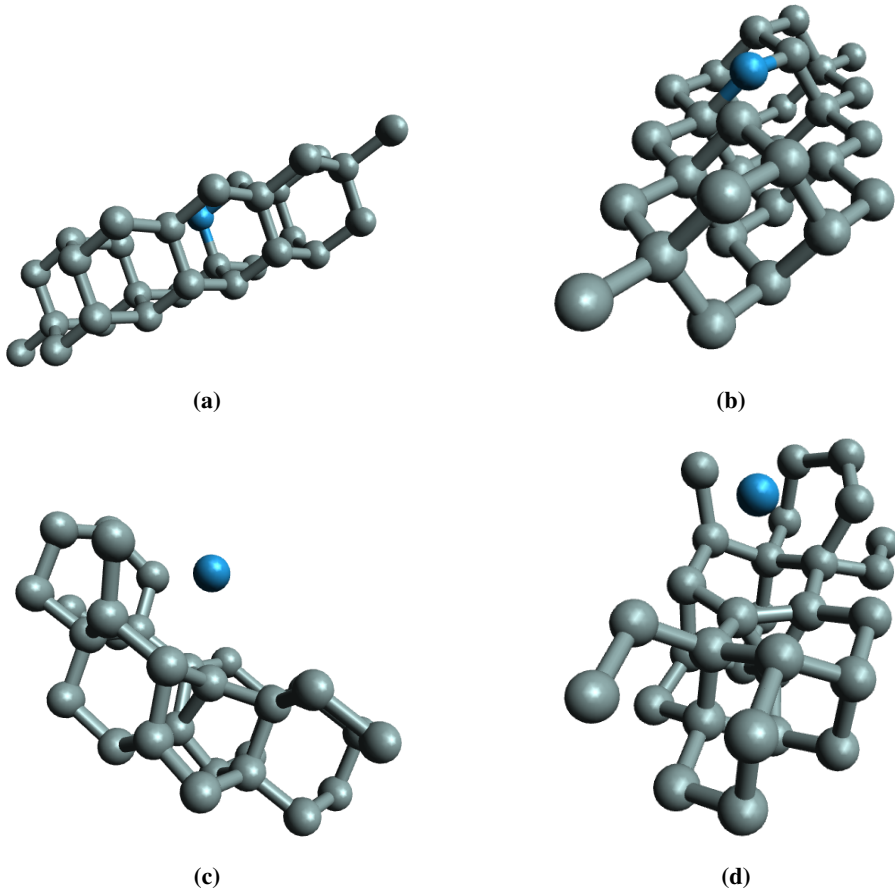
Figure 4.58: The unit cell of a 3.22% W-doped Si crystal. A Si atom is also removed right next to the W-impurity. **(a)** and **(b)** are two perspectives of the initial configuration. **(c)** and **(d)** are two perspectives of the optimized geometry, labeled Config. 1.
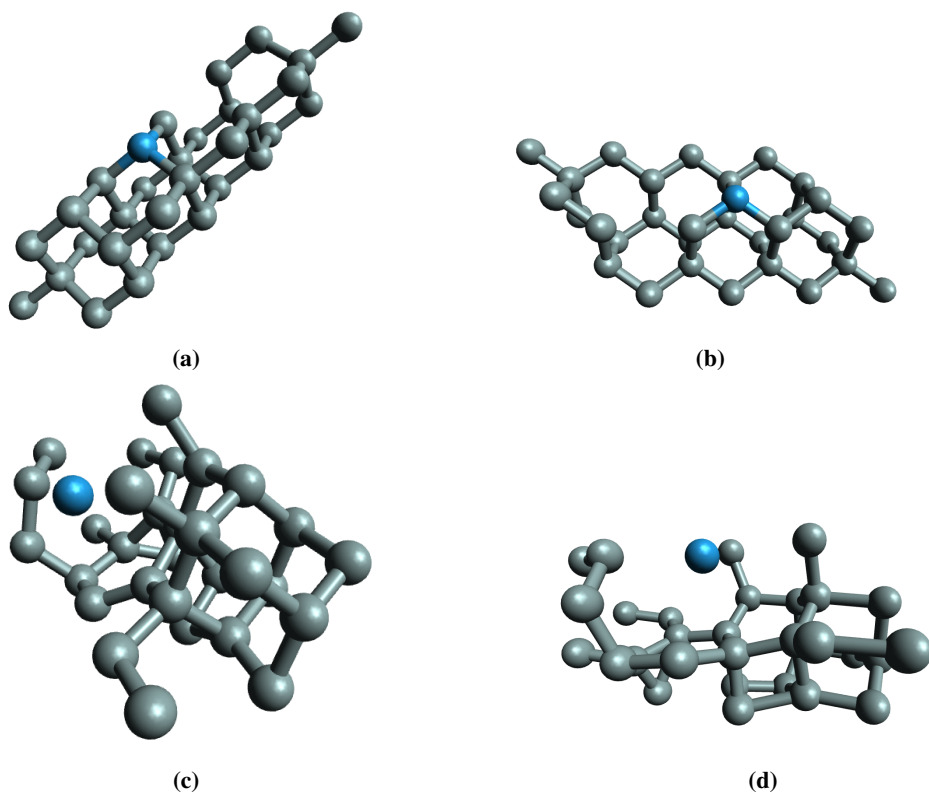
Figure 4.59: The unit cell of a 3.22% W-doped Si crystal. A Si atom is also removed from the lattice. **(a)** and **(b)** are two perspectives of the initial configuration. **(c)** and **(d)** are two perspectives of the optimized geometry, labeled Config. 2.
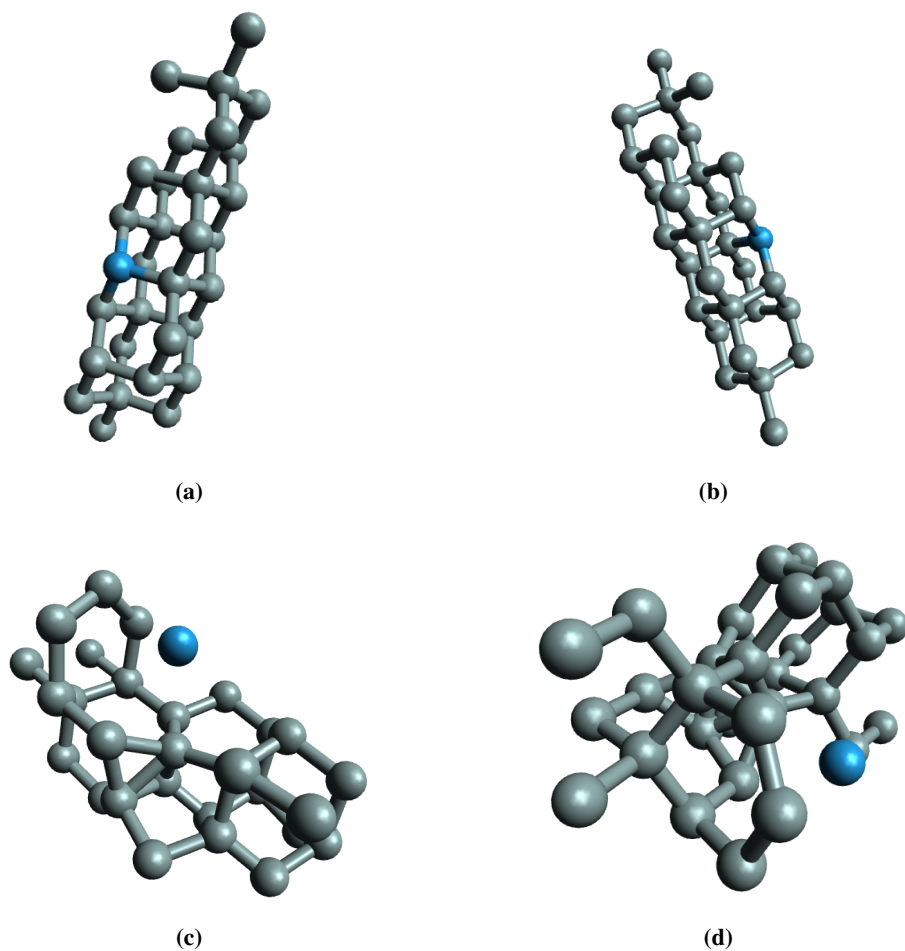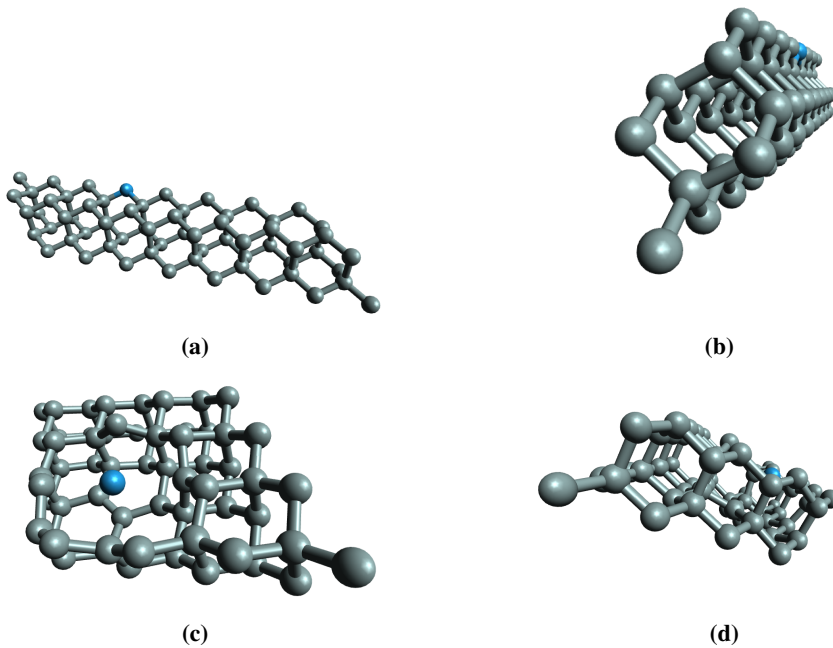
Figure 4.60: The unit cell of a 3.22% W-doped Si crystal. A Si atom is also removed from the lattice. **(a)** and **(b)** are two perspectives of the initial configuration. **(c)** and **(d)** are two perspectives of the optimized geometry, labeled Config. 3.
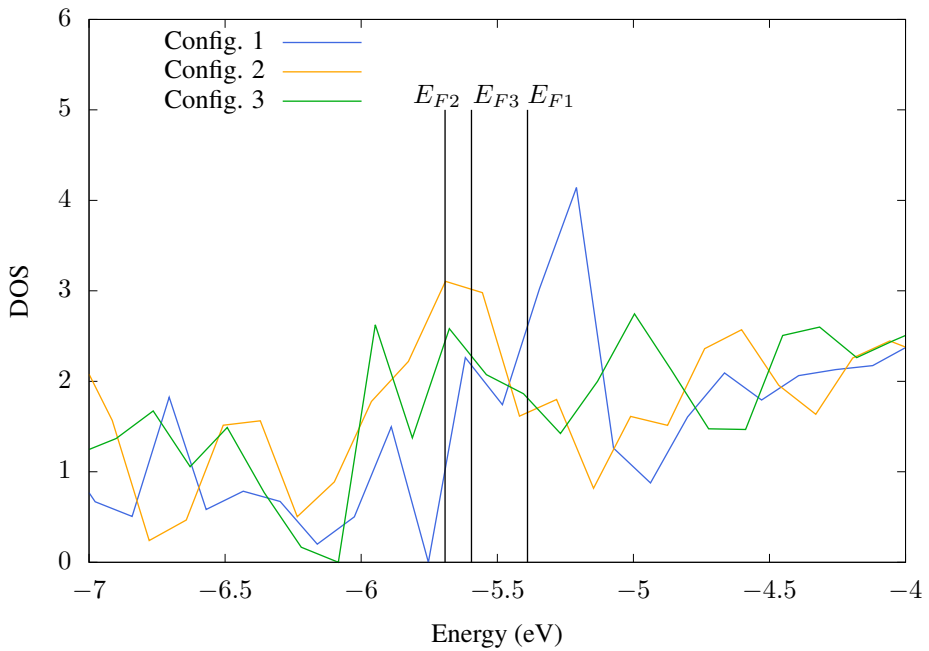
Figure 4.61: DOS as a function of energy for W-doped Si with a doping concentration of 3.22% with a vacancy in the lattice. Standard setup.

We now look at systems with a unit cell size of 64 atoms. In Figure 4.62, a Si-atom is replcaced by a W-atom. The deformation is quite apparent around the impurity, however, 2-3 lattice sites away, the lattice seems intact. The DOS of this configuration is shown in Figure 4.63. We see that there may be tendencies of a formation of an intermediate band around -6 eV to -5.5 eV. The DOS drops slightly on the edge of this region and the Fermi level lies within.

(a)

(b)

(c)

(d)

Figure 4.62: The unit cell of a 1.56% W-doped Si crystal. **(a)** and **(b)** are two perspectives of the initial configuration. **(c)** and **(d)** are two perspectives of the optimized geometry, labeled Config. 3.
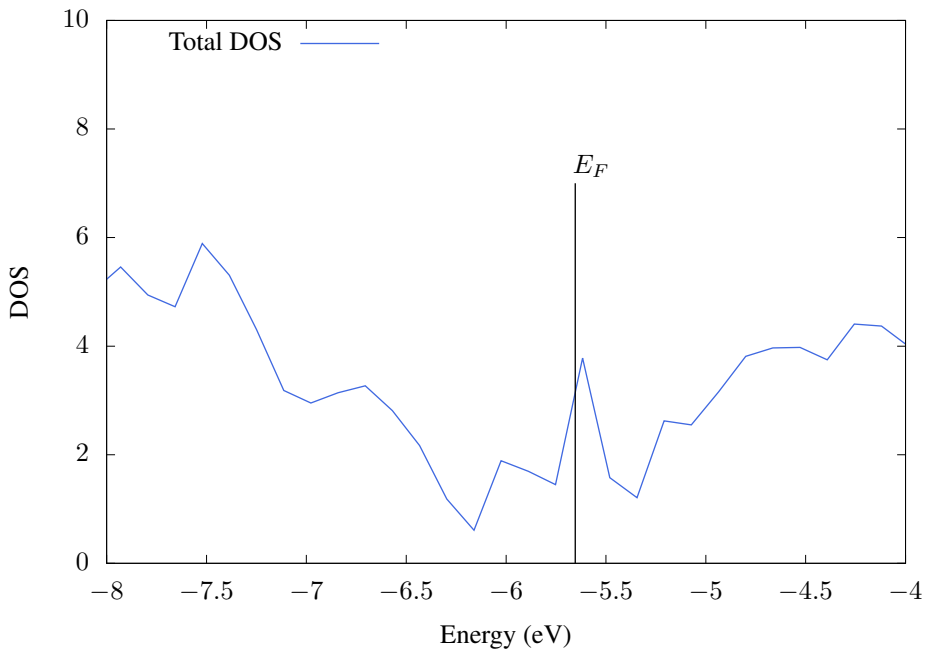
Figure 4.63: DOS as a function of energy for W-doped Si with a doping concentration of 1.56% with a vacancy in the lattice. Standard setup.

We now add two W-impurities instead of one. Three unit cell configurations are used, shown in Figure 4.64, Figure 4.65 and Figure 4.66. In the final configuration we see that the impurities have stayed separated after the geometry optimization, just like with the 32-atomic unit cell. There are no interesting properties when viewing the DOS in Figure 4.67 in the context of an IBSC.
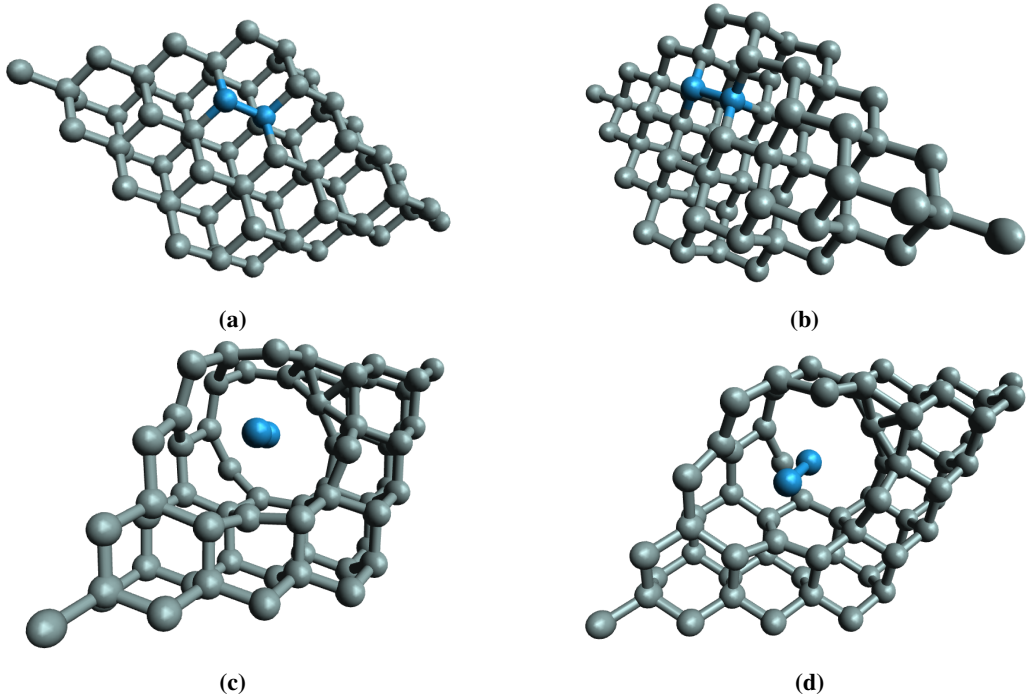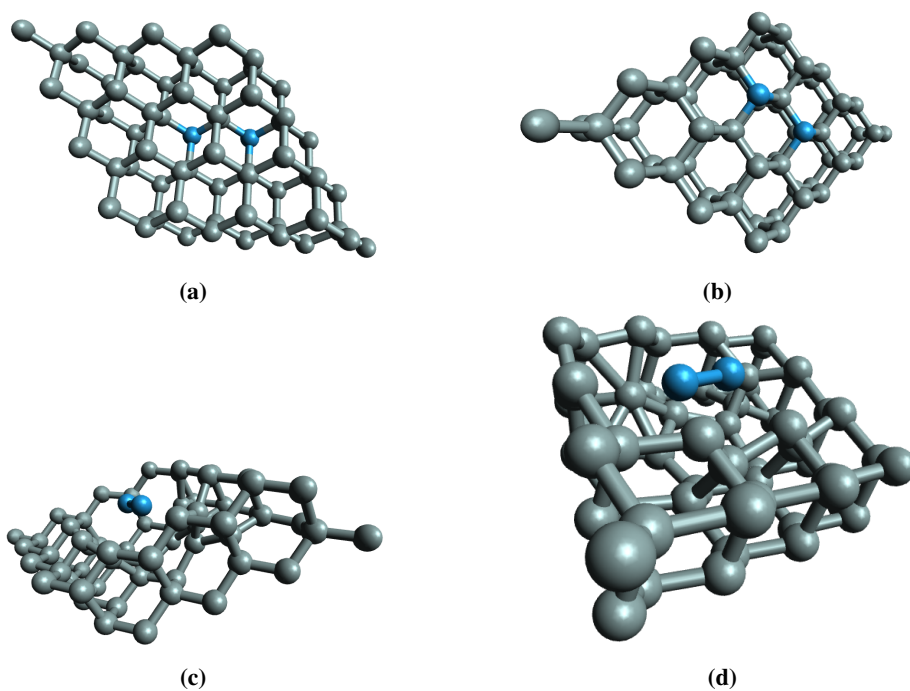

(a)

(b)

(c)

(d)

Figure 4.64: The unit cell of a 3.125% W-doped Si crystal. **(a)** and **(b)** are two perspectives of the initial configuration. **(c)** and **(d)** are two perspectives of the optimized geometry, labeled Config. 1.

(a)

(b)

(c)

(d)

Figure 4.65: The unit cell of a 3.125% W-doped Si crystal. **(a)** and **(b)** are two perspectives of the initial configuration. **(c)** and **(d)** are two perspectives of the optimized geometry, labeled Config. 2.

Figure 4.66: The unit cell of a 3.125% W-doped Si crystal. **(a)** and **(b)** are two perspectives of the initial configuration. **(c)** and **(d)** are two perspectives of the optimized geometry, labeled Config. 3.

Figure 4.67: DOS as a function of energy for W-doped Si with a doping concentration of 3.125%. Standard setup.

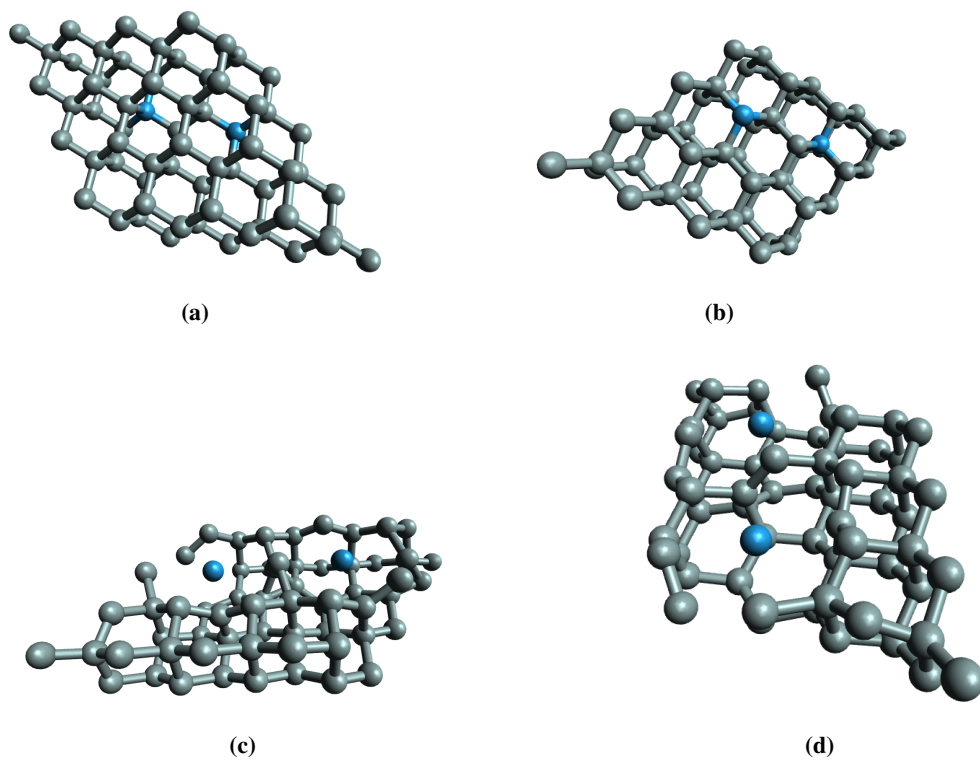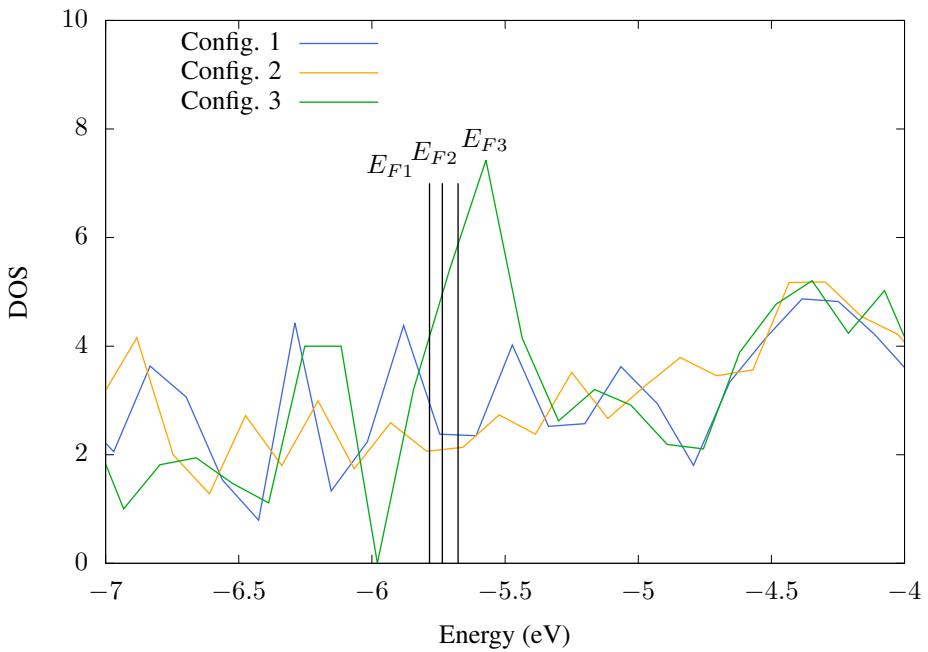We now add one W-impurity and remove one Si-atom in the lattice. Two unit cell configurations are used, shown in Figure 4.68 and Figure 4.69 with increasing distance between the impurity and the vacancy. There are no interesting properties in the DOS in Figure 4.70 in the context of an IBSC.

(a)

(b)

(c)

(d)

Figure 4.68: The unit cell of a 1.56% W-doped Si crystal. **(a)** and **(b)** are two perspectives of the initial configuration. **(c)** and **(d)** are two perspectives of the optimized geometry, labeled Config. 1.
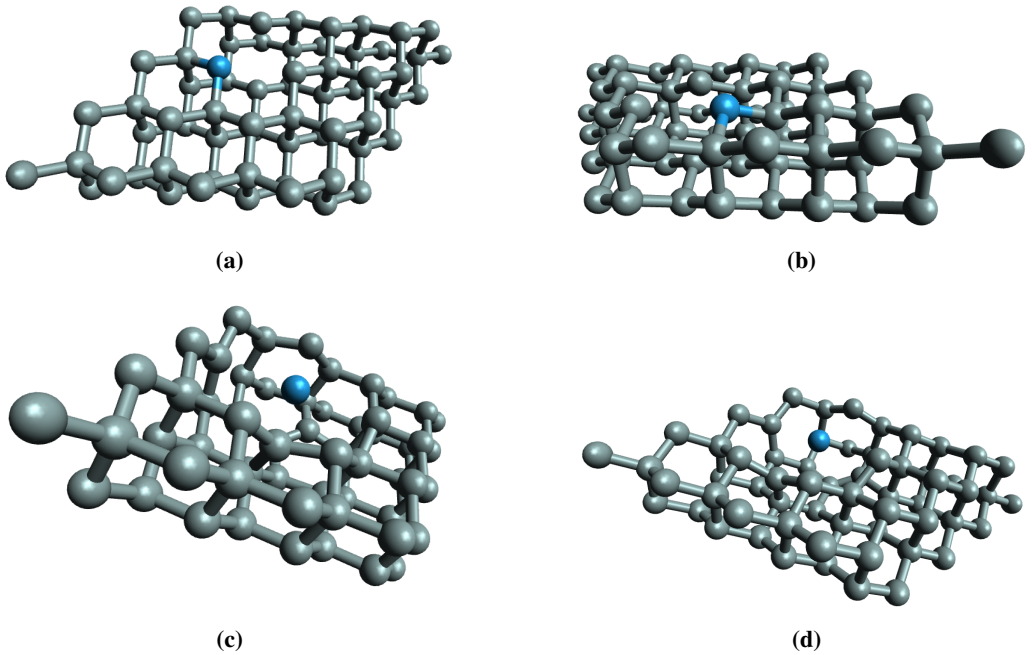
Figure 4.69: The unit cell of a 1.56% W-doped Si crystal with a vacancy in the lattice. **(a)** and **(b)** are two perspectives of the initial configuration. **(c)** and **(d)** are two perspectives of the optimized geometry, labeled Config. 2.
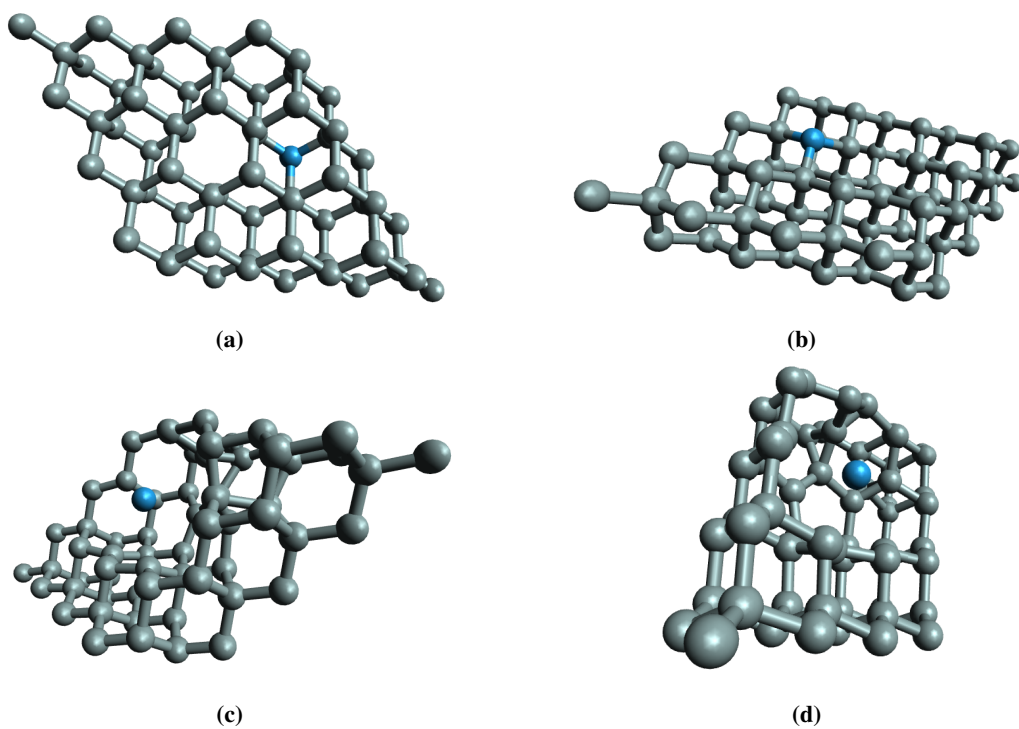
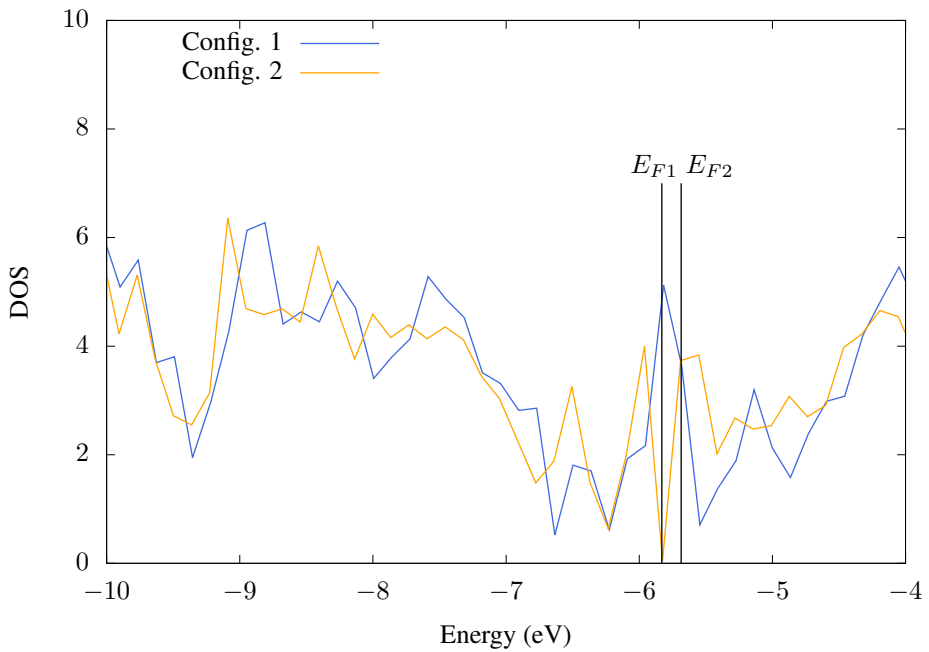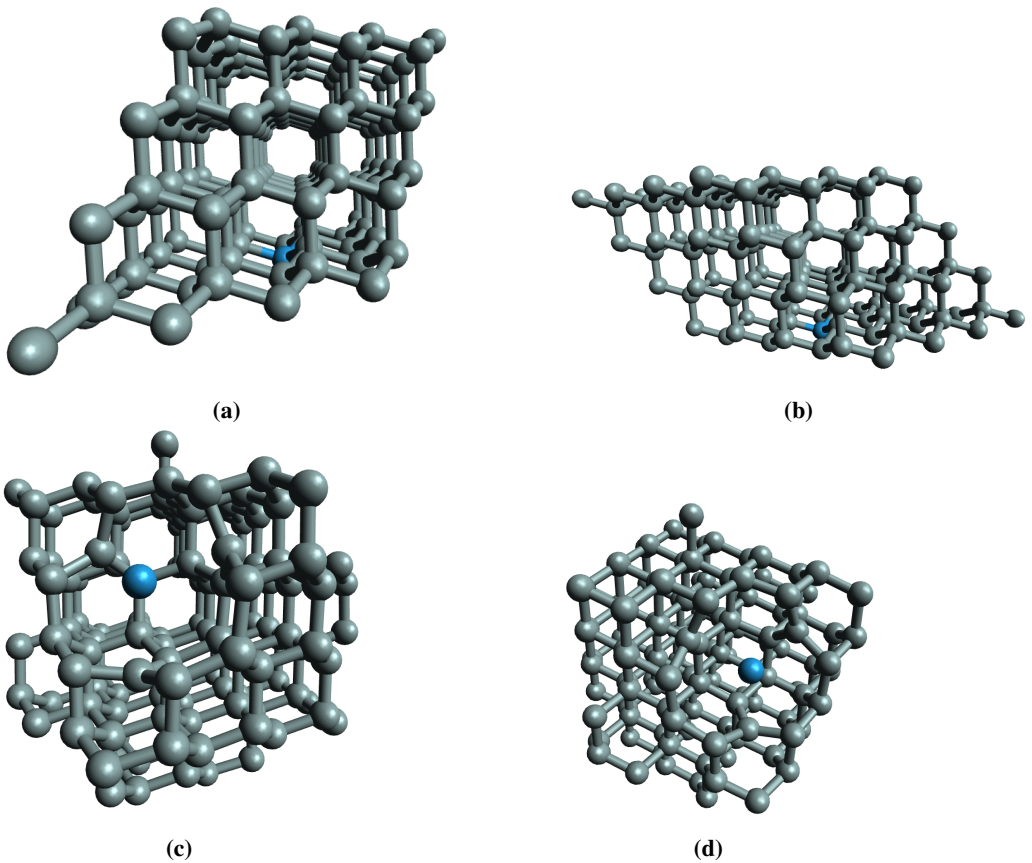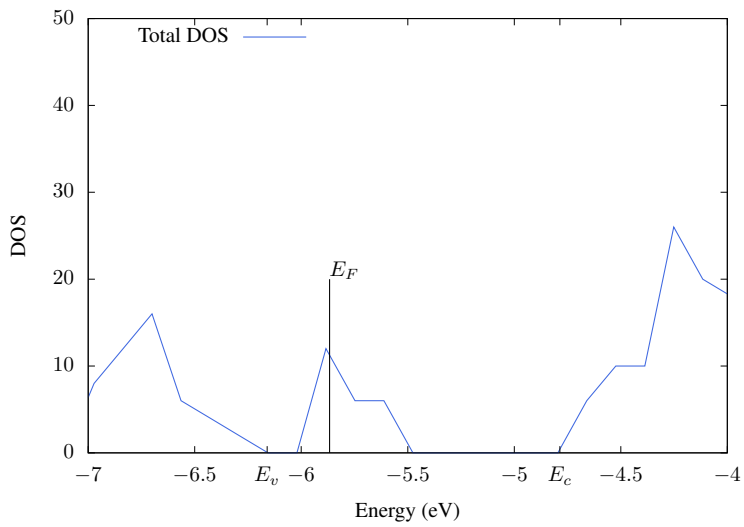**Figure 4.70:** DOS as a function of energy for W-doped Si with a doping concentration of 1.56% and a vacancy in the lattice. Standard setup.

MOPAC geometry optimizations were run on a crystal with a doping concentration of
0.78 %. In a 128-atomic Si diamond lattice unit cell, one Si atom was replaced by W. The
initial and final configurations are shown in Figure 4.71. It is clear that the W-atom has
made a cavity around it, taking more space. Further away from the W-atom, 2-3 lattice
sites away, the lattice seems untouched and intact, so the deformation of the lattice is
strictly in the immediate surrounding of the W-atom. The DOS is shown in Figure 4.72
and we see that an intermediate band has formed, and that the Fermi level lies inside this
band. The bottom of the conduction band lies at $E_C = -4.78$ eV, the top of the valence
band lies at $E_V = -6.16$ eV, giving a band gap of $E_g = 1.38$ eV, which is in the same
order of magnitude as pure Si. The bottom of the IB lies 0.15 eV above the top of the VB,
and the top of the IB lies 0.68 eV below the bottom of the conduction band, making the IB
fill about one third of the energies in the band gap.

(a)   (b)
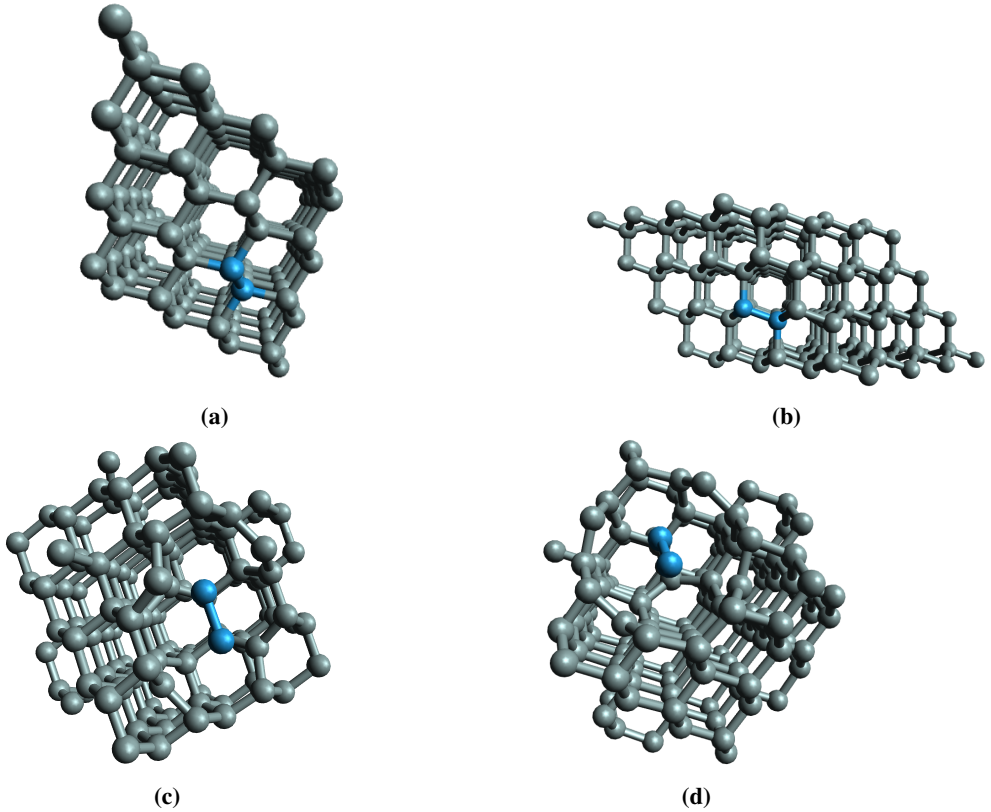
(c)   (d)

Figure 4.71: The unit cell of a 0.78% W-doped Si crystal. **(a)** and **(b)** are two perspectives of the
initial configuration. **(c)** and **(d)** are two perspectives of the optimized geometry.

Figure 4.72: DOS as a function of energy for W-doped Si with a doping concentration of 0.78%. Standard setup.

In Figure 4.75 we see the DOS from the two configuratons shown in Figure 4.73 and Figure 4.74. Two Si-atoms are replaced by W-atoms, with increasing distance in between them in the two configurations. The lattice deforms around the W-atoms, but leaves the lattice intact further away. There may be indications of an IB also here, but on the left side of what seems to be an IB for both the configurations, there is only a point which equals zero, not a continuous region.

(a)

(b)

(c)

(d)

Figure 4.73: The unit cell of a 1.56% W-doped Si crystal. **(a)** and **(b)** are two perspectives of the initial configuration. **(c)** and **(d)** are two perspectives of the optimized geometry, labeled Config. 1.

Figure 4.74: The unit cell of a 1.56% W-doped Si crystal. **(a)** and **(b)** are two perspectives of the initial configuration. **(c)** and **(d)** are two perspectives of the optimized geometry, labeled Config. 2.
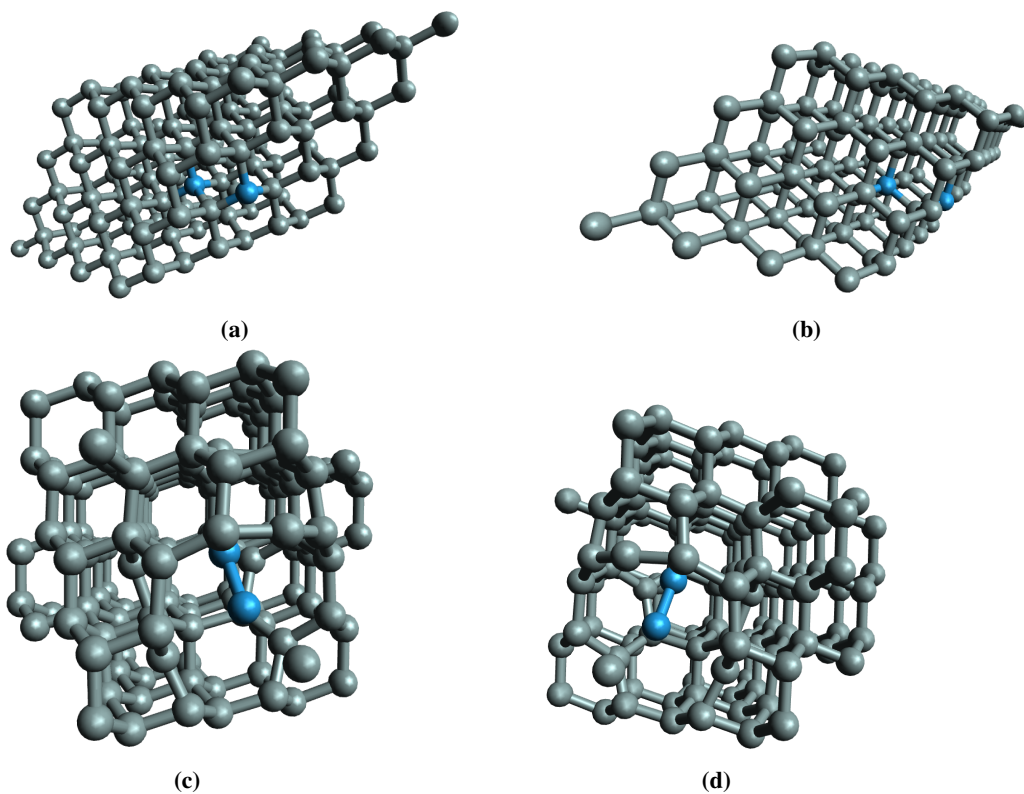
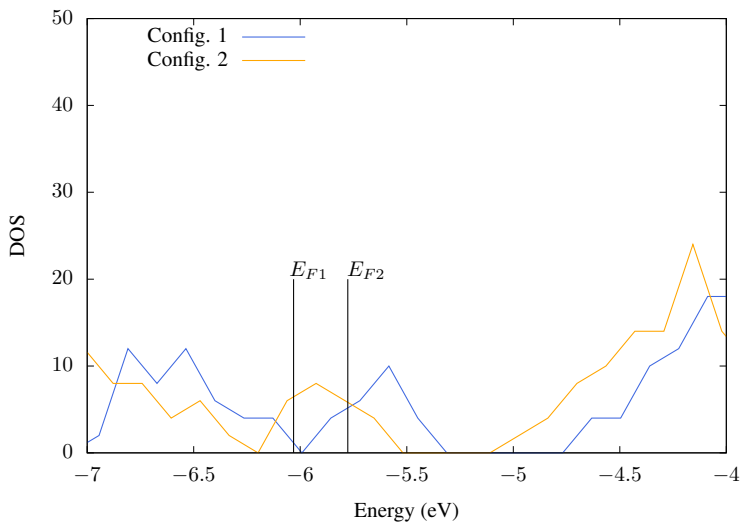**Figure 4.75:** DOS as a function of energy for W-doped Si with a doping concentration of 1.56%. Standard setup.

In Figure 4.79 we see the DOS of the three configurations shown in Figure 4.76, Figure 4.77 and Figure 4.78. A 128-atomic Si basis was used, then one W-atom replaced a Si-atom, and a Si atom was removed, leaving a vacancy in the unit cell. The DOS show clear tendencies for an IB around -6 eV in all three configurations. All three configurations have a region above the Fermi level where the DOS equals zero, between -5 eV and about -5.5 eV. Between the mark at -6 eV and -6.5 eV all the three configurations' DOS drop down, and configurations 1 and 2 touch zero, even though it is not for a continuous region.

(a)

(b)

(c)

(d)

Figure 4.76: The unit cell of a 0.79% W-doped Si crystal with a vacancy in the lattice. **(a)** and **(b)** are two perspectives of the initial configuration. **(c)** and **(d)** are two perspectives of the optimized geometry, labeled Config. 1.

Figure 4.77: The unit cell of a 0.79% W-doped Si crystal with a vacancy in the lattice. **(a)** and **(b)** are two perspectives of the initial configuration. **(c)** and **(d)** are two perspectives of the optimized geometry, labeled Config. 2.
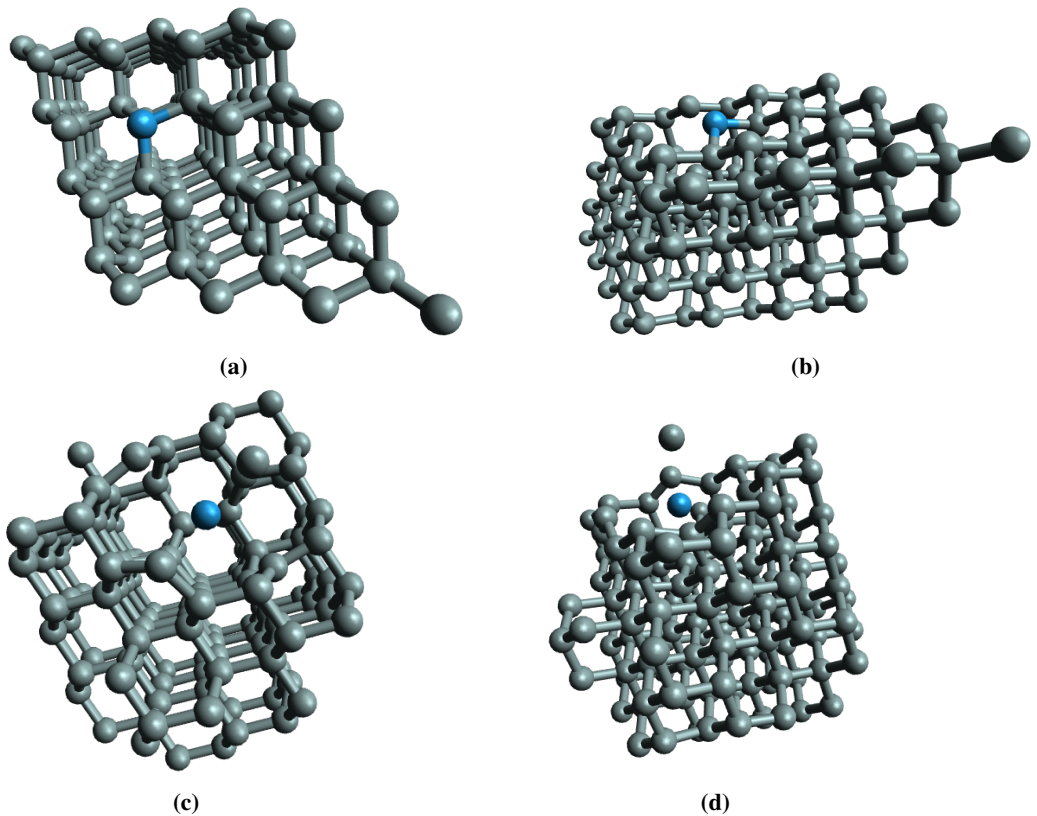
Figure 4.78: The unit cell of a 0.79% W-doped Si crystal with a vacancy in the lattice. **(a)** and **(b)** are two perspectives of the initial configuration. **(c)** and **(d)** are two perspectives of the optimized geometry, labeled Config. 3.
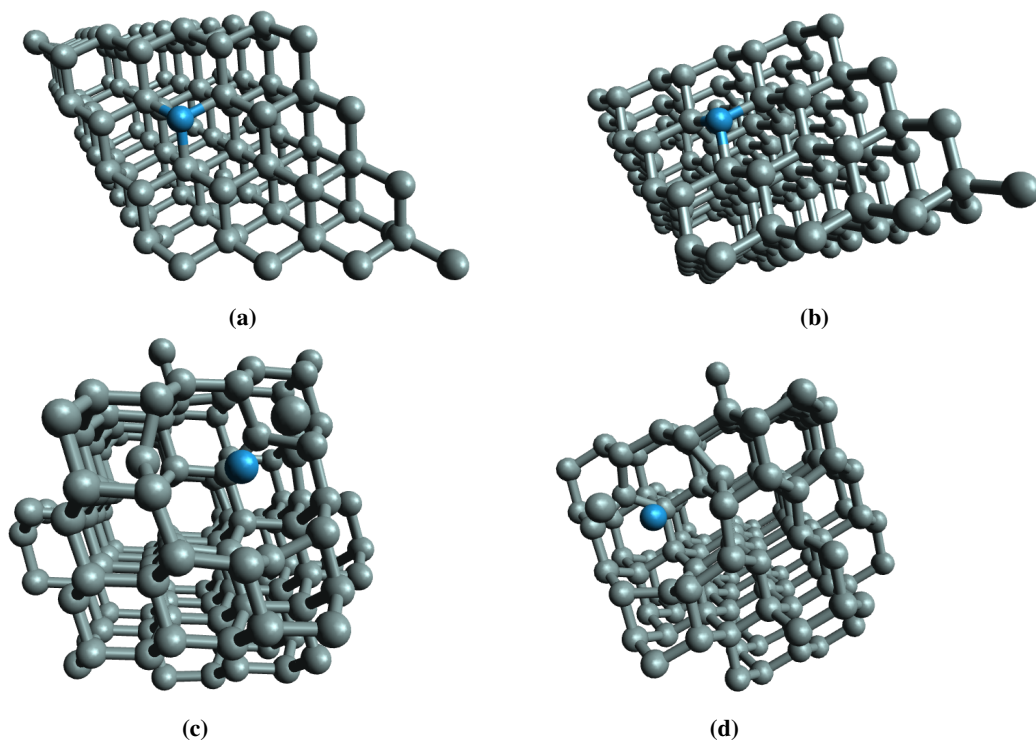
Figure 4.79: DOS as a function of energy for W-doped Si with a doping concentration of 0.79% with a vacancy in the lattice. Standard setup.
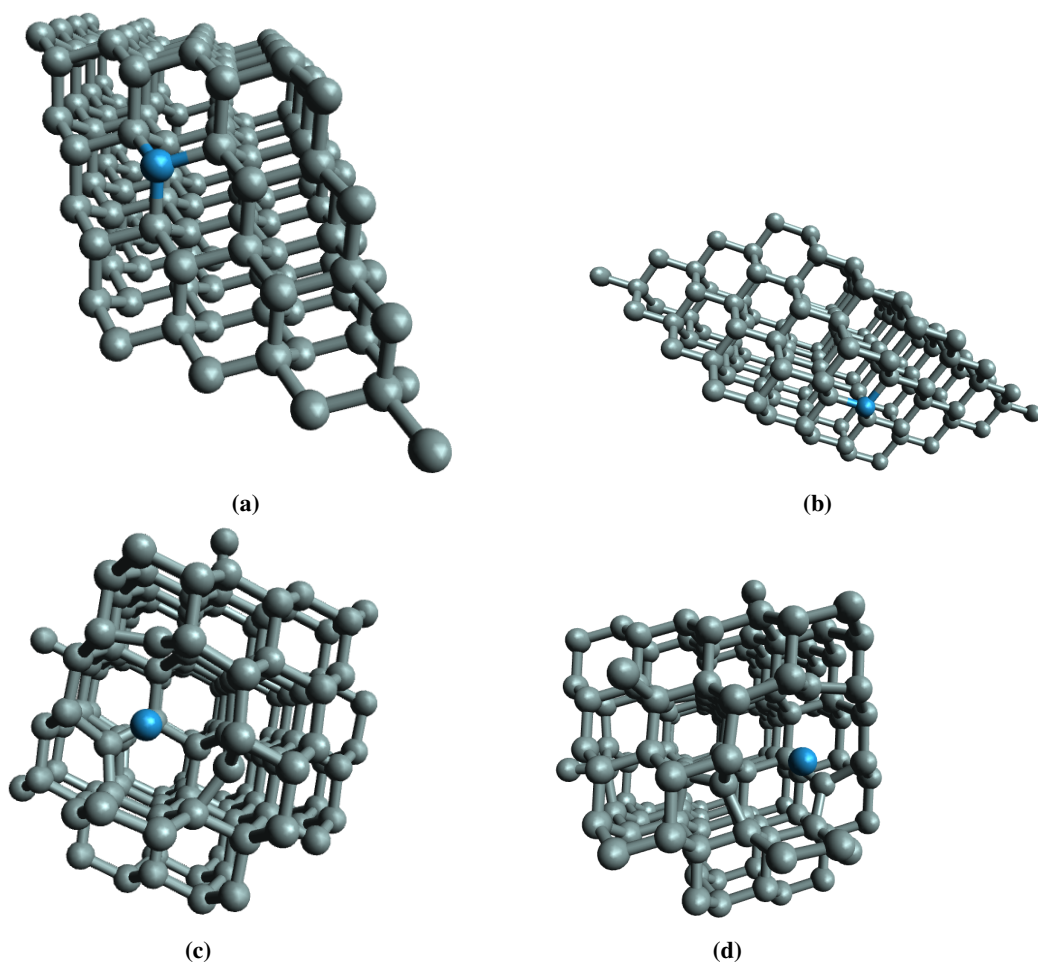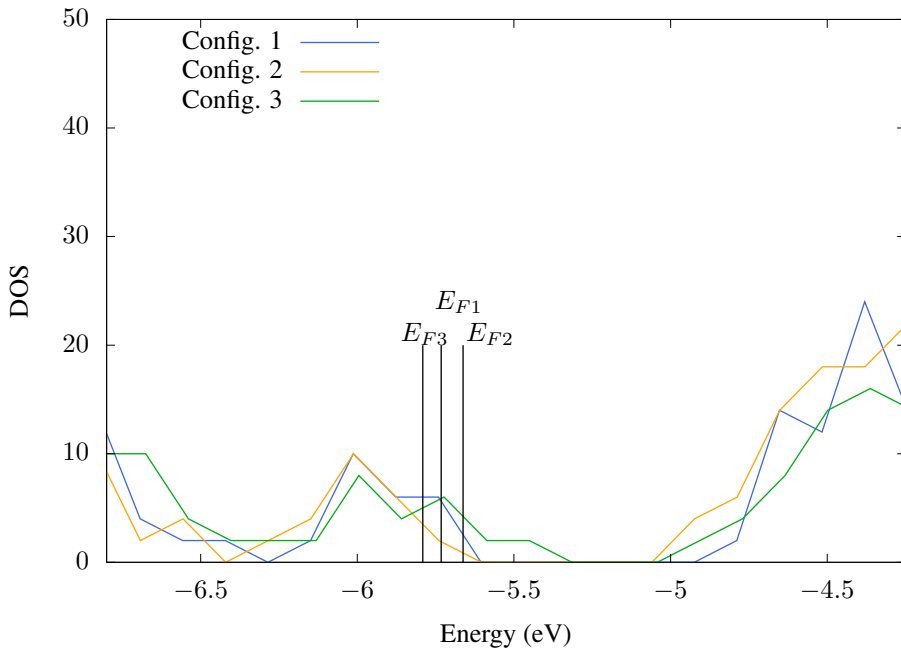
Chapter 5

Conclusion

We have conducted theoretical studies using DFT, DFTB and MOPAC to find the electronic properties of Si crystals, in particular under what conditions an intermediate band (IB) will form. Initially, DFT proved to underestimate the band gap when comparing to experimental results. Adding a Hubbard parameter in the Hamiltonian improved the results and made better correspondence with experiments. Upon a closer inspection of the band structure, important physical symmetry properties were broken when including the semi-empirical Hubbard correction. The Hubbard term was therefore omitted when doing calculations on the many systems in this thesis. The MOPAC geometry optimizations, being semi-empirical, gave vastly more disturbances in the lattice than DFTB and should not bear much weight. For the smallest systems, 2-atomic to 16-atomic basis, DFT geometry optimizations were run on Si doped with Ag and W showing no signs of an IB. For the largest systems containing Ag, 32-atomic to 128-atomic basis, DFTB was used to optimize the geometry and DFT calculations were run on the optimized geometry. Tendencies of an IB were found at a doping concentration of 0.78 %, two different configurations with doping concentration 1.56 %, and two different configurations with doping concentration 0.79 % with vacancies in the lattice. For the largest systems containing W, 32-atomic to 128-atomic basis, MOPAC was used to optimize the geometry and DFT calculations were run on the optimized geometry. Si doped with W with a doping concentration of 0.78 % exhibits an IB at the Fermi level, with a band gap of 1.38 eV and the IB placed 0.15 eV above the VB and 0.68 eV below the CB. A W doping concentration of 1.56 % also showed tendencies of an IB, but the numerical quality for the large systems proved it difficult to conclude anything with certainty. It should be noted that all the results do not have a satisfying accuracy to conclude that an IB will form for certain. Among the many systems investigated in this thesis, more detailed calculations should be run on the systems that showed tendencies of an IB.

Chapter 6

Future Work

This chapter gives suggestions on further work to be done based on the results presented in this thesis.

• A more thorough study on the distance between two or more impurities before and after a geometry optimization should be done. Some of our results showed the existence of some critical distance which determines whether the two impurities will stay separated or move together to form a cluster. This was the case for both the MOPAC and DFTB calculations. A way to investigate this problem would be to track the movement of an impurity, keeping a fixed distance between the other impurity while optimizing the surrounding lattice. Then stepwise increasing the distance between the impurities and tracking the total energy, to find some energy barrier at some point. This energy barrier will determine if the two impurities will move together or stay separated. The interatomic distance between the two impurities when the energy has a maximum will be the critical distance.

• In this thesis, we have studied a manifold of systems, some of which showed the tendencies of an IB. These particular systems should be investigated in more detail with both higher accuracy DFT calculations and cross-examined by other methods, both theoretical and experimental.

• DFTB more closely resembles DFT, and is a more accurate theory than MOPAC. Developing Si-W parameters for DFTB, so that DFTB may be used for W-doped Si would be of value to the worldwide scientific community doing both theoretical and experimental studies on these kinds of materials.

Bibliography

[1] Yoshihiro Hamakawa. Background and motivation for thin-film solar-cell development. In *Thin-Film Solar Cells*, pages 1–14. Springer, 2004.

[2] Antonio Luque and Antonio Martí. Increasing the efficiency of ideal solar cells by photon induced transitions at intermediate levels. *Physical Review Letters*, 78(26): 5014, 1997.

[3] David Sholl and Janice A Steckel. *Density functional theory: a practical introduction*. John Wiley & Sons, 2011.

[4] Peter Politzer and Jorge M Seminario. *Modern density functional theory: a tool for chemistry*, volume 2. Elsevier, 1995.

[5] Richard M Martin. *Electronic structure: basic theory and practical methods*. Cambridge university press, 2004.

[6] VP Gupta. *Principles and Applications of Quantum Chemistry*. Academic Press, 2015.

[7] Pierre Hohenberg and Walter Kohn. Inhomogeneous electron gas. *Physical Review*, 136(3B):B864, 1964.

[8] Per C Hemmer. Faste stoffers fysikk. *Tapir Forlag*, 1987.

[9] Walter Kohn and Lu Jeu Sham. Self-consistent equations including exchange and correlation effects. *Physical Review*, 140(4A):A1133, 1965.

[10] Axel D Becke. A new inhomogeneity parameter in density-functional theory. *The Journal of chemical physics*, 109(6):2092–2098, 1998.

[11] John F Dobson, Giovanni Vignale, and Mukunda P Das. *Electronic density functional theory: recent progress and new directions*. Springer Science & Business Media, 2013.

[12] O Gunnarsson, M Jonson, and BI Lundqvist. Descriptions of exchange and correlation effects in inhomogeneous electron systems. *Physical Review B*, 20(8):3136, 1979.

[13] Xin Xu and William A Goddard. The x3lyp extended density functional for accurate descriptions of nonbond interactions, spin states, and thermochemical properties. *Proceedings of the National Academy of Sciences of the United States of America*, 101(9):2673–2677, 2004.

[14] Jianmin Tao, John P Perdew, Viktor N Staroverov, and Gustavo E Scuseria. Climbing the density functional ladder: Nonempirical meta–generalized gradient approximation designed for molecules and solids. *Physical Review Letters*, 91(14):146401, 2003.

[15] Yan Zhao and Donald G Truhlar. Calculation of semiconductor band gaps with the m06-l density functional. *The Journal of chemical physics*, 130(7):074103, 2009.

[16] Walter Kohn. Analytic properties of bloch waves and wannier functions. *Physical Review*, 115(4):809, 1959.

[17] Ben G Streetman and Sanjay Kumar Banerjee. *Solid State Electronic Devices: Global Edition*. Pearson education, 2016.

[18] William Shockley and Hans J Queisser. Detailed balance limit of efficiency of p-n junction solar cells. *Journal of applied physics*, 32(3):510–519, 1961.

[19] Jenny Nelson. *The physics of solar cells*. World Scientific Publishing Company, 2003.

[20] SCM webpage. `https://www.scm.com`. Accessed: 2018-03-03.

[21] G Te Velde and EJ Baerends. Precise density-functional method for periodic structures. *Physical Review B*, 44(15):7888, 1991.

[22] ADF BAND Documentation, basis set. `https://www.scm.com/doc/BAND/Input/Basis.html`. Accessed: 2018-02-25.

[23] Attila Szabo and Neil S Ostlund. *Modern quantum chemistry: introduction to advanced electronic structure theory*. Courier Corporation, 2012.

[24] BH Bransden and CJ Joachain. Quantum mechanics 2nd edition, 2000.

[25] Mike C Payne, Michael P Teter, Douglas C Allan, TA Arias, and JD Joannopoulos. Iterative minimization techniques for ab initio total-energy calculations: molecular dynamics and conjugate gradients. *Reviews of modern physics*, 64(4):1045, 1992.

[26] John C Slater. A simplification of the hartree-fock method. *Physical Review*, 81(3):385, 1951.

[27] Seymour H Vosko, Leslie Wilk, and Marwan Nusair. Accurate spin-dependent electron liquid correlation energies for local spin density calculations: a critical analysis. *Canadian Journal of physics*, 58(8):1200–1211, 1980.

[28] John P Perdew, P Ziesche, and H Eschrig. *Electronic structure of solids 91*, volume 11. Akademie Verlag, Berlin, 1991.

[29] John P Perdew, Kieron Burke, and Matthias Ernzerhof. Generalized gradient approximation made simple. *Physical Review Letters*, 77(18):3865, 1996.

[30] John P Perdew, Adrienn Ruzsinszky, Gábor I Csonka, Oleg A Vydrov, Gustavo E Scuseria, Lucian A Constantin, Xiaolan Zhou, and Kieron Burke. Restoring the density-gradient expansion for exchange in solids and surfaces. *Physical Review Letters*, 100(13):136406, 2008.

[31] Yan Zhao and Donald G Truhlar. A new local density functional for main-group thermochemistry, transition metal bonding, thermochemical kinetics, and noncovalent interactions. *The Journal of chemical physics*, 125(19):194101, 2006.

[32] Yan Zhao and Donald G Truhlar. The m06 suite of density functionals for main group thermochemistry, thermochemical kinetics, noncovalent interactions, excited states, and transition elements: two new functionals and systematic testing of four m06-class functionals and 12 other functionals. *Theoretical Chemistry Accounts: Theory, Computation, and Modeling (Theoretica Chimica Acta)*, 120(1):215–241, 2008.

[33] Viktor N Staroverov, Gustavo E Scuseria, Jianmin Tao, and John P Perdew. Comparative assessment of a new nonempirical density functional: Molecules and hydrogen-bonded complexes. *The Journal of chemical physics*, 119(23):12129–12137, 2003.

[34] ADF DFTB Documentation, frozen core approximation. `https://www.scm.com/doc/ADF/Input/Electronic_Configuration.html#frozen-core-approximation`. Accessed: 2018-03-06.

[35] U Von Barth and CD Gelatt. Validity of the frozen-core approximation and pseudopotential theory for cohesive energy calculations. *Physical Review B*, 21(6):2222, 1980.

[36] Matteo Cococcioni and Stefano De Gironcoli. Linear response approach to the calculation of the effective interaction parameters in the lda+ u method. *Physical Review B*, 71(3):035105, 2005.

[37] ADF BAND Documentation, gga+u. `https://www.scm.com/doc/BAND/Input/Density_functional.html#gga-u`, . Accessed: 2018-02-26.

[38] Robert S Mulliken. Electronic population analysis on lcao–mo molecular wave functions. i. *The Journal of Chemical Physics*, 23(10):1833–1840, 1955.

[39] Andrew R Leach. *Molecular modelling: principles and applications*. Pearson education, 2001.

[40] Pekka Koskinen and Ville Mäkinen. Density-functional tight-binding for beginners. *Computational Materials Science*, 47(1):237–253, 2009.

[41] ADF DFTB Documentation, dftb. `https://www.scm.com/product/dftb/`, . Accessed: 2018-03-06.

[42] DFTB.org parameter library. `https://www.dftb.org/`. Accessed: 2018-03-06.

[43] Carlos Fiolhais, Fernando Nogueira, and Miguel AL Marques. *A primer in density functional theory*, volume 620. Springer Science & Business Media, 2003.

[44] ADF BAND Documentation, units in the density of states (dos) plot. `https://www.scm.com/faq/band-faq/#what-are-the-units-in-the-density-of-states-dos-plot`, . Accessed: 2018-05-10.

[45] Vladimir I Anisimov, Jan Zaanen, and Ole K Andersen. Band theory and mott insulators: Hubbard u instead of stoner i. *Physical Review B*, 44(3):943, 1991.

[46] Manuel Cardona and Fred H Pollak. Energy-band structure of germanium and silicon: The k· p method. *Physical Review*, 142(2):530, 1966.

[47] EO Kane. Band structure of silicon from an adjusted heine-abarenkov calculation. *Physical Review*, 146(2):558, 1966.

[48] T Kunikiyo, M Takenaka, Y Kamakura, M Yamaji, H Mizuno, M Morifuji, K Taniguchi, and C Hamaguchi. A monte carlo simulation of anisotropic electron transport in silicon including full band structure and anisotropic impact-ionization model. *Journal of Applied Physics*, 75(1):297–312, 1994.

[49] RC Albers, Niels Egede Christensen, and Axel Svane. Hubbard-u band-structure methods. *Journal of Physics: Condensed Matter*, 21(34):343201, 2009.

[50] W Klement. Lattice parameters of the metastable close-packed structures in silver-germanium alloys. *J. Inst. Metals.1961.90*, (9):27–30, 1961.

[51] G Müller and S Kalbitzer. The crystalline-to-amorphous transition in ion-bombarded silicon. *Philosophical Magazine B*, 41(3):307–325, 1980.

[52] ADF BAND Documentation, lattice vectors. `https://www.scm.com/doc/BAND/Input/Geometry.html#lattice-vectors`, . Accessed: 2018-05-10.